Doctoral Dissertation (Shinshu University)

Study on the Multi-Functional Electrospun Nanofibers and Their Applications

September, 2015

Interdisciplinary Graduate School of Science and Technology, Shinshu University

Department of Bioscience and Textile Technology

Bang Hyunsik

ABSTARCT

Study on the Multi-Functional Electrospun Nanofibers and Their Applications

The design and development of electrospun polymer fibers with sub-micrometer diameters from various kinds of materials has gained significant attention due to several amazing characteristics such as very large surface area to volume ratio, flexibility in surface functionalities, and superior mechanical performances, which make the polymer nanofibers to be optimal candidates for many important applications, such as electronics, medicine, sensor, and controlled release technology, etc. However, despite of the potential mentioned above, the application of nanofibers has been limited due to its poor mechanical properties. In a recent year, to maximize the good properties and complement the weaknesses, the combined technologies for producing the functional composite nanofibers incorporating various nano-objects (such as carbon nanotubes, ceramics metal nanoparticles, etc) in a broad range of areas such as electronics, medicine, sensor, and controlled release technology are being conceived these days.

Carbon nanotubes (CNTs) have attracted great attention as ideal fillers for reinforcement because of their unique physical and mechanical properties since the discovery by Ijima. To date, the reinforcement of both single wall carbon nanotubes (SWNTs) and multiwalled carbon nanotubes (MWNTs) on polymer composites has received great attention. Up to date, PVA/CNT composite materials have been widely studied since the hydroxyl groups of the PVA and the carboxyl groups of the modified

CNTs can form strong interaction via hydrogen bonding. Although a lot of works have been done to learn the interfacial interactions between the carbon nanotubes and the polymer chains and the load-transfer efficiency from the polymer to the carbon nanotubes, few people studied how pH value of the polymer/acid-treated MWNT solution affects the connections between the MWNT and polymer matrix. We report the influence the pH of the aqueous PVA/MWNT dispersion solution on the morphology and mechanical properties of the corresponding electrospun PVA/acid-treated MWNT composite nanofibers.

The ferric hexacyanoferrate ($Fe_4III[FeII(CN)_6]_3$) is well known as Prussian blue (PB), often used as an efficient adsorbent for the removal of radioactive cesium (Cs) from the wastewater. Developing an efficient, stable and easily handlable PB nanoparticles-based material for the removal of Cs remains an highly demanding issue. Metal nanoparticles-based PVA composite nanofibers have been extensively used for several applications. In fact, PVA is largely available, highly hydrophilic, easily processable, biocompatible, non–toxic and chemical resistive. We report a new Prussian blue nanoparticle (PBNPs) incorporated polyvinyl alcohol (PVA) composite nanofiber (*c*-PBNPs/PVA) for a rapid adsorption of Cs from the radioactive wastewater. Inductive coupled plasma-mass spectroscopy (ICP-MS) was used to measure the Cs adsorption activity of the *c*-PBNPs/PVA in wastewater. Therefore, the simple preparation, easy separation and faster Cs adsorption activity expect *c*-PBNPs/PVA as an alternate choice to the existing PBNPs-composite materials.

Metal nanoparticles (MNPs) have played a tremendous role as heterogeneous catalysts in various organic reactions. Particularly, supported MNPs catalysts are

preferred over the unsupported MNPs due to their simple separation and. Till date, several supported MNPs catalysts are reported for various organic reactions. Electrospun nanofibers (NFs) including cellulose nanofibers (CNFs) have attracted much attention due to their unique properties such as large surface area to volume ratio, biocompatibility, simple surface functionalization, easy handling and outstanding mechanical properties. The CNFs and their composites have been used for various potential applications such as sensors, energy, catalysis, biomedical, separators and filters. We have prepared noble MNPs supported on CNFs (RuNPs/CNFs and AgNPs/CNFs) by a simple reduction method. After complete characterization, the RuNPs/CNFs and AgNPs/CNFs were used as nanocatalysts for the oxidation of benzyl alcohol and *aza*-Michael reaction, respectively.

ACKNOWLEDGEMENTS

TABLE OF CONTENTS

LIST OF TABLES

LIST OF FIGURES

x

LIST OF SCHEMES

CHAPTER 1

Introduction

CHAPTER 1

Introduction

1.1 Background

Nanotechnology is considered one of the most promising technologies for the 21st century. Optimizing products, decreasing the ecological impact and consumption of natural resources has the potential to improve the effectiveness of a number of existing consumer and industrial products and is expected to have a substantial impact on the development of new high tech applications. Nanotechnology is an expected future manufacturing technology that will make most products lighter, stronger, cleaner, less expensive and more precise. Nanotechnology is either when nanoscaled materials are produced (defined by their thickness, particle size or other structural features) or when the nature of a process involves the use of nanoscaled materials. Research and development in nanotechnology is directed toward understanding and creating improved materials, devices, and systems that exploit these new properties.

1.2 Electrospinning

Electrospinning which the most popular and attractive method in fiber production has become due to form very fine fibers ranging from 10 nm to 10 μm in diameter with various types of fiber morphology, significantly smaller than a human hair. Polymer nanofibers are in demand due to their potential advanced applications. Electrospinning is

an emerging method for producing nanofibers. Electrospun fibers with their high surface area to volume ratio and small pores, are drawing interest in vast variety of applications, some being, filtration products, scaffolds for tissue engineering, wound dressings, drug release materials, fiber reinforcement composites, protective clothing [1-3].

1.2.1 History

Although the research related to electrospinning technique was not blooming until middle 1990s, the recognition of this process has been almost 100 years. This probably led to the invention of electrospinning to produce fibers in the early 1900s by Cooley and Morton. In one of the earliest electrospinning inventions, Cooley patented a set-up that used auxiliary electrodes to direct the electrospinning jet onto a rotating collector. In the 1930s, Formhals has introduced several innovative set-ups to produce yarns from electrospun fibers, including designs that did not require the use of a spinneret[4] and patented his invention relating to the process and the apparatus. In 1940, Formhals patented another method for producing composite fiber webs from multiple polymer substrates by electrostatically spinning polymer fibers on a moving base substrate. In 1969, Taylor studied the shape of the polymer droplet produced at the tip of the needle when an electric field was applied and showed that it was a cone and the jets ejected from the vortices of the cone. This cone was later referred to as the 'Taylor cone'. The effects of electric field, experimental conditions and the factors affecting the atomization and fiber stability were studied [5-7]. For the fiber industries, one important consideration is the rate of fiber production. Electrospinning, compared to the popular industrial fiber spinning processes, has very low production rates [4,6,7].

1.2.2 Fundamentals

The basic electrospinning setup is composed of at least a high-voltage power supply (typically 1~30kV), a reservoir for polymer solution or melts which can provide stable flow rate (typically 1~ 50 μl/min) through a conductive spinneret, and a grounded collector for the deposit of fiber mats. Usually a syringe pump can be used to generate a steady flow rate of the polymer solution or melts continuously. If ignoring other environmental effects, without the electric field, the slowly flowing liquid droplets will form and drop at the tip of the spinneret by the balance of only two forces: surface tension and gravity. When an electrostatic potential is applied between the spinneret and the collector, a point-to-plate type of electrostatic field will form, which will charge the surface of the droplets, thereby cause electrostatic repulsion force to form besides the surface tension and gravity. Since the effect of gravity is very small compared to the electrostatic force in electrospinning, it will be omitted in following discussions. With the increase of electric field, the combined effect from electric force and surface tension changed the shape of the droplet from a meniscus to a cone-shaped structure known as "Taylor cone" [6,7], until the gradient of electric field can finally break the droplet into a liquid jet.

The quality of nanofibers produced in any electrospinning experiment is affected by a variety of material and process variables. From a practical standpoint, two such sets of variables might be identified; equipment-related and material-related variables. Each set includes a number of different and sometimes interrelated variables. Material variables include the solution (or melt) temperature, solution concentration and viscosity, solvent volatility, solvent vapor pressure, dielectric properties of the system, solution

conductivity and surface tension, and the molecular weight, molecular weight distribution and structure (branched, linear) of the polymer. Process variables include solution flow rate, applied electric potential, tip-to-target distance, ambient parameters (temperature, humidity and air velocity in the environment surrounding the spinning fiber), type of target screen and internal diameter of the capillary. Changing any of these can not only change fiber morphology and mat structure of the nanofiber formed but in some instances even determine if electrospinning occurs at all. Comprehensive predictive models that encompass all pertinent variables have not been developed as yet. Only qualitative general guidelines are available on the effect of these variables on fiber or mat quality, making electrospinning as much an art as it is a science. Generally, it is well known that increasing solution concentration or flow rate will increase the resultant fiber diameter, and increasing the applied voltage or tip-to-target distance will decrease it. Solutions with really high viscosity or surface tension will generally have trouble electrospinning because the droplet will resist forming into a cone and projecting towards the collector. Consequently, polymers that tend to form high viscosity solutions like high molecular weight or highly branched polymers will have difficulty electrospinning. On the other hand, if the polymer molecular weight is too low, the charged jet will break up to form droplets, a phenomenon commonly referred to as electrospraying. The formation of such droplets was reported to be due to the capillary breakup of the jet by surface tension [8].

1.2.3 Parameters

Many parameters can influence the transformation of polymer solutions into nanofibers through electrospinning. These parameters include (a) the solution properties such as viscosity, elasticity, conductivity, and surface tension, (b) governing variables

such as hydrostatic pressure in the capillary tube, electric potential at the capillary tip, and the gap (distance between the tip and the collecting screen), and (c) ambient parameters such as solution temperature, humidity, and air velocity in the electrospinning chamber [9].

Several researchers investigated spinnibility of different polymers. For instance, [10] found for electrospinning of aqueous poly(ethylene oxide) (PEO) dissolved in ethanol-to-water solutions that viscosities in the range of 1–20 poises and surface tension between 35 and 55 dynes/cm were suitable for fiber formation. At viscosities above 20 poises, electrospinning was prohibited because of the instability of flow caused by the high cohesiveness of the solution. Droplets were formed when the viscosity was too low (<1 poise). Similarly, for electrospinning of cellulose acetate (CA) in 2:1 acetone/ DMAc (dimethylacetamide), [11] recognized that viscosities between 1.2 and 10.2 poises were applicable. Outside that range, the CA solutions could not be electrospun into fibers at room temperature. Namely, either only few fibers could be obtained from a even higher viscosity solution or the fluid jet broke up to droplets due to too low viscosity (<1.2 poise). These two examples clearly demonstrated that the viscosity range of a different polymer solution which is spinnable is different.

As long as a polymer can be electrospun into nanofibers, ideal targets would be in that: (1) the diameters of the fibers be consistent and controllable, (2) the fiber surface be defect-free or defect-controllable, and (3) continuous single nanofibers be collectable. However, researches so far have shown that there three targets are by no means easily achievable.

One of the most important quantities related with electrospinning is the fiber diameter. Since nanofibers are resulted from evaporation or solidification of polymer fluid jets, the fiber diameters will depend primarily on the jet sizes as well as on the polymer contents in the jets. It has been recognized that during the traveling of a solution jet from the pipette onto the metal collector, the primary jet may [12-14] or may not [47-51] be split into multiple jets, resulting in different fiber diameters. As long as no splitting is involved, one of the most significant parameters influencing the fiber diameter is the solution viscosity. A higher viscosity results in a larger fiber diameter [9,10,20]. However, when a solid polymer is dissolved in a solvent, the solution viscosity is proportional to the polymer concentration. Thus, the higher the polymer concentration the larger the resulting nanofiber diameters will be. In fact, Deitzel et al. pointed out that the fiber diameter increased with increasing polymer concentration according to a power law relationship [13]. Demir et al. further found that the fiber diameter was proportional to the cube of the polymer concentration [16]. Another parameter which affects the fiber diameter to a remarkable extent is the applied electrical voltage. In general, a higher applied voltage ejects more fluid in a jet, resulting in a larger fiber diameter [16].

1.3 Applications

Recently, nanofiber-related publications and patents have increased geometrically. Especially electrospun nanofibers, own a group of unique features and mechanical, thermo or electric properties owing to their nanocomposite structures, nano or submicron scale and controllable formations. Nanofibers with the diameter of 100nm can have a

surface area to mass ratio as high as 100 m^2/g [17]. With this kind of super high surface area and porosity to the extreme of as high as 90%, nanofibers can be applied to many biological or industrial engineering such as 3-D scaffolds for tissue engineering, protective textile, catalyst supports, nanoscale reinforcement and ultrafiltration membranes etc, wherein more than half of the current research interests exit in the biomedical or bioengineering related field. Several nice review of the nanofiber application could be referred to such as the review from Zhang et al. [18] and Sawicka et al. [19]. Major application area related to polymers will be introduced in the following sections. Applications of inorganic ceramic nanofibers and carbon nanofibers can be found enormously elsewhere.
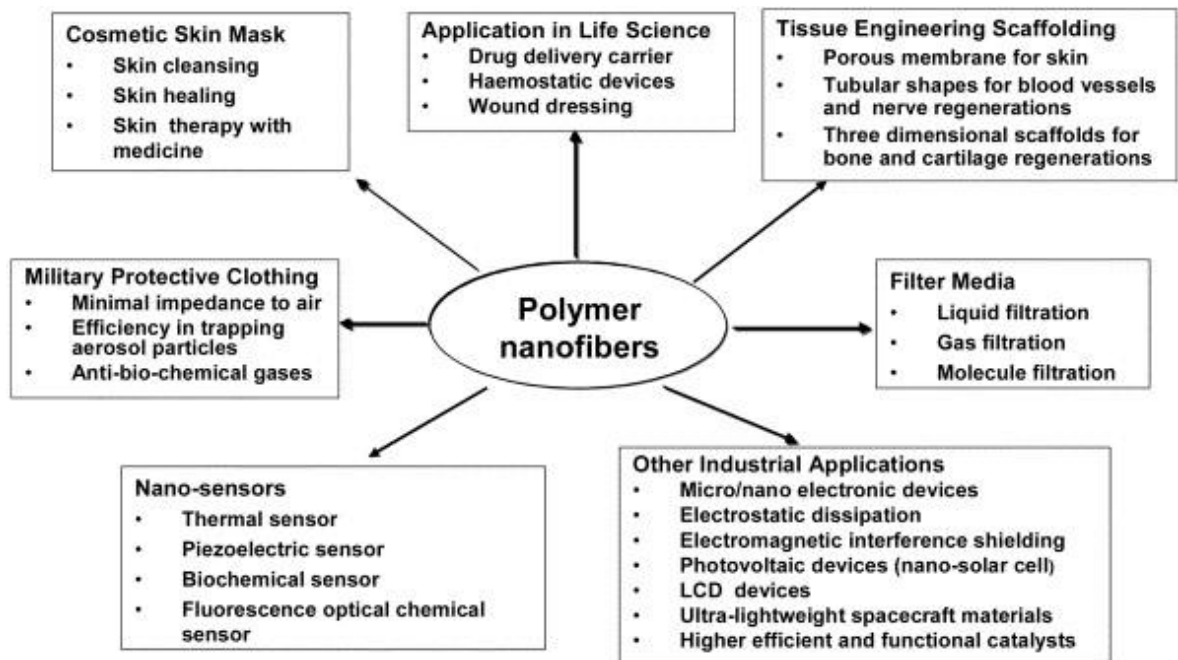
Figure 1.1 Potential applications of electrospun polymer nanofibers.
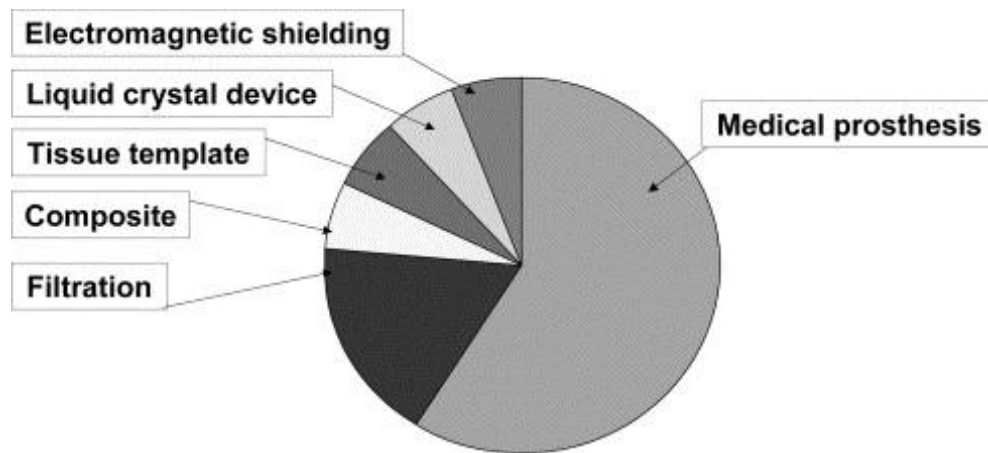
Figure 1.2 Application fields targeted by US patents on electrospun nanofibers.

Figure 1.3 by Huang et al. [20] illustrates the diversity of applications where nanofibers might be used. In addition to the applications mentioned above, numerous examples of other possible applications of nanofibers have been reported in the literature, such as: magneto-responsive fiber materials [21-24], electrical applications such as carbon nanofiber-based supercapacitors [25-28], nanofiber photovoltaic devices [29-31], catalysis applications [32-35] and superhydrophobic surfaces [24, 36-40].

One of the best representatives in this regard is shown by relevant US patents, in which most applications are in the field of filtration systems and medical prosthesis mainly grafts and vessels. Other applications which have been targeted include tissue template, electromagnetic shielding, composite delamination resistance, and liquid crystal device. A schematic diagram illustrating these patent applications is shown in Figure 1.2[20]. It should be realized that most of these applications have not reached their

industry level, but just at a laboratory research and development stage. However, their promising potential is believed to be attracting attentions and investments from academia, governments, and industry all over the world.

1.4 Objectives

In chapter 2, we present the influence the pH of the aqueous PVA/MWNT dispersion solution on the morphology and mechanical properties of the corresponding electrospun PVA/acid-treated MWNT composite nanofibers. The interfacial interactions between the carbon nanotubes and the polymer chains have been studied. And it obtained how pH value of the polymer/acid-treated MWNT solution affects the connections between the MWNT and polymer matrix. It was found that the PVA/acid-treated MWNTs (MWNTs concentration ～1.0 wt%) nanofibers at higher pH gave lower diameter than those at lower pH, due to a decreased molecular interaction between PVA and acid-treated CNTs, and thereby results in a decreased viscosity and their diameters. Moreover, the resultant nanofibers at lower pH have better mechanical properties than those at higher pH.

In chapter 3, we report a new Prussian blue nanoparticle (PBNPs) incorporated polyvinyl alcohol (PVA) composite nanofiber (*c*-PBNPs/PVA) for a rapid adsorption of cesium (Cs) from the radioactive wastewater. It was found that the prepared composite nanofiber is highly hydrophilic and water-insoluble. The *c*-PBNPs/PVA showed an excellent and faster Cs adsorption rate of 96 % after only 100 min. After the Cs adsorption test, the *c*-PBNPs/PVA composite nanofiber can be easily separated from the wastewater.

In chapter 4, cellulose acetate nanofibers (CANFs) with a mean diameter of 325±2.0 nm were electrospuned followed by deacetylation and functionalization to produce anionic cellulose nanofibers (*f*-CNFs). The noble metal nanoparticles (RuNPs and AgNPs) were successfully decorated on the *f*-CNFs by a simple wet reduction method using NaBH$_4$ as a reducing agent. TEM and SEM images of the nanocomposites (RuNPs/CNFs and AgNPs/CNFs) confirmed that the very fine RuNPs or AgNPs were homogeneously dispersed on the surface of *f*-CNFs. The weight percentage of the Ru and Ag in the nanocomposites was found to be 13.29 wt% and 22.60 wt% respectively; as confirmed by SEM-EDS analysis. The metallic state of the Ru and Ag in the nanocomposites was confirmed by XPS and XRD analyses. The usefulness of these nanocomposites was realized from their superior catalytic activity. In the aerobic oxidation of benzyl alcohol to benzaldehyde, the RuNPs/CNFs system gave a better yield of 89% with 100% selectivity. Similarly, the AgNPs/CNFs produced an excellent yield of 99% (100% selectivity) in the *aza*-Michael reaction of 1-phenylpiperazine with acrylonitrile. Mechanism has been proposed for the catalytic systems.

Reference

[1]   Doshi, J.; Reneker, D. H. Electrospinning process and applications of electrospun fibers. *J. Electrostatics.* **1995***, 2-3,* 151-160.

[2]   Ma, Z. W.; Kotaki, M.; Ramakrishna, S. Electrospun cellulose nanofiber as affinity membrane. J. Membr. Sci. **2005**, 1-2, 115-123.

[3]   Fong, H.; Chun, I.; Reneker, D. H. Beaded nanofibers formed during electrospinning. *Polymer.* **1999**, 16, 4585-4592.

[4]   Teo,. A review on electrospinning design and nanofibre assemblies. *Nanotechnology.* **2006**,17(14), R89.

[5]   Subbiah, T.; Bhat, G. S.; Tock, R. W.; Parameswaran, S.; Ramkumar, S. S. Electrospinning of nanofibers. *Journal of Applied Polymer Science.* **2005**, 96(2), 557-569. doi:10.1002/app.21481

[6]   Taylor, G. Disintegration of Water Drops in an Electric Field. *Proceedings of the Royal Society A.* **1964**, 280, 383-397.

[7]   Taylor, G. Electrically Driven Jets. *Proceedings of the Royal Society A.* **1969**, 313, 453-475.

[8]   Yarin, A. L.; Koombhongse, S.; Reneker, D. H. Bending instability in electrospinning of nanofibers. *J. Appl. Phys.* **2001***, 9,* 4836-4846.

[9]   Doshi, J; Reneker, DH. Electrospinning process and applications of electrospun fibers. *J Electrostatics.* **1995**, 35(2-3), 151− 60.

[10]   Fong, H; Chun, I; Reneker, DH. Beaded nanofibers formed during electrospinning. *Polymer.* **1999**, 40, 4585–4592.

[11] Liu, HQ; Hsieh, YL. Ultrafine fibrous cellulose membranes from electrospinning of cellulose acetate. *J of Polyer Sci Part B: Polymer Physics.* **2002**, 40, 2119–2129.

[12] Bergshoef, MM; Vancso, GJ; Transparent nanocomposites with ultrathin, electrospun Nylon-4,6 fiber reinforcement. *Adv Mater.* **1999**, 11(16), 1362–1365.

[13] Deitzel, JM; Kleinmeyer, J; Harris, D; Tan, NCB. The effect of processing variables on the morphology of electrospun nanofibers and textiles. *Polymer.* **2001**, 42, 261–272.

[14] Koombhongse, S; Liu, WX; Reneker, DH. Flat polymer ribbons and other shapes by electrospinning. *J Polymer Sci: Part B: Polymer Physics.* **2001**, 39, 2598–2606.

[15] Baumgarten, PK. Electrostatic spinning of acrylic microfibers. *J of Colloid and Interface Science.* **1971**, 36, 71–79.

[16] Demir, MM; Yilgor, I; Yilgor, E; Erman, B. Electrospinning of polyurethane fibers. *Polymer.* **2002**, 43, 3303–3309.

[17] Frenot, A.; Chronakis, I. S. Polymer nanofibers assembled by electrospinning. *Current Opinion in Colloid & Interface Science.* **2003**, 8, 64-75.

[18] Zhang, Y. Z.; Lim, C. T.; Ramakrishna, S.; Huang, Z. M. Electrospinning of gelatin fibers and gelatin/Pcl composite fibrous scaffolds. *Journal of Materials Science-Materials in Medicine.* **2005**, 16, 933-946.

[19] Sawicka, K. M.; Gouma, P. Electrospun composite nanofibers for functional applications. *Journal of Nanoparticle Research.* **2006**, 8, 769-781.

[20] Huang, Z. M.; Zhang, Y. Z.; Kotaki, M.; Ramakrishna, S. A review on polymer nanofibers by electrospinning and their applications in nanocomposites. *Composites Sci. Technol.* **2003**, 15, 2223-2253.

[21] Li, D.; Herricks, T.; Xia, Y. N. Magnetic nanofibers of nickel ferrite prepared by electrospinning. *Appl. Phys. Lett.* **2003**, 22, 4586-4588.

[22] Wang, A.; Singh, H.; Hatton, T. A.; Rutledge, G. C. Field-responsive superparamagnetic composite nanofibers by electrospinning. *Polymer.* **2004**, 16, 5505-5514.

[23] Tan, S. T.; Wendorff, J. H.; Pietzonka, C.; Jia, Z. H.; Wang, G. Q. Biocompatible and biodegradable polymer nanofibers displaying superparamagnetic properties. *ChemPhysChem.* **2005**, 8, 1461-1465.

[24] Ying, Z.; Jing, C. Z.; Jin, Z.; Yong, M. Z.; Lin, F.; Lei, J. Multifunctional carbon nanofibers with conductive, magnetic and superhydrophobic properties. *ChemPhysChem.* **2006**, 2, 336-341.

[25] Kim, C.; Yang, K. S. Electrochemical properties of carbon nanofiber web as an electrode for supercapacitor prepared by electrospinning. *Appl. Phys. Lett.* **2003**, 6, 1216-1218.

[26] Kim, C.; Kim, J. S.; Kim, S. J.; Lee, W. J.; Yang, K. S. Supercapacitors Prepared from Carbon Nanofibers Electrospun from Polybenzimidazol. *J. Electrochem. Soc.* **2004**, 5, A769-A773.

[27] Kim, C.; Choi, Y. O.; Lee, W. J.; Yang, K. S. Supercapacitor performances of activated carbon fiber webs prepared by electrospinning of PMDA-ODA poly(amic acid) solutions. *Electrochim. Acta.* **2004**, 2-3, 883-887.

[28] Kim, C. Electrochemical characterization of electrospun activated carbon nanofibres as an electrode in supercapacitors. *J. Power Sources.* **2005**, 1-2, 382-388.

[29]   Drew, C.; Wang, X. Y.; Senecal, K.; Schreuder-Gibson, H.; He, J. N.; Kumar, J.;
       Samuelson, L. A. Electrospun photovoltaic cells. *J. Macromol. Sci. -Pure Appl.*
       Chem. 2002, 10, 1085-1094.

[30]   Tomer, V.; Teye-Mensah, R.; Tokash, J. C.; Stojilovic, N.; Kataphinan, W.; Evans,
       E. A.; Chase, G. G.; Ramsier, R. D.; Smith, D. J.; Reneker, D. H. Selective emitters
       for thermophotovolataics: erbia-modified electrospun titania nanofibers. *Solar*
       Energy Mater. Solar Cells. **2005**, 4, 477-488.

[31]   Onozuka, K.; Ding, B.; Tsuge, Y.; Naka, T.; Yamazaki, M.; Sugi, S.; Ohno, S.;
       Yoshikawa, M.; Shiratori, S. Electrospinning processed nanofibrous TiO(2)
       membranes for photovoltaic applications. *Nanotechnology*. **2006**, 4, 1026-1031.

[32]   He, C. H.; Gong, J. The preparation of PVA–Pt/TiO$_2$ composite nanofiber
       aggregate and the photocatalytic degradation of solid-phase polyvinyl alcohol.
       Polym. Degrad. Stab. **2003**, 1, 117-124.

[33]   Demir, M. M.; Gulgun, M. A.; Menceloglu, Y. Z.; Erman, B.; Abramchuk, S. S.;
       Makhaeva, E. E.; Khokhlov, A. R.; Matveeva, V. G.; Sulman, M. G. Palladium
       nanoparticles by electrospinning from poly(acrylonitrile-co-acrylic acid)-PdCl2
       solutions. Relations between preparation conditions, particle size, and catalytic
       activity. *Macromolecules*. **2004**, 5, 1787-1792.

[34]   Li, D.; McCann, J. T.; Gratt, M.; Xia, Y. N. Photocatalytic deposition of gold
       nanoparticles on electrospun nanofibers of titania. *Chem. Phys. Lett.* **2004**, 4-6, 387-
       391.

[35] Wang, Z. G.; Xu, Z. K.; Wan, L. S.; Wu, J.; Innocent, C.; Seta, P. Nanofibrous membranes containing carbon nanotubes: Electrospun for redox enzyme immobilization. *Macromol. Rapid Commun.* **2006**, 7, 516-521.

[36] Acatay, K.; Simsek, E.; Ow-Yang, C.; Menceloglu, Y. Z. Tunable, superhydrophobically stable polymeric surfaces by electrospinning. *Angew. Chem. - Int. Edit.* **2004**, *39,* 5210-5213.

[37] Jiang, L.; Zhao, Y.; Zhai, J. A Lotus-Leaf-like Superhydrophobic Surface: A Porous Microsphere/Nanofiber Composite Film Prepared by Electrohydrodynamics. *Angew. Chem. -Int. Edit.* **2004**, *33,* 4338-4341.

[38] Ma, M. L.; Hill, R. M.; Lowery, J. L.; Fridrikh, S. V.; Rutledge, G. C. Electrospun poly(styrene-block-dimethylsiloxane) block copolymer fibers exhibiting superhydrophobicity. *Langmuir.* **2005**, *12,* 5549-5554.

[39] Ma, M. L.; Mao, Y.; Gupta, M.; Gleason, K. K.; Rutledge, G. C. Superhydrophobic Fabrics Produced by Electrospinning and Chemical Vapor Deposition. *Macromolecules.* **2005**, 23, 9742-9748.

[40] Singh, A.; Steely, L.; Allcock, H. R. Poly[bis(2,2,2-trifluoroethoxy)phosphazene] superhydrophobic nanofibers. *Langmuir*. **2005**, 25, 11604-11607.

[41] Ma, Z. W.; Masaya, K.; Ramakrishna, S. Immobilization of Cibacron blue F3GA on electrospun polysulphone ultra-fine fiber surfaces towards developing an affinity membrane for albumin adsorption. *Journal of Membrane Science.* **2006**, 282, 237-244.

[42] Peng, Q.; Sun, X. Y.; Spagnola, J. C.; Hyde, K. G.; Spontak, R, J.; Parsons, G, N. Atomic layer deposition on electrospun polymer fibers as a direct route to Al_2O_3 microtubes with precise wall thickness control. *Nano Letters*. **2007**, 7, 719-722.

[43] Wong, K. K. H.; Zinke-Allmang, M.; Wan, W. N^+ surface doping on nanoscale polymer fabrics via ion implantation. *Nuclear Instruments & Methods in Physics Research Section B-Beam Interactions with Materials and Atoms*. 2006, 249, 362-365.

[44] Ghosh, P. K.; Maiti, U. N.; Chattopadhyay, K. K. Structural and optical characterization of CdS nanofibers synthesized by dc-sputtering technique. *Materials Letters*. **2006,** 60, 2281-2285.

[45] Li, D.; Xia, Y. N. Direct fabrication of composite and ceramic hollow nanofibers by electrospinning. *Adv Mater*. **2004**, 14, 1151-1170.

[46] Reneker, D. H.; Yarin, A. L.; Fong, H.; Koombhongse, S. Bending instability of electrically charged liquid jets of polymer solutions in electrospinning. *J. Appl. Phys*. **2000**, 87, 4531–4547.

[47] Shin, Y. M.; Hohman, M. M.; Brenner, M. P.; Rutledge, G,C. Electrospinning: A whipping fluid jet generates submicron polymer fibers. *Appl Phys Lett*. **2001**, 78, 1149–1151.

[48] Yarin, A. L.; Koombhongse, S.; Reneker, D. H. Bending instability in electrospinning of nanofibers. *J. Appl. Phys.* **2001**, 89(5), 3018–3026.

[49] Yarin, A. L.; Koombhongse, S.; Reneker, D. H. Taylor cone and jetting from liquid droplets in electrospinning of nanofibers. *J. Appl. Phys*. **2001**, 89(9), 4836–4846.

[50] Hohman, M. M.; Shin, M; Rutledge, G.; Brenner, M. P. Electrospinning and electrically forced jets. I. Stability theory. *Physics of Fluids*. **2001**, 13, 2201–2220.

[51] Hohman, M. M.; Shin, M.; Rutledge, G.; Brenner, M. P. Electrospinning and electrically forced jets. II. Applications. *Physics of Fluids*. **2001**, 13, 2221–2236.

CHAPTER 2

Effects of pH on Electrospun PVA/acid-treated MWNT

Composite Nanofibers

CHAPTER 2

Effects of pH on Electrospun PVA/acid-treated MWNT Composite Nanofibers

2.1 Introduction

Carbon nanotubes (CNTs) have attracted great attention as ideal fillers for reinforcement because of their unique physical and mechanical properties since the discovery by Ijima [1-4]. However, poor solubility and processability of the CNTs have hindered chemical manipulations and their further uses in applications [5-7]. Thus, both chemical functionalization and noncovalent wrapping methods have been studied. As functionalization of the CNTs is growing popular in nanotechnology, many new green techniques have been employed [8]. Among the functionalization techniques, there are either acid or basic treatments, but the former is a better functionalization treatment, because after the acid-treatments, there are small changes in the physical and chemical properties of the CNTs compared to the as-grown materials. Moreover, several techniques revealed the presence of oxygen-containing functional groups, such as –COOH or $-SO_3H$ groups, on the surface of the CNTs treated with a HNO_3/H_2SO_4 mixture [9]. Up to date, PVA/CNT composite materials have been widely studied [11-14] since the hydroxyl groups of the PVA and the carboxyl groups of the modified CNTs can form strong interaction via hydrogen bonding. A. B. Dalton et al. [11] produced the super-tough carbon-nanotube fibers which possess high tensile strength of 1.8 GPa and high Young's modulus of 80 GPa with the single-walled carbon nanotube (SWNT) and

PVA by using a type of coagulation-based carbon-nanotubes spinning method to prepare these fibers. N. Lachman et al. [10] also studied the Raman response of carbon nanotube/PVA fibers under strain and found that the carboxylic groups played a major role in the stress-transfer mechanism, as they improved the transfer of stress from the matrix to the CNTs. A. Eitan et al. [15] modified the multi-walled carbon nanotubes (MWNT) by means of epoxide-based functional groups, as the MWNTs were first carboxylated along their walls, and followed by further reactions to attach diglycidyl ether of bisphenol-A-based epoxide resin, so in the case of an epoxy-based bulk polymer it is possible to obtain a covalent bond between the nanotube and the polymer matrix. Although a lot of works have been done to learn the interfacial interactions between the carbon nanotubes and the polymer chains and the load-transfer efficiency from the polymer to the carbon nanotubes, few people studied how pH value of the polymer/acid-treated MWNT solution affects the connections between the MWNT and polymer matrix. In this paper, we studied the influence the pH of the aqueous PVA/MWNT dispersion solution on the morphology and mechanical properties of the corresponding electrospun PVA/acid-treated MWNT composite nanofibers.

2.2 Experimental section

2.2.1 Materials

Poly(vinyl alcohol) (PVA) (degree of polymerization ~ 1700 and degree of hydrolysis 88%) was kindly provided by Kuraray Co. Ltd., Japan and used without

further purification. Multi-walled carbon nanotubes (MWNTs, diameter ~15–25 nm, [16]) grown by chemical vapor deposition (CVD) method were used as a nanofiller. To improve the miscibility of the MWNTs with PVA, pristine MWNTs were acid-treated using sulfuric and nitric acid solution (H_2SO_4:HNO_3 = 3:1) [9] under sonication for 3 hrs. at about 50^oC, and then kept for 1 day. Afterwards, acid-treated MWNTs were thoroughly rinsed 4 to 5 times with access amounts of deionized water until pH became neutral, and subsequently was vacuum-dried. The resultant acid-treated MWNTs were dispersed in dimethylformamide (DMF) (Wako Pure Chemical Industries, Ltd.: > 99.5%) under sonication for 3hrs, and then used as a stock solution. The MWNT concentration in the PVA/MWNT blend solutions was controlled to be 1.0 ~ 3.0 wt%. Before electrospinning, mixed solutions of PVA and MWNTs were sonicated for 3 hrs. and stirred for 24 hrs., and then electrospun to produce the PVA/MWNT composite nanofibers with different MWNT contents. The PVA was dissolved in the distilled water with different pH values ranging from 2 to 12 and mixed with different amounts of MWNTs to produce the PVA/MWNTs composite solutions, and then used for electrospinning to produce the PVA/MWNT composite nanofibers with different pHs. The concentration of aqueous PVA solution was ca. 12.0 wt%.

2.2.2 Electrospinning [17-21]

A high-voltage power supply (CPS-60 Ko22V1, Chunpa EMT Co., Republic of Korea) capable of generating voltage up to 80 kV, was used as a source of electric field. The aqueous PVA/MWNTs dispersion solutions with various pHs and MWNT contents were supplied through a plastic syringe attached to a capillary tip with inner diameter of

0.6 mm. The copper wire connected to a positive electrode (anode) was inserted into the polymer solution, and a negative electrode (cathode) was attached to a metallic collector. The collecting roller was placed at distance of 15 cm from the capillary tip, and a voltage of 12 kV was applied to the copper wire, while the receiving collector was rotating.

2.2.3 Characterization

Scanning electron microscopy (SEM, VE-8800, Keynece Co., Japan) was used to characterize the fiber morphology, average diameter and its distribution of the resultant PVA/MWNTs composite nanofibers. Transmission electron microscopy (TEM) (JEOL model 2010 FasTEM, accelerating voltage 200 kV) was used to investigate the morphologies of the pristine and the acid-treated MWNTs as well as the alignment of the MWNTs in the resulting PVA/MWNTs composite nanofibers. The Raman spectra were recorded with a Raman spectrometer (Hololab 5000, Kaiser Optical Systems Inc., USA), and argon laser at 532 nm, with a Kaiser holographic edge filter. Typically 50 mW of laser light was used at the sample with a $\times$ 50 long distance microscope objective. Integration time was around 40 s, and the spectral resolution was 1.2 cm^{-1}. The wide-angle X-ray diffraction (WAXD) experiments were performed at room temperature with nanofiber samples using a Rotaflex RTP300 (Rigaku Co., Japan) X-ray diffractometer operating at 50 kV and 200 mA. Nickel-filtered Cu K_{α} radiation was used for the measurements, along with an angular range of $5 < 2\theta < 50^{o}$. The mechanical behavior was determined by a universal testing machine (TENSILON RTC1250A, A&D Company, Ltd, Japan) under a crosshead speed 5.0 mm/min at room temperature. In according with ASTM D-638, samples were prepared in the form of a dumbbell-shape and, then, at least

five specimens were tested for tensile behavior and the average values were reported. All specimens were dried in a vacuum oven at 25 $^{\circ}$C for a day before use. Three parameters were determined from each stress-strain curves: Young's modulus, tensile strength, and elongation at break. Elastic modulus or Young's modulus is the initial slope of the stress-strain curve. Tensile strength is the stress at failure and the strain corresponding to the tensile strength is the failure strain.

2.3 Results and discussion

2.3.1 Effects of MWNT contents on PVA/MWNT composite fibers

Figure 2.1, 2.2 show SEM images and the change in average fiber diameters for the electrospun PVA/MWNT composite nanofibers with different concentrations of MWNTs. It could be seen that the PVA/MWNT nanofibers with 1.0 wt% MWNTs exhibited the smallest diameter and narrower diameter distribution, suggesting well-distribution of the MWNTs onto the PVA nanofibers. This may be attributed to the fact that the MWNTs have a good conductivity and therefore reduce an electrostatic potential to give smaller diameter during electrospinning. On the other hand, as the concentration of MWNTs increased to 2.0 and 3.0 wt%, the diameter and its distribution of the PVA/MWNT nanofibers became bigger and broader, and the surface of the fibers became rough, which was attributed to the agglomeration of the superfluous MWNTs which couldn't be wrapped by the PVA molecules, as confirmed by SEM image (Figure 2.1d). Indeed, the dispersion of the MWNTs plays a crucial role in the production of the

MWNT-containing composite nanofibers. That is, when MWNT concentration was kept at the lower level, the MWNTs could be rather evenly dispersed in the PVA matrix and were completely wrapped by the PVA polymer [22]. The presence of the MWNT and their orientation in the resulting PVA/MWNT composite fibers can be observed by TEM. As seen in Figure 2.3, TEM micrograph shows that the MWNT are embedded in the PVA fibers and not deposited on the surface of the PVA fibers during electrospinning. The MWNT are supported to align along the axis of the PVA fiber. The high electrostatic fields during electrospinning are expected to result in a favored orientation of the MWNT along the fiber axis. Moreover, the PVA matrix undergoes a drawing effect during electrospinning, which induced alignment of the MWNT along the fiber axis.
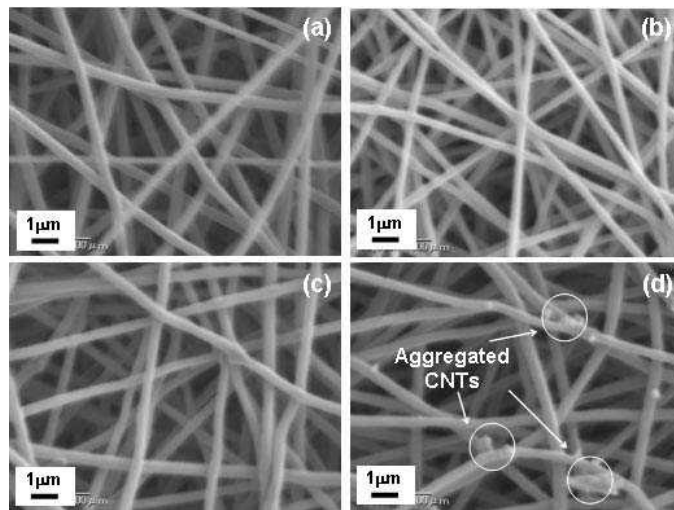
Figure 2.1 – SEM images of electrospun PVA/MWNT composite nanofibers with different MWNT concentrations: (a) pure PVA and MWNT concentrations of (b) 1.0 wt%, (c) 2.0 wt%, and (d) 3.0 wt%, respectively.
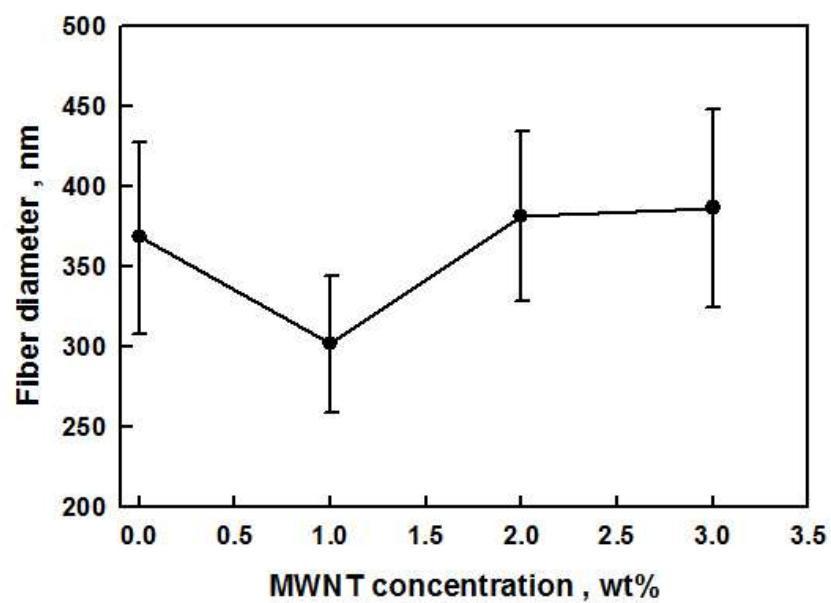
Figure 2.2 – Change in averaged diameters for the corresponding electrospun PVA/MWNT nanofibers.
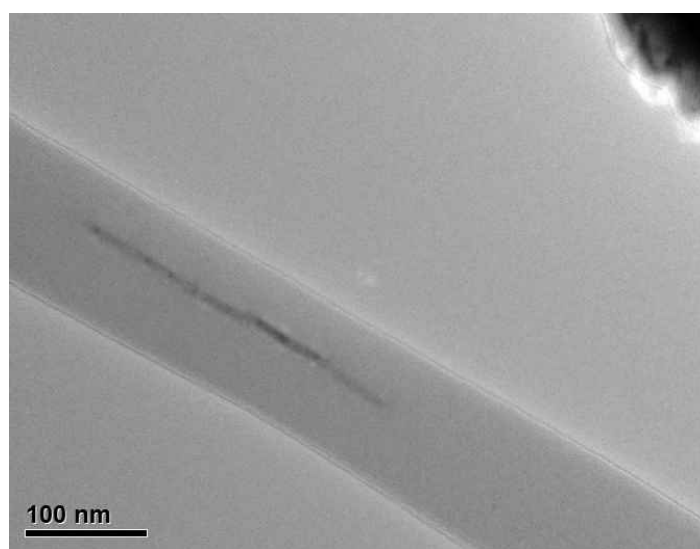
Figure 2.3 – TEM micrograph of 1 % MWNT reinforced PVA composite nanofibers produced at pH of 7.0.
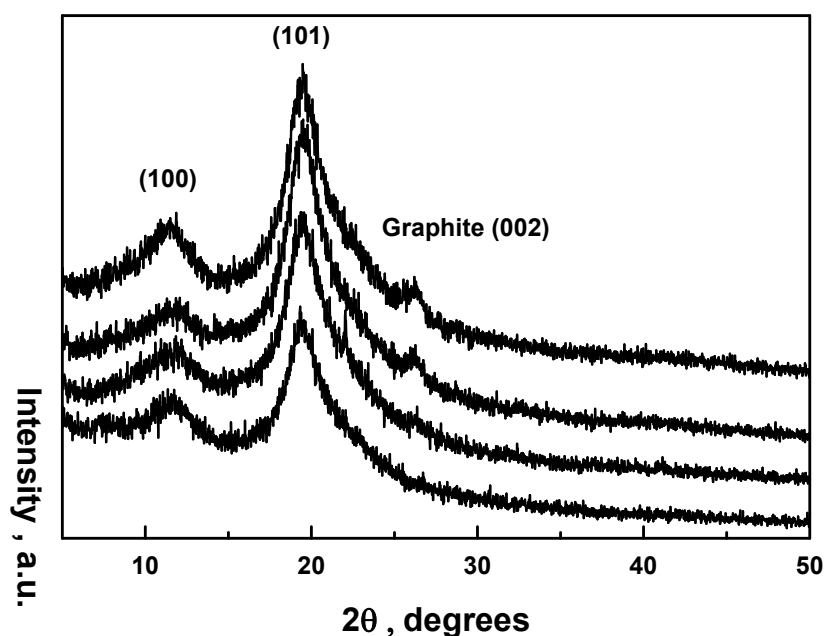
Figure 2.4 – WAXD patterns of MWNT- reinforced and as-spun PVA nanofibers, **a** pure PVA nanofibers, **b** 1% MWNT reinforced nanofibers, **c** 2% MWNT reinforced nanofibers, **d** 3% MWNT reinforced nanofibers.

The pure PVA exhibits typical peaks at 11.6^{o} and 19.5^{o}, corresponding to the (100) and (101) reflections [12], as seen in Figure 2.4. It was also found that such crystal peaks became sharper as the MWNT contents increased. The result might be attributed to enhanced alignment of the PVA macromolecules which was induced by increased solution conductivity of the PVA/MWNT solutions during electrospinning. Moreover, new peak at 26.5^{o}, corresponding to the (002) reflection, was observed in the WAXD patterns of PVA/MWNT composite nanofibers. The new peak at 26.5^{o} was due to the graphite structures of incorporated MWNTs [23]. Moreover, the peak intensity at 26.5^{o} became evident gradually as the MWNT contents increased.
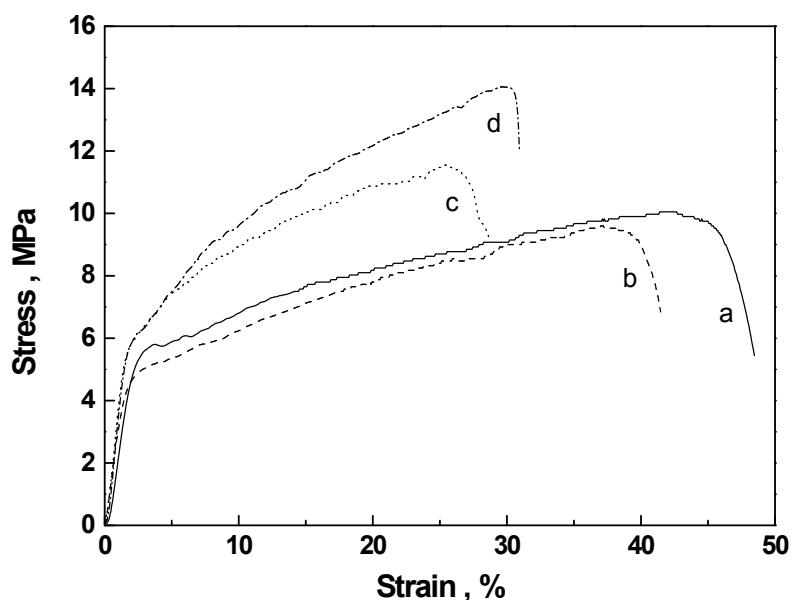
Figure 2.5 – Typical stress-strain curves of MWNT- reinforced and as-spun PVA nanofibers, a pure PVA nanofibers, b 1% MWNT reinforced nanofibers, c 2% MWNT reinforced nanofibers, d 3% MWNT reinforced nanofibers.

Figure 2.5 shows stress-strain curves for the MWNT-reinforced PVA composite fibers with different MWNT contents. As it can be seen from the figure, the mechanical properties of the 1.0 wt% MWNT-reinforced PVA fibers were similar to those of the pure PVA fibers, while the mechanical properties increased gradually when the MWNT contents exceeded 1.0 wt%. On the other hand, above MWNT content of 3.0 wt%, we failed to produce the PVA/MWNT composite fibers due to severe aggregation of MWNTs in PVA/MWNT solution.

2.3.2 pH Effects on PVA/MWNT composite fibers

We have further studied the pH effects of aqueous PVA/MWNT solution on the morphology and mechanical properties of the corresponding electrospun PVA/acid-treated MWNT composite nanofibers. Here, we chose an optimum MWNT concentration around 1.0 wt% in the PVA/MWNT solutions, because it produced the smaller diameter and its narrower distribution of the resulting PVA/MWNT composite fibers. The pH values of PVA/MWNT aqueous solutions were varied ranging from 2.0 to 12.0 in order to explore the molecular interactions between PVA and acid-treated MWNTs via hydrogen bonding.

Figure 2.6 shows SEM images (top) and the change in averaged diameters (bottom) for the PVA/MWNT composite nanofibers (MWNT concentration $\approx$ 1.0 wt%) produced at various pHs. It was found that the PVA/MWNT nanofibers at higher pH gave lower diameter than those at lower pH, probably due to the decreased hydrogen-bonding interactions between PVA and acid-treated MWNTs, and thereby results in a decreased viscosity and their diameters. The detailed solution properties, such as solution viscosity, surface tension, conductivity, of the PVA/MWNT composite solutions should be further studied. On the other hand, Figure 2.6d shows that the PVA/MWNT composite nanofibers produced at alkaline environment are very rough because MWNTs easily tend to form agglomeration via Van der Waals attractions between MWNTs, but not interact with PVA.
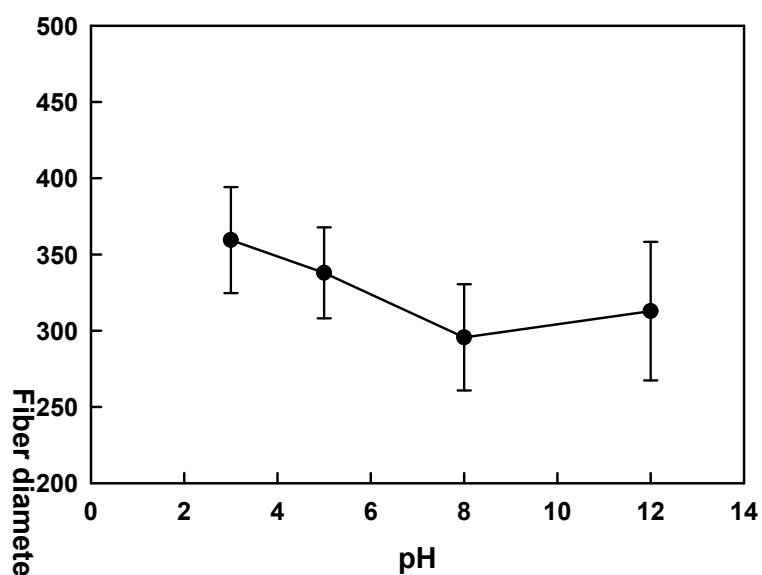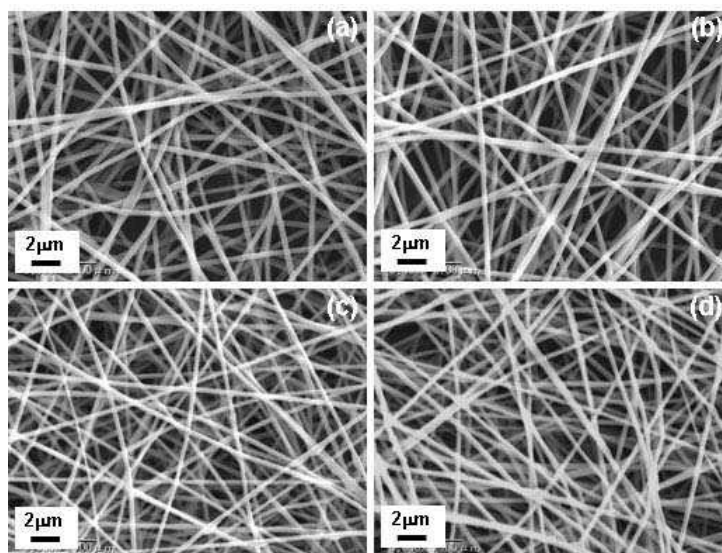
Figure 2.6 – SEM images for electrospun PVA/MWNT composite nanofibers produced at various pHs: (a) 2.0, (b) 5.0, (c) 8.0, and (d) 12.0, respectively (top). Change in averaged diameters for the corresponding electrospun PVA/MWNT composite nanofibers (bottom). The concentration of the MWNTs was fixed at 1.0 wt%.
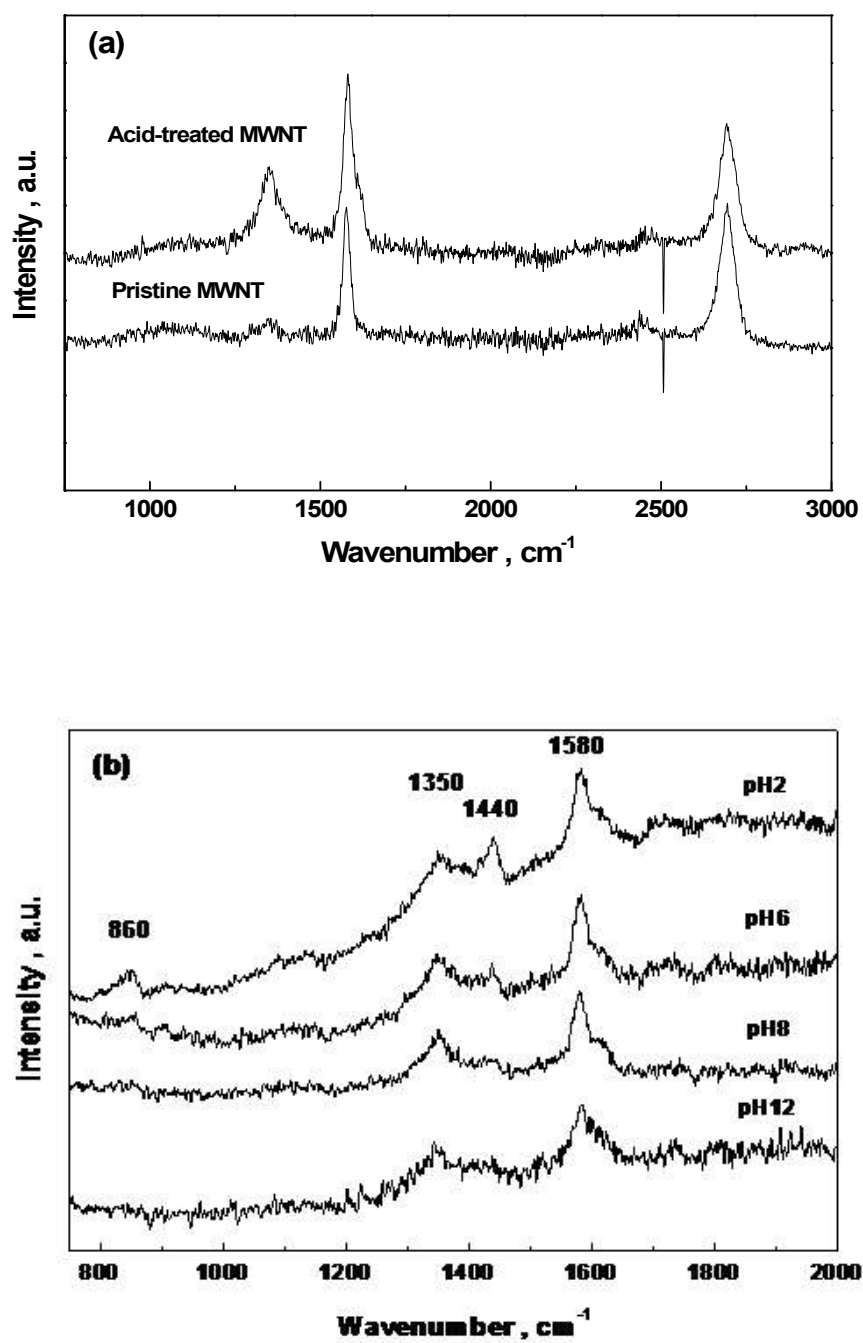
Figure 2.7 – (a) Raman spectra of pristine and acid-treated MWNTs, (b) Raman spectra of the 1 wt% MWNT reinforced PVA nanofibers produced at different pH values.

The presence of interfacial interactions between acid-treated MWNTs and PVA molecular chains in the resultant PVA/acid-treated MWNT composite nanofibers prepared from various pHs was characterized by Raman spectroscopy. The Raman spectra of the PVA/acid-treated MWNT composite nanofibers were presented in Figure 2.7. In general, the peak for Disorder Induced Mode (D) is at 1350 cm^{-1} which provides the information on the crystallinity of the sample and the defects in the sp^2 orbital of carbon in the nanotubes [24,25]. The other characteristic peak is Tangential Mode (TM) which is observed between 1590 and 1570 cm^{-1}. TM band can be used to differentiate metallic from semi-conducting nanotubes. We were able to see two characteristic bands of MWNT in the resulting PVA/acid-treated MWNT nanofibers except for pure electrospun PVA nanofiber, suggesting that the MWNTs were incorporated into the PVA fibers during electrospinning. Moreover, Raman spectra of 1.0 wt% MWNT-reinforced PVA produced at pH of 2 and 6 showed remarkably enhanced peaks at 1440 and 860 cm^{-1}, compared to those produced at pH of 8 and 12, indicating the strong interactions between the PVA and acid-treated MWNT.

As expected, pH variation of aqueous PVA/MWNT dispersion solutions can affect the dispersion of the MWNTs as well as the interaction between the PVA and acid-treated MWNT in the resultant PVA/MWNT composite nanofibers. WAXD analysis of PVA/MWNT composite nanofibers produced at various pHs were carried out. As a result, the PVA/MWNT composite nanofibers exhibited the same crystalline microstructure as pure PVA (data not shown). These peaks were less ordered and also depended on the pH of PVA/MWNT aqueous solutions.
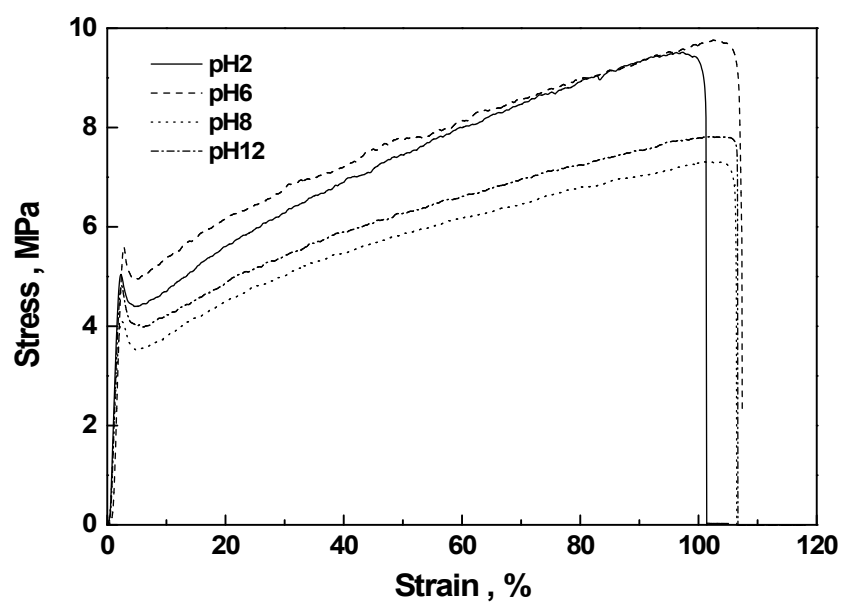
Figure 2.8 – Typical stress-strain curves of 1wt% MWNT reinforced PVA nanofibers at different pH values.

	Young's modulus / MPa	Tensile strength / MPa	Elongation at break / %
pH2	293±40	9.3±0.6	96.8±7
pH6	355±30	9.8±0.1	96.3±7
pH8	272±40	7.4±0.2	104.4±5
pH12	316±20	7.5±0.2	98.8±6

Table 2.1 – Mechanical properties of 1% MWNT reinforced PVA nanofibers at different pH values.

The mechanical properties of the 1.0 wt% acid-treated MWNT reinforced PVA nanofibers produced under various pHs were investigated, and the obtained stress-strain curves were shown in Figure 2.8. As it can be seen from the figure, the 1.0 wt% MWNT reinforced PVA fibers produced at pH of 2 and 6 have the similar mechanical properties, while the tensile strength of 1.0 wt% MWNT reinforced fibers produced at pH of 8 and 12 decreased to about 20%. The detailed data were summarized in Table 1. However, the tensile strength (~9.5 MPa) of the fibers produced at pH of 2 and 6 was 25% higher than that (~7.5 MPa) produced at pH of 8 and 12. All the results indicated that the PVA formed better interaction with the acid-treated MWNT in the nanofibers, which may be attributed to the stronger hydrogen bonding in the acidic circumstance compared to the alkaline circumstance.

2.4 Conclusions

We have successfully prepared the PVA/MWNT composite nanofibers by electrospinning method, and studied the effects of MWNT concentration and pH on the morphologies, microstructures and mechanical properties of the resultant PVA/MWNT composite nanofibers. SEM analysis demonstrated that the PVA/MWNT nanofibers with acid-treated MWNTs of 1.0 wt% gave rather smaller diameter and narrower distribution, suggesting well-distribution of the MWNTs onto the PVA nanofiber matrix, which was also confirmed by TEM analysis. In addition, it was found that the PVA/acid-treated MWNT (MWNTs concentration ~ 1.0 wt%) nanofibers at higher pH gave lower diameter than those at lower pH, due to a decreased molecular interaction between PVA and acid-treated CNTs, and thereby results in a decreased viscosity and their diameters. Moreover, the resultant nanofibers at lower pH have better mechanical properties than those at higher pH. Also, the crystalline structures of the PVA/MWNT nanofibers were altered when the pH of the PVA/MWNT dispersion solutions was changed.

Reference

[1] Iijima, S. Helical microtubules of graphitic carbon. *Nature*. **1991,** 354, 56–58.

[2] Wagner, H. D.; Lourie, O.; Feldman, Y.; Tenne, R. Stress-induced fragmentation of multiwall carbon nanotubes in a polymer matrix. *Appl. Phys. Lett.* **1998**, 72, 188-190.

[3] Bower, C.; Rosen, R.; Jin, L.; Zhou, O. Deformation of carbon nanotubes in nanotube-polymer composites. *Appl. Phys. Lett.* **1999**, 74, 3317-3319.

[4] Wei, K.; Xia, J. H.; Kim, B. S.; Kim, I. S. Multiwalled carbon nanotubes incorporated Bombyx mori silk nanofibers by electrospinning. *J. Polym. Res.* **2011**, 18(4) , 579-585.

[5] Girifalco, L. A.; Hodak, M.; Lee, R. S. Carbon nanotubes, buckyballs, ropes, and a universal graphitic potential. *Phys. Rev. B*. **2000**, 62, 13104-13110.

[6] Sabba, Y.; Thomas, H. L. High concentration dispersion of single-wall carbon nanotubes. *Macromolecules*. **2004**, 37, 4815-4820.

[7] Hinds, B. J.; Chopra, N.; Rantell, T.; Andrews, R.; Gavalas, V.; Bachas, L. G. Aligned multiwalled carbon nanotube membranes. *Science*. **2004**, 303, 62-65.

[8] Zhang, F.; Zhang, H.; Zhang, Z. W.; Chen, Z. M.; Xu, Q. Modification of carbon nanotubes: water-soluble polymers nanocrystal wrapping to periodic patterning with assistance of supercritical CO_2. *Macromolecules*. **2008**, 41(12), 4519-4523.

[9] Musso, S.; Porro, S.; Vinante, M.; Vanzetti, L.; Ploeger, R.; Giorcelli, M.; Possetti, B.; Trotta, F.; Pederzolli, C.; Tagliaferro, A. Modification of MWNTs obtained by thermal-CVD. *Diamond and Relat. Mater*. **2007**, 16, 1183-1187.

[10] Lachman, N.; Bartholome, C.; Miaudet, P.; Maugey, M.; Poulin, P.; Wagner, H. D. Raman response of carbon nanotube/PVA fibers under strain. *J. Phys. C*. **2009**, 113(12), 4751-4754.

[11] Dalton, A. B.; Collins, S.; Munoz, E.; Razal, J. M.; Ebron, V. H.; Ferraris, J. P.; Coleman, J. N.; Kim, B. G.; Baughman, R. H. Super-tough carbon-nanotube fibres. *Nature*. **2003**, 423(12), 703.

[12] Guerrini, L. M.; de Oliveira, M. P.; Branciforti, M. C.; Custodio, T. A.; Bretas, R. E. S. Thermal and structural characterization of nanofibers of poly(vinyl alcohol) produced by electrospinning. *J. Appl. Polym. Sci*. **2009**, 112, 1680-1687.

[13] Su, J. X.; Wang, Q.; Su, R.; Wang, K.; Zhang, Q.; Fu, Q. Enhanced compatibilization and orientation of polyvinyl alcohol/gelatin composite fibers using carbon nanotubes. *J. Appl. Polym. Sci*. **2008**, 107, 4070-4075.

[14] Zhao, B.; Wang, J.; Li, Z. J.; Liu, P.; Chen, D.; Zhang, Y. F. Mechanical strength improvement of polypropylene threads modified by PVA/CNT composite coatings. *Materials Letters*. **2008**, 62, 4380-4382.

[15] Eitan, A.; Jiang, K.; Dukes, D.; Andrews, R.; Schadler, L. S. Surface modification of multiwalled carbon nanotubes: toward the tailoring of the interface in polymer composites. *Chemical Materials*. **2003**, 15, 3198-3201.

[16] Kim, Y. A.; Hayashi, T.; Endo, M.; Kaburagi, Y.; Tsukada, T.; Shan, J.; Osato, K.; Tsuruoka, S. Synthesis and structural characterization of thin MWCNTs with a partially facetted cross section. *Carbon*. **2005**, 43, 2243-2250.

[17]   Park, J. C.; Ito, T.; Kim, K. O.; Kim, K. W.; Kim, B. S.; Khil, M. S.; Kim, H. Y.; Kim, I. S. Electrospun poly(vinyl alcohol) nanofibers: effects of degree of hydrolysis and enhanced water-stability. *Polymer Journal*. **2010**, 42, 273-276.

[18]   Ohsawa, O.; Lee, K. H.; Lee, S. M.; Kim, B. S.; Kim, I. S. Preparation, Characterization of polyketone (PK) fibrous membrane via electrospinning. *Polymer*. **2010**, 51, 2007-2010.

[19]   Kim, C. K.; Kim, B. S.; Sheikh, F. A.; Lee, U. S.; Khil, M. S.; Kim, H. Y. Amphiphilic, Poly(vinyl alcohol) hybrids and electrospun nanofibers incorporating polyhedral oligosilsesquioxane. *Macromolecules*. **2007**, 40, 4823-4828.

[20]   Kim, B. S.; Kimura, N.; Kim, H. K.; Watanabe, K.; Kim, I. S. Thermal insulation, antibacterial and mold properties of breathable nanofiber-laminated wallpapers. *J. Nanosci. Nanotech.* **2011**, 11(6), 4929-4933.

[21]   Kim, B. S.; Kim, I. S. Recent nanofiber technologies. *Polym. Rev*. **2011**, 51(3), 288-308.

[22]   Jeong, J. S.; Moon, J. S.; Jeon, S. Y.; Park, J. H.; Alegaonkar, P. S.; Yoo, J. B. Mechanical properties of electrospun PVA/MWNTs composite nanofibers. *Thin Solid Films*. **2007**, 515, 5136-5141.

[23]   Ohta, T.; Ito, T.; Shimizu, M.; Tauchi, L.; Nguyen-Tran, H. D.; Park, J. C.; Kim, B. S.; Kim, I. S.; Ohta, K. Development of novel synthetic method of carbon nanotubes from electrospun polystyrene fibers by using microwave heating. *Polym. Adv. Technol.* **2011**, 22(12), 2653-2658.

[24] Li, M.; Kim, I. H.; Jeong, Y. G. Cellulose acetate/multiwalled carbon nanotube nanocomposites with improved mechanical, thermal, and electrical properties. *J. Appl. Polym. Sci.* **2010**, 118, 2475–2481.

[25] Tan, P.; Dimovski, S.; Gogotsi, Y. Raman scattering of non-planar graphite: arched edges, polyhedral crystals, whiskers and cones. *Philos. Trans. R. Soc. A: Math. Phys. Eng. Sci.* **2004**, 362, 2289-2310.

[26] Filho, A. G. S.; Jorio, A.; Samsonidze, G. G.; Dresselhaus, G.; Saito, R.; Dresselhaus, M. S. Raman spectroscopy for probing chemically/physically induced phenomena in carbon nanotubes. *Nanotechnology*. **2003**, 14(10), 1130-1139.

CHAPTER 3

Highly hydrophilic water-insoluble nanofiber composite as an efficient and easily-handleable adsorbent for a rapid adsorption of cesium from radioactive wastewater

CHAPTER 3

Highly hydrophilic water-insoluble nanofiber composite as an efficient and easily-handleable adsorbent for a rapid adsorption of cesium from radioactive wastewater

3.1 Introduction

A catastrophic earthquake and tsunami occurred on March 11, 2011, which caused a huge destruction in northeastern Japan. Undesirably, the Fukushima Daiichi Nuclear Power Plant (FDNPP) was also severely damaged[1]. As a consequence, there have been continued spills of radioactive isotopes such as ^{90}Sr, ^{131}I, ^{134}Cs and ^{137}Cs contaminated water from the FDNPP[2]. Among the radioactive materials, radiocesium has a long-term of problem due to its long physical half-life (2 years for ^{134}Cs and 30.1 years for ^{137}Cs) and its high biological availability[3,4]. Indeed, this radiocesium (^{134}Cs and ^{137}Cs) is highly harmful to the living organisums. To overcome this issue, several Cs adsorbents have been reported but only very few of them are highly efficient and selective. Among them, ferric hexacyanoferrate ($Fe_4^{III}[Fe^{II}(CN)_6]_3$) is also known as Prussian blue (PB), often used as an efficient adsorbent for the removal of radioactive Cs from the wastewater[5,6]. Very recently, the Japanese National Institute of Advanced Industrial Science and Technology (AIST) has developed PB nanoparticles (PBNPs) with the particle size of 10-20 nm[7]. Interestingly, due to the high specific surface area, the PBNPs has showed an excellent adsorption efficiency of Cs (about 100%)[8]. However, since the size of the PBNPs is too small, the recovery of the PBNPs (after the adsorption

41

of Cs) is very complicated which causes more problems to the living organisms and the environment[9]. Reda et al.,[10] has prepared magnetic hexacyanoferrate(II) polymeric nanocomposite for the separation of Cs from radioactive wastewater. However, during the process, these materials often suffer from the slower Cs adsorption rate and leaching of PBNPs from the polymeric supports into wastewater. Very recently, carbon materials have been played a tremendous role as support for various MNPs including PBNPs[11,12]. Hongjun et al.,[13] has prepared magnetic Prussian blue/graphene oxide nanocomposites for removal of radioactive Cs from wastewater. In spite of the higher activity, these composite materials are highly expensive and toxic. More importantly, recovery of these nanocmposites is complicated and expensive[14]. Therefore, developing an efficient, stable and easily handlable PBNPs-based material for the removal of Cs remains an highly demanding issue.

Recently, polymer nanofibers prepared via electrospinning technique have played tremendous role as a support in a wide range of applications[15]. Particularly, the metal NPs-based composite nanofibers have been attracting more attention in various fields because of their high surface area, cost-effectiveness and easy-handling[16]. Certainly, metal NPs-based PVA composite nanofibers have been extensively used for several applications[17,18]. In fact, PVA is largely available, highly hydrophilic, easily processable, biocompatible, non–toxic and chemical resistive. Dian and co-workers[19] have prepared AgNPs embedded electrospun PVA nanofibers composite (AgNPs/PVA) for the SERS study applications. They found that the AgNPs/PVA composite is highly responsible and the composite can be easy handled and disposed. Based on the previous reports, we presumed that the PBNPs based on PVA nanocomposite can exhibit higher

activity and overcome the drawbacks such as slower Cs adsorption rate, less stability and the difficulties of handling. Herein, we report a new PBNPs-based PVA composite nanofiber (*c*-PBNPs/PVA) for the adsorption of Cs from radioactive wastewater. The resultant nanocomposite (*c*-PBNPs/PVA) was completely characterized by various micro and spectroscopic methods. Inductive coupled plasma-mass spectroscopy (ICP-MS) was used to measure the Cs adsorption activity of the *c*-PBNPs/PVA in wastewater.

3.2   Experimental section

3.2.1   Materials

PVA [degree of hydrolysis = 88%, degree of polymerization (DP) = 1700] was provided by Kuraray Co. Ltd., Japan. Aqueous solution containing 8 wt% of PBNPs (particle size: 10-20 nm) was provided by Kanto Chemical Co., Inc, Japan. Glutaraldehyde solution (GA, 50% in water) was purchased from Sigma-Aldrich. 37% HCl, 99.9% $CsNO_3$ and 2% HNO_3 were purchased from Wako pure chemicals, Japan. All chemicals were used as-received without further purification.

3.2.2   Preparation of *c*-PBNPs/PVA composite nanofiber

3.2.2.1   Preparation of PVA/PBNPs/GA solution

In order to prepare a good PBNPs-based PVA composite nanofiber, dispersibility of the PBNPs into the PVA solution is most important. First, a 1.2 g of PVA (12 wt%) was dissolved in 10 mL of distilled water and the solution mixture was stirred at 80°C for

3 h. After cooling to 27$^{\text{o}}$C, a 24 wt% of PBNPs (based on the wt% of PVA solution) was mixed into the resultant PVA solution (12 wt%) and stirred at 27$^{\text{o}}$C for 24 h. Finally, a 12.5 wt% of GA (based on the wt% of PVA) was mixed into the above resultant mixture (PVA/PBNPs solution) to obtain a homogeneous PVA/PBNPs/GA solution. The resultant PVA/PBNPs/GA solution was used as an electrospinning solution for the preparation of nanofiber composite.

3.2.2.2 Electrospinning

A high-voltage power supply (Har-100*12, Matsusada Co., Tokyo, Japan), capable of generating voltages up to 100 kV, was used as the source of the electric field. The above obtained PVA/PBNPs/GA solutions were poured in a 5 mL plastic syringe attached to a capillary tip of about 0.6 mm in inner diameter. The Cu wire connected to an anode was inserted into the polymer solution, and a cathode was attached to a grounded rotating metallic collector wrapped with cellulose nonwoven. The tip to collector distance (TCD) was 12 cm and the applied voltage was 10 kV. All the processes were carried out at 27$^{\text{o}}$C.

3.2.2.3 Cross-linking process

Since the PVA is highly soluble in water, a post cross-linking was carried out for the resultant nanofiber composites (PBNPs/PVA/GA nanofiber) to improve the water resistance property of the PVA. In the typical experiment, all the obtained electrospun nanofibers were exposed to HCl vapor for 30s. In order to produce HCl vapor, Conc. HCl

was heated at 30°C. Scheme 3.1 shows the schematic illustration for the preparation of *c*-PBNPs/PVA composite nanofibers.
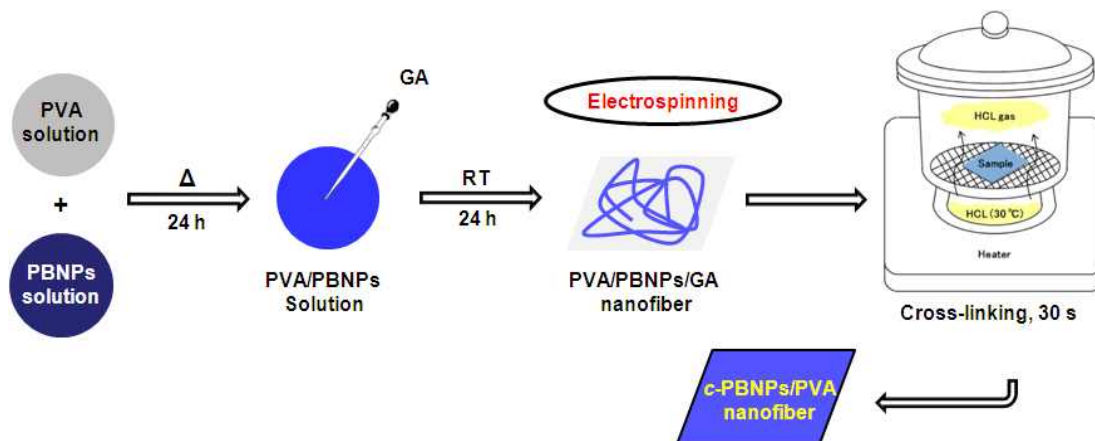
Scheme 3.1 – Schematic illustration for the preparation of *c*-PBNPs/PVA composite nanofiber.

3.2.3 Characterization

PVA solution properties such as viscosity, surface tension and electrical conductively were measured with a viscometer (DV-1, Brookfield Co., Stoughton, MA, USA), a surface tension meter (CBVP-Z, Kyowa Interface Science Co., Ltd, Japan) and a conductivity meter (D-54, HORIBA, Ltd., Japan), respectively. The morphology of electrospun composite nanofibers was characterized by scanning electron microscopy (SEM, JSM-6010LA, JEOL, Japan) and transmission electron microscopy (TEM, 2010 Fas TEM, JEOL, Japan, accelerating voltage 200 kV). The crystalline nature of the electrospun composite nanofibers was investigated using wide angle X-ray diffraction (XRD, Rotaflex RTP300, Rigaku, Japan) operating the diffractometer at 40 kV and 150

mA, using Cu Ka radiation. The scans were recorded over the range 2θ = 10-60°. To confirm the cross-linking of PVA with GA, Fourier Transform Infrared spectra (FT-IR, IRPrestige-21, Shimadzu Co., Japan) were recorded for composite nanofibers. The FT-IR spectra were recorded from 600 to 4000 cm^{-1} at a resolution of 4 cm^{-1}. The Cs adsorption activity of c-PBNPs/PVA was measured by using Inductively Coupled Plasma Mass Spectrometry (ICP-MS, NexION 300D, PerkinElmer Japan Co., Ltd., Japan). The leaching of PBNPs from the c-PBNPs/PVA was analyzed by UV-Vis spectro-photometer (Hitachi U-3500 UV-Vis spectrophotometer).

3.2.4 Cs adsorption test

A 1.0 ppm of Cs aqueous solution was prepared by adding 1.5 mg of $CsNO_3$ in 1 L of Millipore water. 1 mg of c-PBNPs/PVA composite sheet was soaked in 10 mL of 1.0 ppm Cs solution at 27°C. Subsequently, the test solution was shacked for appropriate times (10, 30 and 100 min) at 600 r.p.m using multi shaker (MS-300, AS ONE Corporation., Japan). Then the c-PBNPs/PVA composite nanofiber sheets were removed and the solution was analyzed by ICP-MS. The adsorption rate (A, %) was calculated using the following equation:

$$A = 100 - \frac{A_b}{A_a} \cdot 100$$

where A_b and A_a are the concentration of Cs before and after test, respectively.
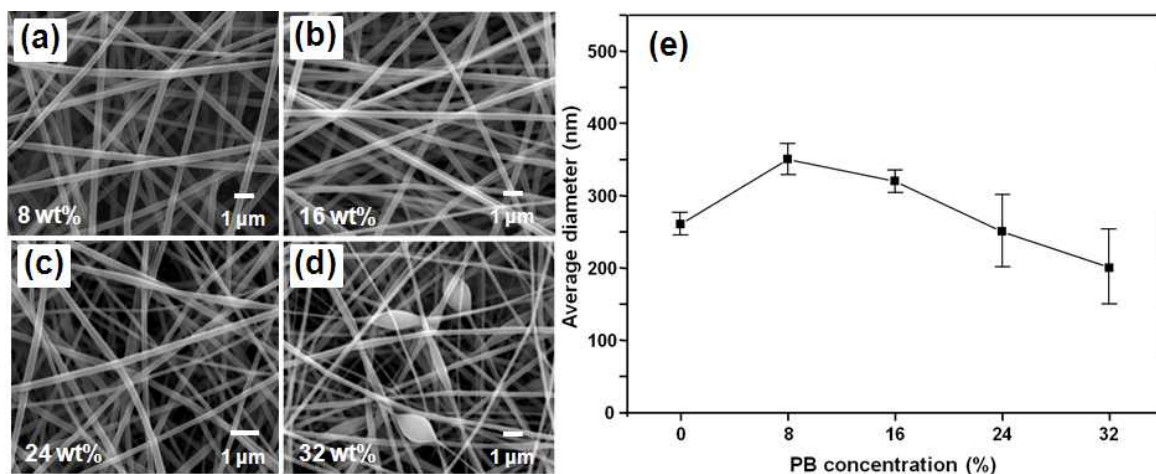
Figure 3.1 – SEM images of *c*-PBNPs/PVA composite fibers with PBNPs wt% of (a) 8%, (b) 16%, (c) 24% and (d) 32%, and (e) fiber diameters of the corresponding *c*-PBNPs/PVA composite fibers.
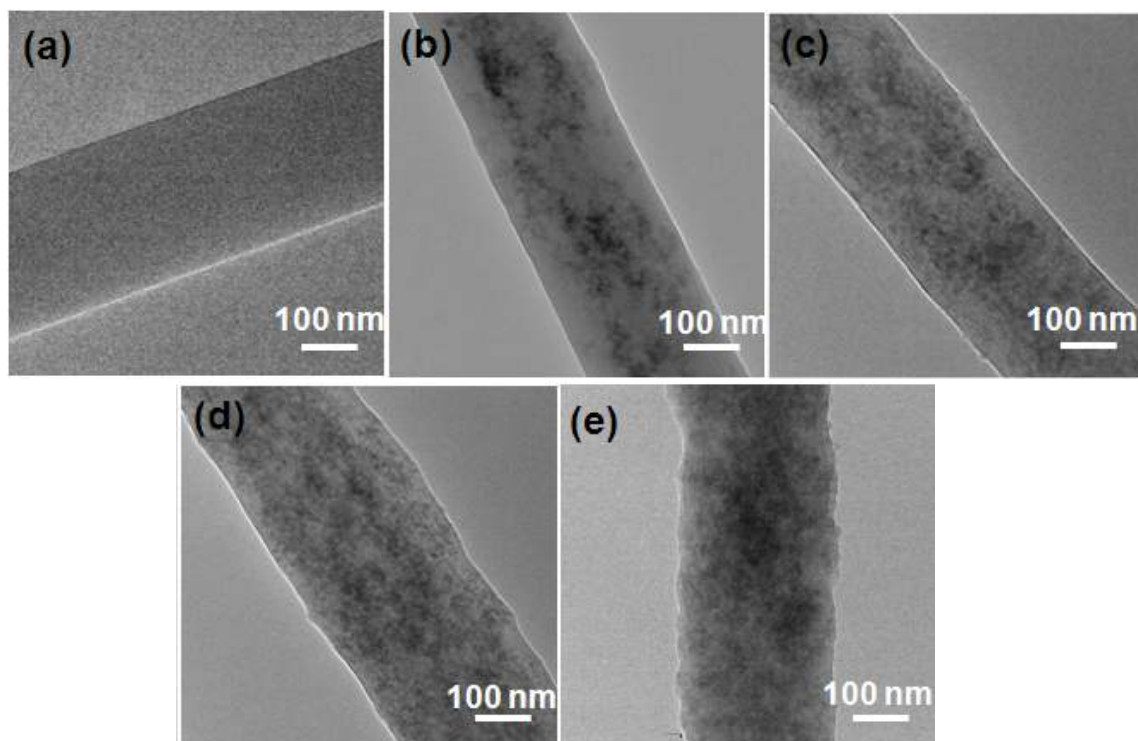
Figure 3.2 – TEM images of (a) pure PVA and *c*-PBNPs/PVA composite fibers with PBNPs wt% of (b) 8%, (c) 16%, (d) 24% and (e) 32%.

3.3 Results and discussion

3.3.1 Optimization of electrospinning conditions

In our very recent course of investigation, we have optimized the electrospinning conditions for the preparation of PVA nanofibers and also the effect of PVA solution properties on the spinnability of PVA were studied[20]. The same optimized conditions were adopted for the preparation of PVA nanofibers. In addition, to obtain a water-insoluble and highly hydrophilic PBNPs-based PVA composite nanofiber with a very fine morphology, other important parameters such as wt% of PVA, PBNPs and GA, and cross-linking time were extensively optimized. Initially, the wt% of PVA was optimized and found that the morphology of the PVA fiber is highly depended on the concentration of PVA solution. A 12 wt% of PVA was found to be the optimum concentration since it produced continuous and homogeneous fibers without beads. Whereas, when the concentration of PVA was 13 wt% or high, the beads and fibers coexisted in the SEM images (data not shown). Subsequently, the wt% of PBNPs was optimized; as consequences, higher amount of 24 wt% PBNPs (based on PVA wt%) could be successfully incorporated into the PVA fibers (Figure 3.1c). When the amount of PBNPs was 32 wt%, the spinning was discontinuous and the morphology of the fibers were irregular and rough (Figure 3.1d and Figure 3.2e). This is probably due to the aggregation of PBNPs at the higher concentrations (Figure 3.1 and 3.2)[21]. However, as expected, the average diameter of the c-PBNPs/PVA composite nanofibers decreased with increasing the concentration of the PBNPs (Figure 3.1e), and this value was found to be 260, 350, 320, 250 and 200 nm for the PBNPs concentrations of 0, 8, 16, 24 and 32 wt%,

respectively. It is clear that the electrical conductivity of the PBNPs-PVA solution played a crucial role on the diameter of the PBNPs/PVA nanofibers (Figure 3.3b)[22]. For more information about the properties of PBNPs/PVA solutions such as viscosity, electrical conductivity and surface tension, please refer Figure 3.3(a-c) in supporting information. Not surprisingly, as-spun pure PVA nanofibers are readily soluble in water at room temperature ($27^{o}C$). Therefore, to improve the water resistance property of composite nanofibers, we carried out a post cross-linking process for the nanofiber composites using GA and HCl vapor as the cross-linker and catalyst, respectively[23]. Prior to the cross-linking process, the wt% of GA (2.5, 7.5, 12.5 and 17.5 wt%) and cross-linking time (10, 30 and 50 s) were optimized. Interestingly, when the GA content was 12.5 wt% and the cross-linking time was 30 s, the fiber morphology and the average diameter of c-PBNPs/PVA were not changed much (Figure 3.4). Moreover, the FT-IR spectra and the water contact angle test showed that the 12.5 wt% of GA is good enough for the cross-linking of PVA (Figure 3.5 and Figure 3.6). Based on these results, the following solution properties and electrospinning conditions were shown to result in the formation of thinner and regular *c*-PBNPs/PVA composite fiber: 12 wt% of PVA, 24 wt% of PBNPs (based on PVA concentration), 12.5 wt% of GA and the cross-linking time is 30 s. The above resultant *c*-PBNPs/PVA composite fiber was characterized in detail by various spectroscopic and microscopic techniques. We also examined the electrospinning condition for the preparation of PBNPs/polyurethane and PBNPs/poly(vinylidene fluoride) composites, but homogeneous solution was not obtained because of low compatibility of organic solvents (*N,N*-dimethylformamide and methyl ethyl ketone) (data not shown).
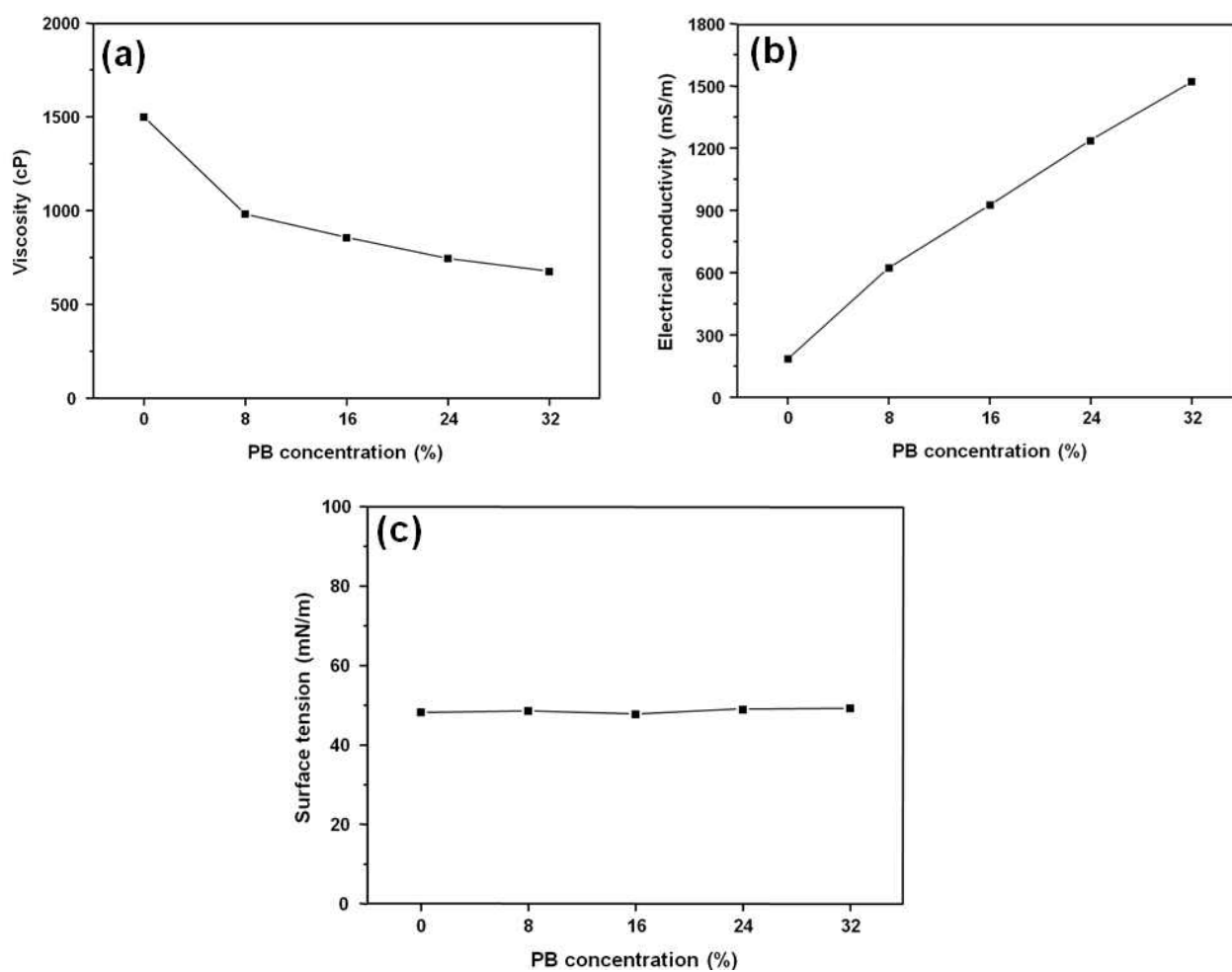
Figure 3.3 (a) Viscosity, (b) electrical conductivity and (c) surface tension of the PVA solution at different concentrations of PBNPs.
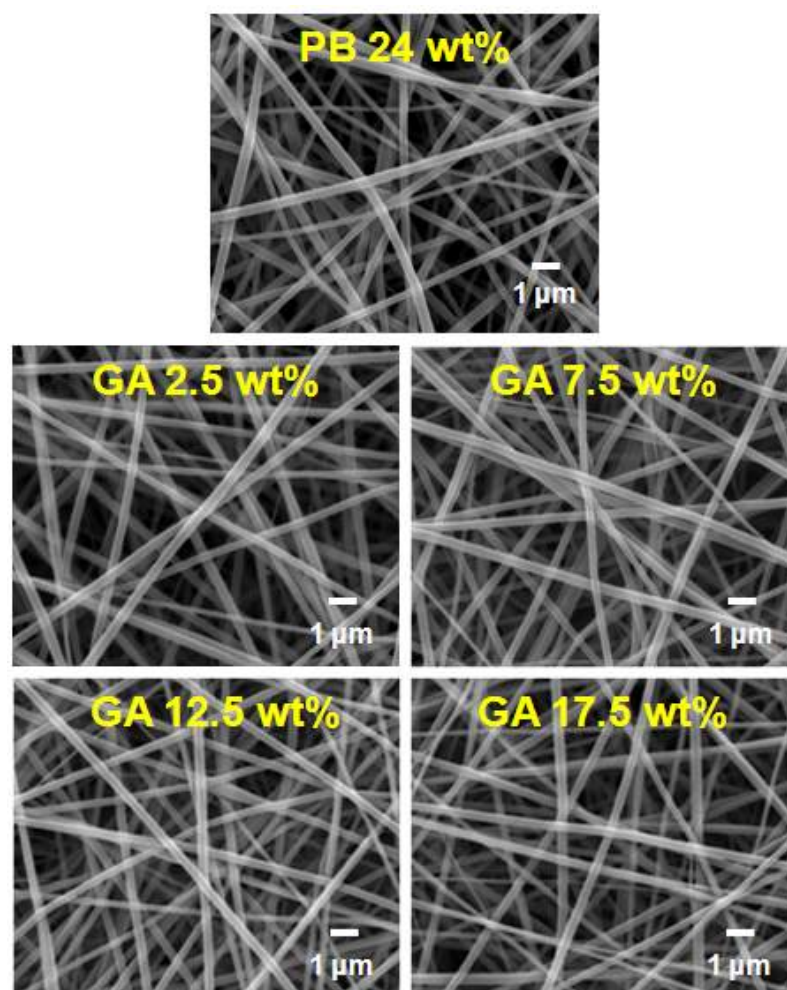
Figure 3.4 SEM images of *c*-PBNPs/PVA composite nanofibers at different concentrations of GA.
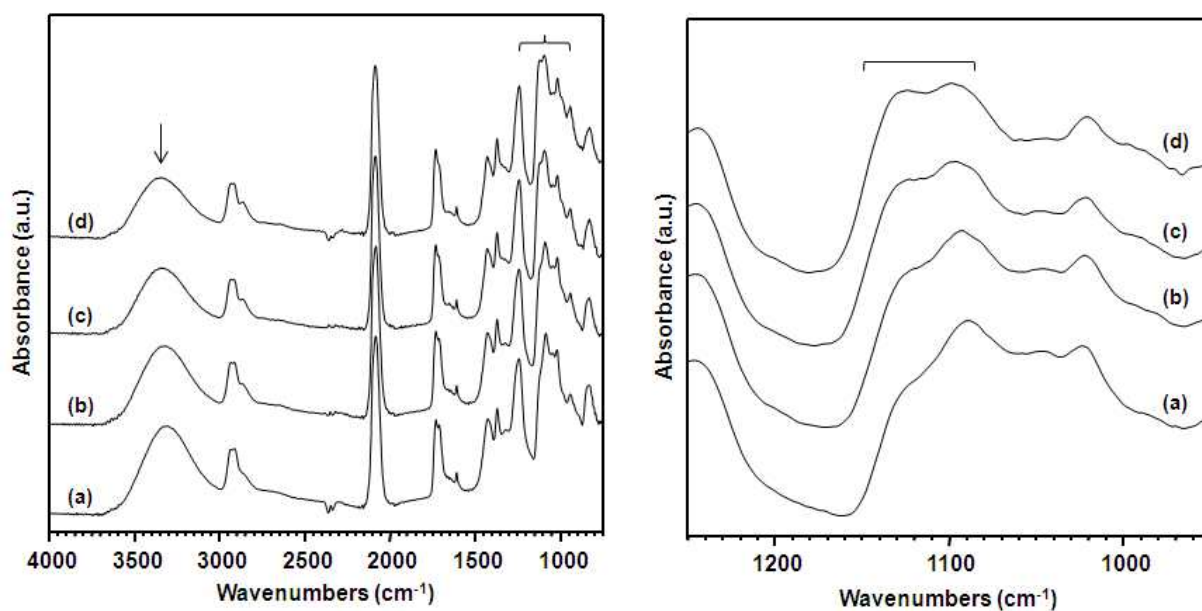
Figure 3.5 FT-IR spectra of *c*-PBNPs/PVA composite nanofibers with different concentrations of GA at the exposure time of 30 s, (a) 2.5 wt%, (b) 7.5 wt%, (c) 12.5 wt% and (d) 17.5 wt%.
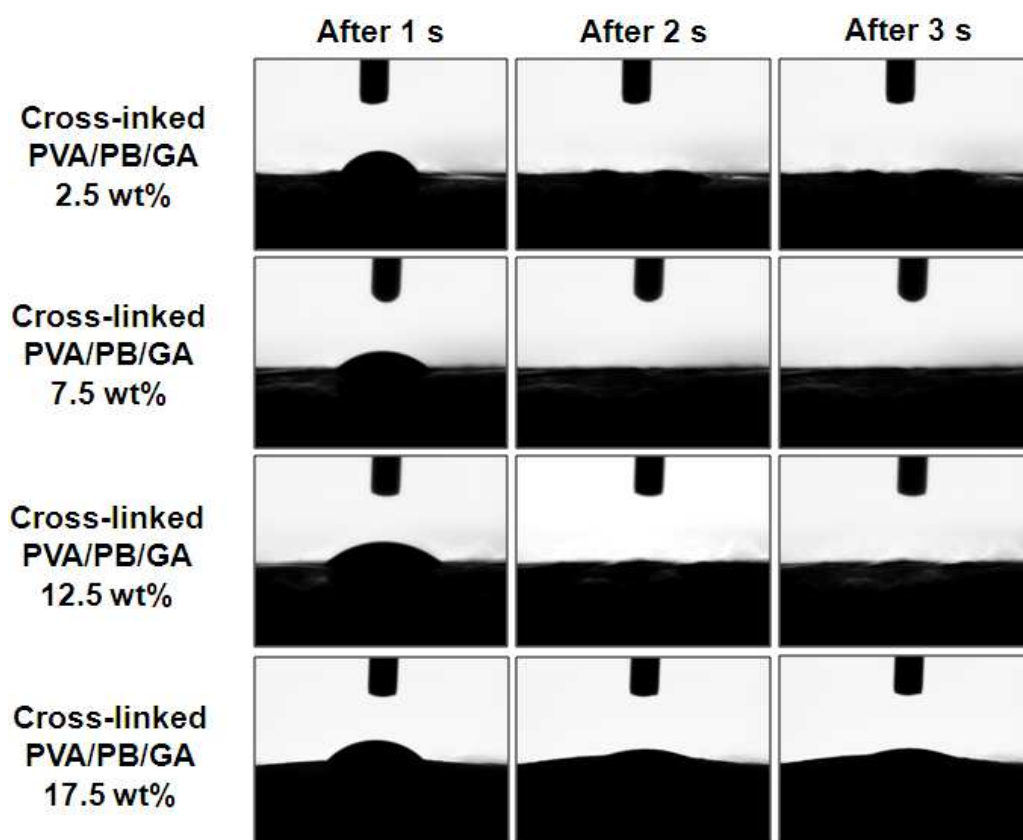
Figure 3.6 Pictures showing the water contact angles of *c*-PBNPs/PVA composite nanofibers with different concentrations of GA at different times.

3.3.2 Characterization of *c*-PBNPs/PVA composite nanofiber

The surface morphology of the *c*-PBNPs/PVA composite nanofiber was investigated by using SEM analysis. Figure 3.7 shows the SEM images, digital photos (inset) and the fiber diameter distribution of pure PVA nanofibers and *c*-PBNPs/PVA composite nanofibers. It can be seen that the morphology of the both pure PVA nanofibers (Figure 3.7a) and *c*-PBNPs/PVA composite nanofibers (Figure 3.7b) were smooth and continuous with diameters of 200-300 nm and lengths up to several millimeters. It is worth to mention that the fibrous shape and diameter of *c*-PBNPs/PVA composite nanofibers maintained well even after the incorporation of PBNPs and cross-linking of GA. In addition, no individual or aggregation of PBNPs was observed in the SEM image of *c*-PBNPs/PVA (Figure 3.7b). The average fiber diameter of PVA nanofibers and *c*-PBNPs/PVA composite nanofibers are 260 ± 20 nm and 250 ± 90 nm, respectively. When compared to the results of pure PVA nanofibers, the fiber diameter slightly decreased (from 260 nm to 250 nm) and the distribution of fiber diameter too quite broaden (from 260 ± 20 nm to 250 ± 90 nm). This is may be due to the higher electrical conductivity of the PBNPs/PVA/GA solution compared to PVA solution. Moreover, the inserted digital photos (Figure 3.1a and 3.1b) show that the PVA nanofibers are white color while *c*-PBNPs/PVA composite nanofibers are inherent blue color; confirms the successful incorporation PBNPs into the PVA matrix.
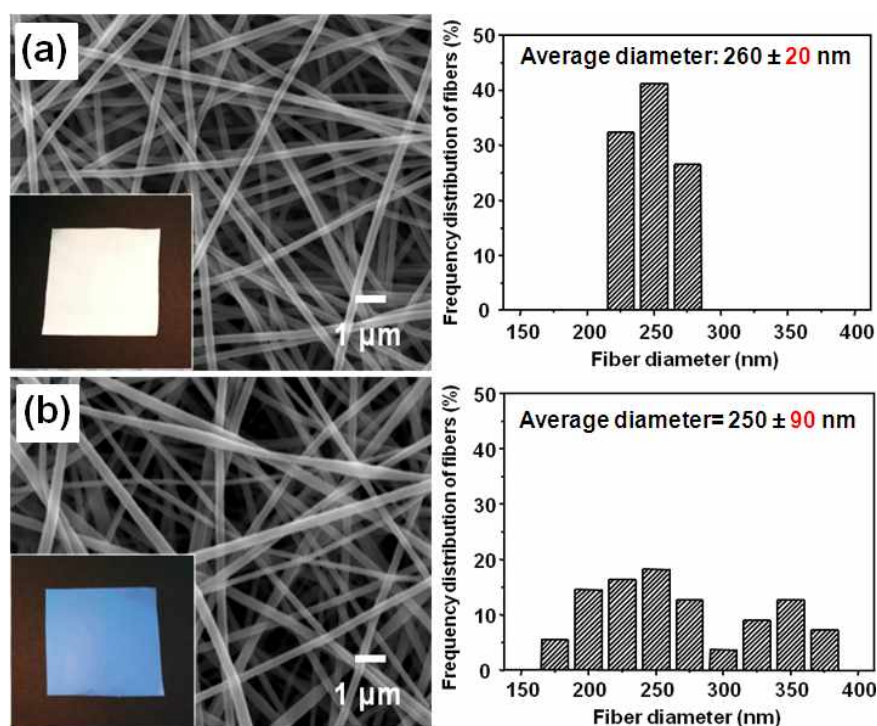
Figure 3.7 – SEM images (left) of (a) pure PVA nanofibers and (b) *c*-PBNPs/PVA composite nanofibers, and the fiber diameter distribution (right) of corresponding electrospun nanofibers.
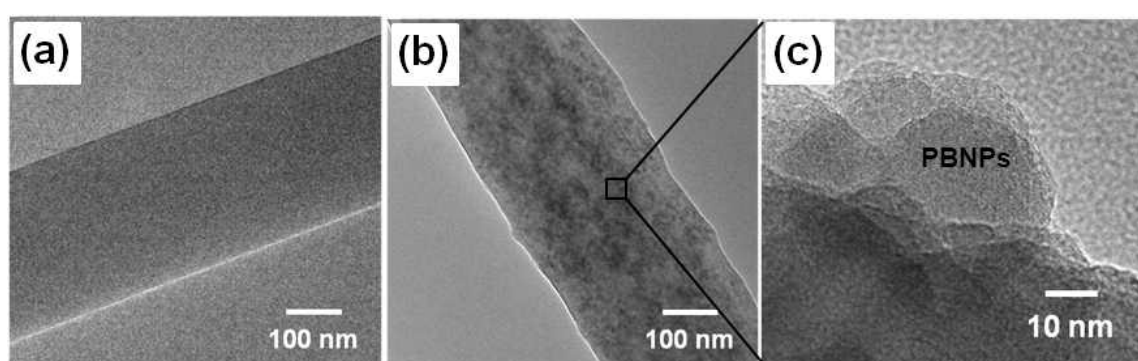
Figure 3.8 – TEM images of (a) pure PVA nanofiber, (b) *c*-PBNPs/PVA composite nanofiber and (c) magnified TEM image of *c*-PBNPs/PVA composite nanofiber.
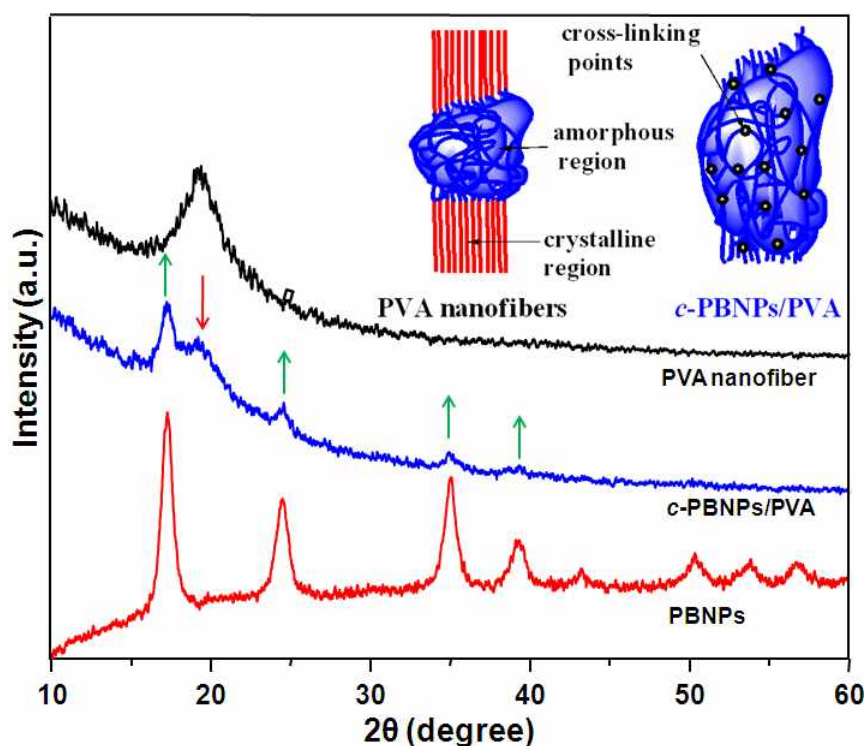
Figure 3.9 – XRD patterns of pure PVA nanofibers, PBNPs and *c*-PBNPs/PVA composite nanofibers (inset: schematic illustration of the crystalline and amorphous regions of PVA and *c*-PBNPs/PVA nanofibers).

The well incorporation and homogeneous dispersion of PBNPs into the PVA matrix were investigated in detail by using TEM analysis. Figure 3.8 shows the TEM images of pure PVA nanofibers (Figure 3.8a) and *c*-PBNPs/PVA composite nanofibers (Figure 3.8b and 3.8c). The results confirmed that the PBNPs are homogeneously distributed into the PVA nanofiber matrix (Figure 3.8b). Most of the PBNPs are embedded within the PVA fiber, and some of the PBNPs remain on the surface of the nanofibers (Figure 3.8c). The size of the incorporated PBNPs in *c*-PBNPs/PVA was

found to be ~15 nm. Moreover, the PVA nanofibers exhibited smooth surface morphology (Figure 3.8b), whereas the *c*-PBNPs/PVA composite nanofibers showed fairly rough surface morphology due to the incorporation of PBNPs.

Figure 3.9 shows the XRD patterns of the pure PVA nanofibers, PBNPs and *c*-PBNPs/PVA composite nanofibers. The PBNPs displays several strong and broad peaks notably at 2θ = 17.4°, 24.7°, 35.3° and 39.5° correspond to typical crystal phases (200), (220), (400) and (420) of cubic face-centered PBNPs lattice (JCPDS card no. 52-1907) [23,24]. For the electrospun PVA nanofibers, a significant crystalline peak at about 23.5° (2θ) was observed, which is due to the strong intermolecular and intermolecular hydrogen bonding [25]. In case of *c*-PBNPs/PVA composite nanofibers, the XRD spectrum is a combination of pure PVA and PBNPs spectra. In detail, in the XRD spectrum of *c*-PBNPs/PVA composite nanofibers, except the diffraction peaks of PVA [23.5° (2θ)], all the other peaks corresponding to the PBNPs phase. The decrease in the peak intensity at 23.5° for *c*-PBNPs/PVA composite nanofibers reveals a lower crystallinity of the *c*-PBNPs/PVA composite when compared to PVA nanofibers. In fact, the suppression of PVA nanofibers crystallinity in the *c*-PBNPs/PVA composite fibers is mainly caused by destruction of the orientation order of the PVA chains and even by the formation of amorphous bound layers around the PBNPs [26]. In the present case, the homogeneously dispersed PBNPs act as steric hindrances within the composite fibers, and thus the crystallization is restricted by a decreasing amount of intact crystalline region. As a result, the usual planar zigzag conformation collapses and converts into an amorphous structure on the interfacial region of PBNPs. Thus, the overall crystallinity of

PVA is decreasing when the PBNPs are incorporated into the PVA matrix. This result is in good agreement with the TEM results (Figure 3.8).
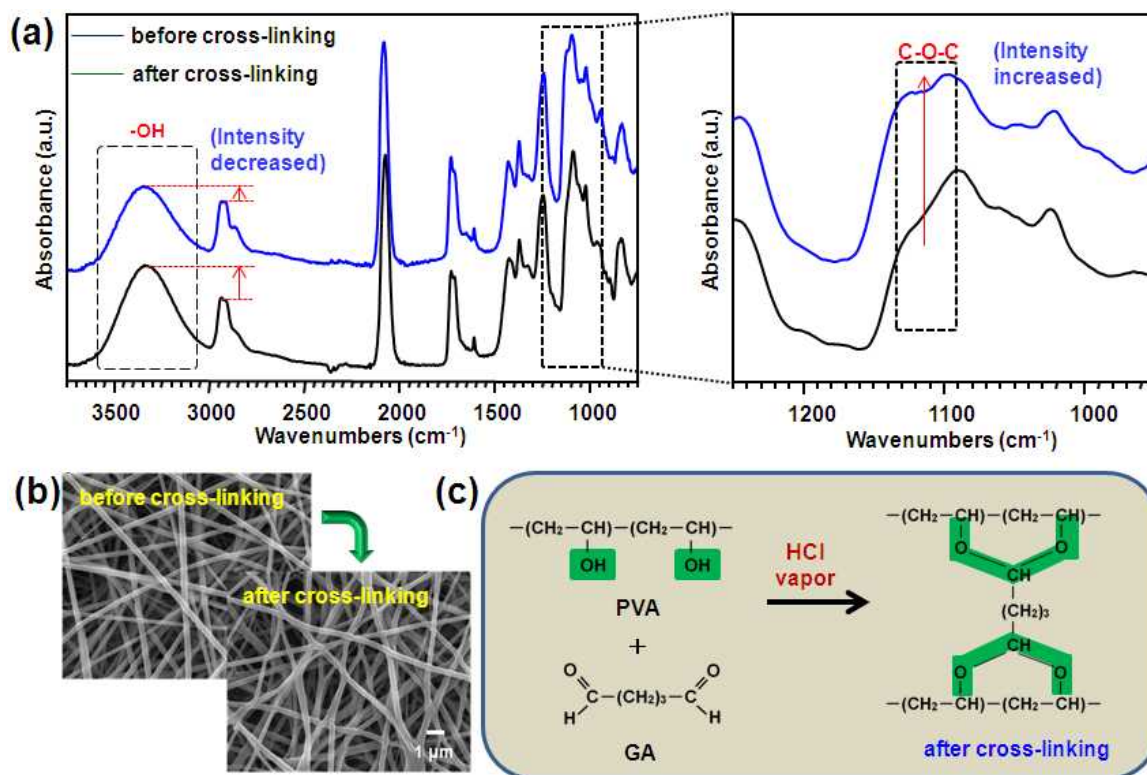
Figure 3.10 – (a) Full (left) and magnified (right) FT-IR spectra of PBNPs/PVA composite nanofibers before (PVA/PBNPs/GA) and after corss-linking (*c*-PBNPs/PVA), (b) SEM images of a) PVA/PBNPs/GA and b) *c*-PBNPs/PVA composite nanofibers (the scale bar is 1 *μ*m), and (c) scheme showing the cross-linking of PVA with GA under HCl vapor.

In order to confirm the cross-linking of PVA with GA, FT-IR spectra were recorded for the PVA/PBNPs/GA(before cross-linking) and *c*-PBNPs/PVA (after cross-linking) composites nanofibers (Figure 3.10). As expected, both the FT-IR spectra exhibited characteristic peaks of PVA and PBNPs. In Figure 3.10a, the characteristic absorption bands of PVA were absorbed at 3278 cm^{-1} (stretching of –OH group), 2935 cm^{-1} (ν_{as} of –CH$_2$), 2906 cm^{-1} (ν_s of –CH$_2$), 1417 cm^{-1} (bending of –OH and wagging of –CH$_2$), 1143 cm^{-1} (stretching of –C–O–C– from crystalline sequence of PVA), 1088 cm^{-1} (stretching of CO and bending of OH from amorphous sequence of PVA), 919 cm^{-1} (bending of –CH$_2$) and 838 cm^{-1} (rocking of –CH)[27]. Similarly, the FT-IR spectrum of the samples exhibited a peak at 2110 cm^{-1} attributed to the –C≡N stretching in the formed [FeII–CN–FeIII] structure, which indicates the presence of PBNPs [28]. Apart from the characteristic absorption band, there are two significant changes in the FT-IR peaks (–OH and –C–O–C–) obviously confirm the cross-linking of PVA with GA [29]. In the FT-IR spectrum of *c*-PBNPs/PVA composites nanofibers, the intensity of the adsorption peak at 3300 cm^{-1} (–OH stretching) decreased and simultaneously the adsorption peak at 1150-1085 cm^{-1} (–C–O–C– stretching) increased when compared with that of the uncross-linked nanocomposite nanofibers (PVA/PBNPs/GA). These results confirm that the –OH groups in the PVA and the –CHO groups in GA typically reacted to form an acetal groups or ether linkages during the cross-linking process (Figure 3.10c) [30].

Several existing PBNPs-based nanocomposites highly suffer from the leaching of PBNPs after the adsorption of Cs from the wastewater and sometimes the nanocomposites are partially soluble in water, which leads to low environmental impact and therefore hinders its direct industrial applications. Hence, the water resistance

property and the stability of *c*-PBNPs/PVA composite nanofibers were investigated in detail. In a typical experiment, 1g of *c*-PBNPs/PVA composite nanofibers was dipped into a 50mL of Milli Q water and shaked for 100 min using a multi shaker with 600 rpm at 27°C. Finally, the mixture was filtered and the leaching of Fe was analyzed by ICP-MS. Figure 3.11 show digital photos of *c*-PBNPs/PVA composites nanofiber soaked in distilled water for 1 h at 27°C. As seen from Figure 3.11, no significant leaching of PBNPs from *c*-PBNPs/PVA composite nanofibers is observed. In addition, after soaking, the soaked water and the composites were further analyzed by ICP-MS analysis. The results confirmed that the *c*-PBNPs/PVA composite nanofibers are highly stable since it showed very less amount of (~1.7ppb) leaching of PBNPs and the unaffected morphology of *c*-PBNPs/PVA composite nanofibers (Table 3.1) [31]. This is may be due to the effective cross-linking process of PVA with GA.
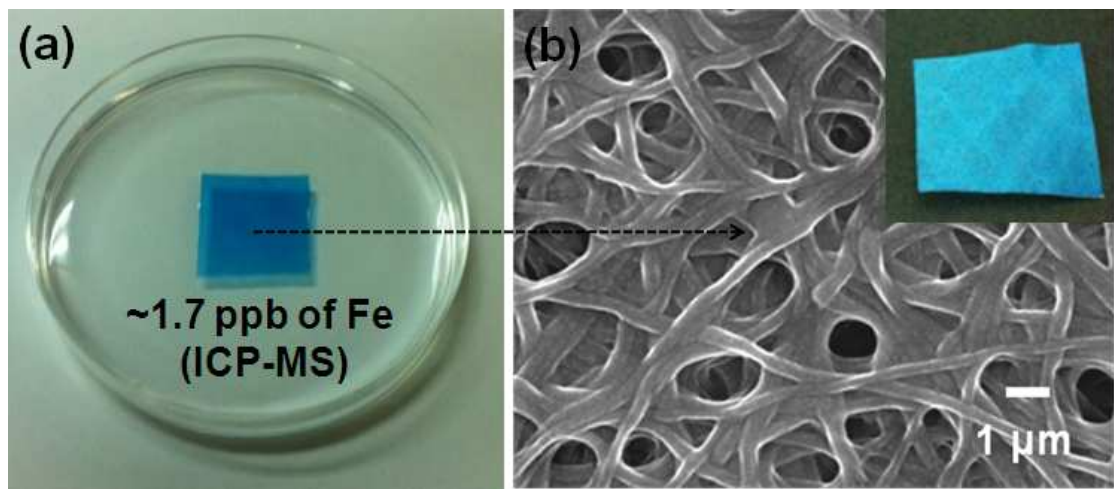
Figure 3.11 – Digital photos of (a) *c*-PBNPs/PVA composite nanofibers soaked in distilled water and (b) SEM image (inset: digital photo) of cross-linked *c*-PBNPs/PVA composite nanofibers after soaking in distilled water for 1 h (dried).

Table 3.1 Fe dissolution test with Cs adsorbents

S.No	Weight of PB of c-PBNPs/PVA composite nanofibers (mg) by ICP-MS	Solution amounts (mL)	Temperature (^{o}C)	Concentration of Fe in solution (ppb)	Conversion concentration of Fe (ppb)
1	1.0059	50	25	15.19	1.519
2	1.0033	50	25	17.21	1.721
3	1.0028	50	25	19.34	1.934
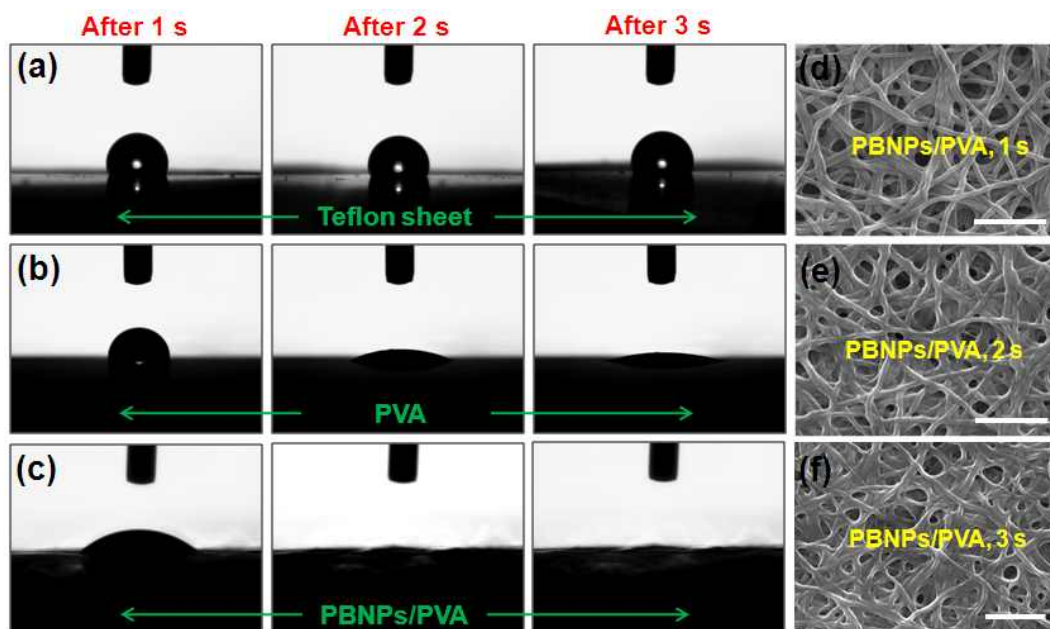
Figure 3.12 – Pictures showing the water contact angles of (a) Teflon sheet (for reference), (b) pure PVA nanofibers with a smooth surface, (c) c-PBNPs/PVA composite nanofibers with a rough surface, and SEM images of c-PBNPs/PVA after the water contact angle test; after (d) 1 s, (e) 2 s and (f) 3 s.

Since the hydrophilic nature of the *c*-PBNPs/PVA composite nanofibers is one of the highly significant properties for the rapid adsorption of the Cs, the wettability of the pure PVA and *c*-PBNPs/PVA-composite nanofibers were investigated by the measurements of water contact angles. In Figure 3.12, the photographs show the water contact angles of Teflon sheet (for reference), pure PVA nanofibers and *c*-PBNPs/PVA composite nanofibers. Although the surface of the *c*-PBNPs/PVA composite nanofibers are rough, it showed lower water contact angle of 29° than that of pure PVA nanofibers (91°), which obviously indicates that the cross-linked *c*-PBNPs/PVA composite have high hydrophilic nature. This is due to the presence of unreacted (uncross-liked) –OH and –CHO groups in the *c*-PBNPs/PVA composite nanofibers [32]. In addition, the high hydrophilic nature of the *c*-PBNPs/PVA composite is may also be due to the amorphous nature of the *c*-PBNPs/PVA composite when compared to the PVA nanofibers. The result agrees well with the SEM and XRD results (Figure 3.7 and Figure 3.9).

3.3.3 Evaluation of C_s adsorption performance

After the extensive characterization, the *c*-PBNPs/PVA composite nanofiber mat was used for the removal of Cs from the wastewater. ICP-MS analysis was used to study the adsorption activity of the *c*-PBNPs/PVA. Initially, the Cs adsorption behavior of the pure PVA nanofiber was investigated and it was found to be very low even after the soaking time of 100 min. Figure 3.13(a) shows the Cs adsorption rate of *c*-PBNPs/PVA composite nanofibers. The adsorption rate of *c*-PBNPs/PVA increased with increasing soaking time, and this value was found to be 86 %, 90 %, and 96 % for the soaking time of 10 min, 30 min, and 100 min, respectively. The merit of the present *c*-PBNPs/PVA

was realized from the very high adsorption rate of 86% after only 10 min. To the best of our knowledge, this is the highest activity (86% after 10 min) reported for the adsorption of Cs from the radioactive wastewater till to date. Moreover, the results are well comparable to those previous reported. In most of the previous studies, the hybrid materials have showed the maximum adsorption rate of about 30-65 % after the soaking time of 10 min[33-39]. For instance, the magnetic hexacyanoferrate (II) polymeric nanocomposite (RZ) showed the adsorption rate of ~65% after 10 min and the maximum adsorption rate of ~95% only after 150 h, [10] whereas the present c-PBNPs/PVA composite nanofibers showed a very higher Cs adsorption rate of ~96% after only a very less soaking time of 100 min (1.7 h). Similarly, the present c-PBNPs/PVA composite nanofibers confirmed a better adsorption rate of ~96 % (100 min) when compared to the zirconium(IV) iodomolybdate exchanger (ZIM) (Figure 3.13) [40]. The results confirm the higher activity of the present c-PBNPs/PVA composite nanofibers towards the adsorption of radioactive Cs from the wastewater. From the value of Cs adsorption rate, it was calculated that 1 g of c-PBNPs/PVA composite is enough to remove ~8 mg of Cs from the wastewater. Although the value is not higher when compared to the previous reports [9, 10, 40-44], the proposed composite material has shown a faster Cs adsorption rate in addition to the other advantages such as easy-handling and separation. There are three possible reasons for the higher activity of this newly developed c-PBNPs/PVA composite nanofibers: (1) higher surface area and the three dimensional structure of the c-PBNPs/PVA composite nanofibers web, (2) higher hydrophilic nature of the composite and (3) water-insoluble property of the c-PBNPs/PVA composite nanofibers. Apart from

these most possible reasons, the higher dispersion of PBNPs into the PVA matrix might also be assisted for the higher adsorption rate of Cs from the wastewater.
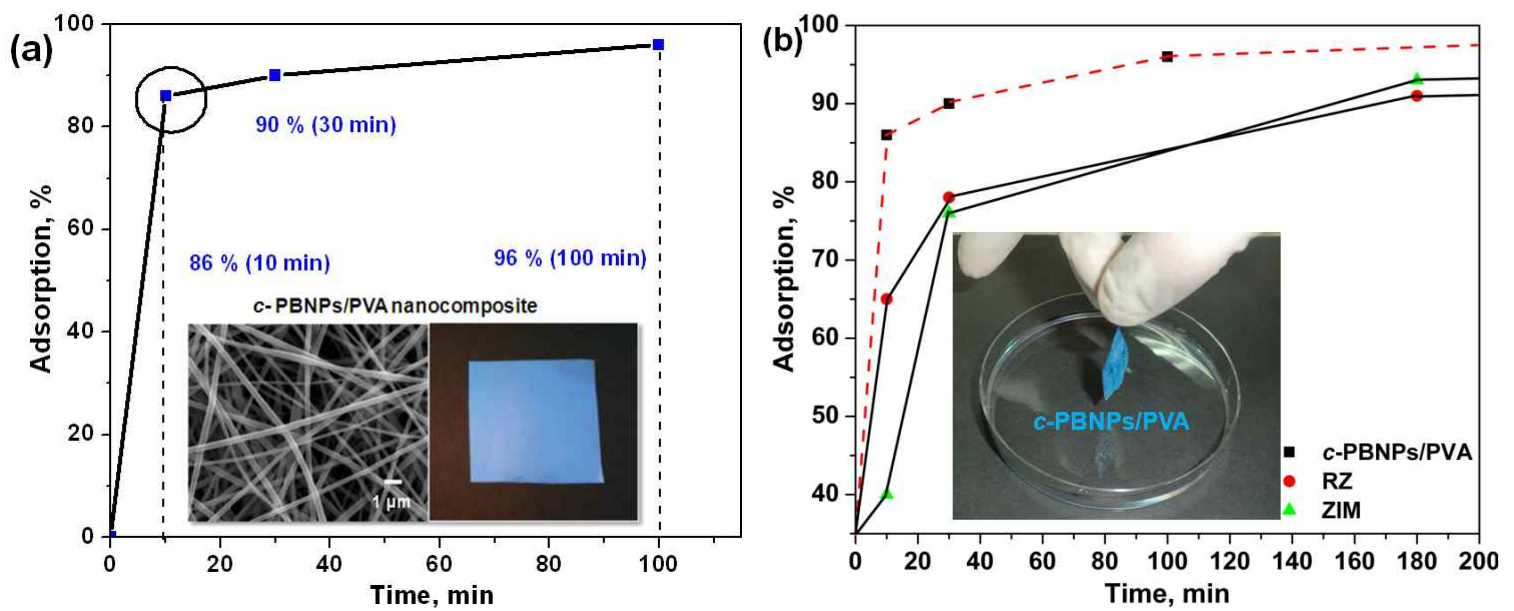
Figure 3.13 – (a) Adsorption of Cs onto *c*-PBNPs/PVA composite nanofiber at different time intervals and (b) comparison of Cs adsorption activity of present composite nanofiber (*c*-PBNPs/PVA) with previously reported nanocmposites (RZ [10] and ZIM [40]) (inset showing the separation of *c*-PBNPs/PVA after treatment).

3.3.4 Separation of *c*-PBNPs/PVA after Cs adsorption test

The separation of Cs adsorbents after treatment is very important since the radioactive Cs is highly harmful [9,13,14]. At present, the challenging task is the development of easily separable Cs adsorbents[45]. There are several reports describe various separation techniques for the removal Cs adsorbents after treatment. However, since the PBNPs-based nanocomposites are very small in size (10-100 nm), the separation process is more complicated and expensive. For instance, Chakrit et al., [9] reported that the PBNPs-coated magnetic NPs for the removal of Cs from wastewater. However, they used a neodymium magnet (strength of 0.25 T) for the separation of PBNPs-coated MNP nano-sorbent from the wastewater after treatment. Similarly, magnetic PBNPs/graphene oxide nanocomposites (PBNPs/GO) for the removal of radioactive Cs were reported by Hongjun and co-workers[14]. In spite of their higher adsorption activity, the separation of PBNPs/GO is very difficult and expensive. Interestingly, in the present study, the separation of Cs adsorbent (*c*-PBNPs/PVA composite nanofiber) is very simple and efficient. After the Cs adsorption test, the *c*-PBNPs/PVA composite nanofiber sheets can be easily taken off from the wastewater by well-gloved hands (inset in Figure 3.13b). The simple and effective separation of *c*-PBNPs/PVA composite nanofiber is also one of the hall marks of this work. Since the handling and separation are very easy, the present *c*-PBNPs/PVA composite may be good to use for the removal of Cs particularly from the seawater and groundwater.

3.4 Conclusions

In summary, we have successfully prepared a new PBNPs-based PVA composite nanofibers (*c*-PBNPs/PVA) via electrospinning. SEM images revealed smooth and continuous nanofiber morphology of the *c*-PBNPs/PVA composite with diameters of 200-300 nm and lengths up to several millimeters. TEM images confirmed homogeneous dispersion and well incorporation of PBNPs into the PVA matrix. The amorphous nature of the *c*-PBNPs/PVA composite nanofibers was confirmed by the XRD analysis. FT-IR spectra showed successful cross-linking of PVA with GA. It was found that the prepared nanocomposite fiber is highly hydrophilic and water-insoluble. The excellent activity of the *c*-PBNPs/PVA composite nanofibers can be realized from the higher Cs adsorption rate of 96 % after only 100 min. Moreover, the mass production of the *c*-PBNPs/PVA is simple and cost-effective. After Cs adsorption test, the *c*-PBNPs/PVA can be easily separated from the wastewater. Overall, the simple preparation, easy separation and faster Cs adsorption activity make *c*-PBNPs/PVA as an alternate choice to the existing PBNPs-composite materials.

References

[1]   Morino, Y.; Ohara, T.; Nishizawa, M. Atmospheric behavior, deposition, and budget of radioactive materials from the Fukushima Daiichi nuclear power plant in March 2011. *J. Geophys. Res.* **2011**, 38, 1–7.

[2]   Kato. H.; Onda, Y.; Teramage, M. Depth distribution of ^{137}Cs, ^{134}Cs, and ^{131}I in soil profile after Fukushima Dai-ichi Nuclear Power Plant Accident. *J. Environ. Radioactiv.* **2012**, 111, 59–64.

[3]   Kawamura, H.; Kobayashi, T.; Furuno, A.; In, T.; Ishikawa, Y.; Nakayama, T.; Shima, S.; Awaji, T. Preliminary Numerical Experiments on Oceanic Dispersion of ^{131}I and ^{137}Cs Discharged into the Ocean because of the Fukushima Daiichi Nuclear Power Plant Disaster. *J. Nucl. Sci. Technol.* **2011**, 48, 1349–1356.

[4]   Chino, M.; Nakayama, H.; Nagai, H.; Terada, H.; Katata, G.; Yamazawa, H. Preliminary Estimation of Release Amounts of ^{131}I and ^{137}Cs Accidentally Discharged from the Fukushima Daiichi Nuclear Power Plant into the Atmosphere. *J. Nucl. Sci. Technol.* **2011**, 48, 1129–1134.

[5]   Sangvanich, T.; Sukwarotwat, V.; Wiacek, R. J.; Grudzien, R. M.; Fryxell, G. E.; Addleman, R. S.; Timchalk, C.; Yantasee, W. Selective capture of Cesium and Thallium from natural waters and simulated wastes with copper ferrocyanide functionalized mesoporous silica. *J. Hazard. Mater.* **2010**, 182, 225–231.

[6]   Torad, N. L.; Hu, M.; Imura, M.; Naito, M.; Yamauchi, Y. Large Cs adsorption capability of nanostructured Prussian Blue particles with high accessible surface areas. *J. Mater. Chem.* **2012**, 22, 18261–18267.

[7] Escosura, A. de la; Martijn, V.; Friso, D. S.; Marta, C. A.; Andrei, K.; Theo, R.; Roeland, J. M. N.; Jeroen, J. L. M. C. Viral capsids as templates for the production of monodisperse Prussian blue nanoparticles. *Chem. Commun.* **2008**, 1542-1544.

[8] Subbiah, T.; Bhat, G. S.; Tock, R. W.; Parameswaran, S.; Ramkumar, S. S. Electrospinning of nanofibers. *J. Appl. Poly. Sci.* **2005**, 96, 557-569.

[9] Chakrit, T.; Pakorn, O.; Pramuan, T.; Paiboon, S. Prussian blue-coated magnetic nanoparticles for removal of cesium from contaminated environment. *J. Nanopart. Res.* **2013**, 15, 1689(1-10).

[10] Reda, R. S. Synthesis and characterization of magnetic hexacyanoferrate (II) polymeric nanocomposite for separation of cesium from radioactive waste solutions. *J. Colloid Interface Sci*. **2012**, 388, 21−30.

[11] Gopiraman, M.; Karvembu, R.; Kim, I. S. Highly Active, Selective and Reusable RuO2/SWCNT Catalyst for Heck Olefination of Aryl Halides. *ACS Catal*. **2014**, 4, 2118−2129.

[12] Gopiraman, M.; Ganesh Babu, S.; Khatri, Z.; Wei, K.; Kim, Y. A.; Endo, M.; Karvembu, R.; Kim, I. S. Dry Synthesis of Easily Tunable Nano Ruthenium Supported on Graphene: Novel Nanocatalysts for Aerial Oxidation of Alcohols and Transfer Hydrogenation of Ketones. *J. Phys. Chem. C.* **2013**, 117, 23582–23596.

[13] Hongjun, Y.; Lei, S.; Jiali, Z.; Haiyan, L.; Yan, Z.; Hongwen, Y. In situ controllable synthesis of magnetic Prussian blue/graphene oxide nanocomposites for removal of radioactive cesium in water. *J. Mater. Chem. A.* **2014**, 2, 326–332.

[14]   Gopiraman, M.; Ganesh Babu, S.; Khatri, Z.; Kai, W.; Kim, Y. A.; Endo, M.; Karvembu, R.; Kim. I. S. An efficient, reusable copper-oxide/carbon-nanotube catalyst for N-arylation of imidazole. *Carbon.* **2013**, 62, 135–148.

[15]   Ohsawa, O.; Lee, K. H.; Kim, B. S.; Lee, S.; Kim, I. S. Preparation and Characterization of Polyketone (PK) Fibrous Membrane via Electrospinning. *Polymer.* **2010**, 51, 2007-2012.

[16]   Park, S. J.; Kim, H. R.; Bang, H. S.; Fujimori, K.; Kim, B. S.; Kim, S. H.; Kim, I. S. Fabrication and Deodorizing Efficiency of Nanostructured Core-Sheath TiO_2 Nanofibers. *J. Appl. Poly. Sci.* **2012**, 125, 2929–2935.

[17]   Dian, H.; Bo, H.; Qiao-Feng, Y.; Kan, W.; Shu-Hong, Y. Large-Scale Synthesis of Flexible Free-Standing SERS Substrates with High Sensitivity: Electrospun PVA Nanofibers Embedded with Controlled Alignment of Silver Nanoparticles. *ACS Nano.* **2009**, 3, 3993–4002.

[18]   Jie, B.; Yaoxian, L.; Songtao, Y.; Jianshi, D.; Shugang, W.; Jifu, Z.; Yongzhi, W.; Qingbiao, Y.; Xuesi, C.; Xiabin, J. A simple and effective route for the preparation of poly(vinylalcohol)(PVA) nanofibers containing gold nanoparticles by electrospinning method. *Solid State Comm.* **2007**, 141, 292–295.

[19]   Mbhele, Z. H.; Salemane, M. G.; Sittert, C. G. C. E. van; Nedeljkovic, J. M.; Djokovic, V.; Luyt, A. S. Fabrication and Characterization of Silver−Polyvinyl Alcohol Nanocomposites. *Chem. Mater.* **2003**, 15, 5019–5024.

[20]   Park, J. C.; Ito, T.; Kim, K. O.; Kim, K. W.; Kim, B. S.; Khil, M. S.; Kim, H. Y.; Kim, I. S. Electrospun poly(vinyl alcohol) nanofibers: effects of degree of hydrolysis and enhanced water stability. *Polymer Journal.* **2010**, 42, 273–276.

[21] Kong, H.; Jang J. One-step fabrication of silver nanoparticle embedded polymer nanofibers by radical-mediated dispersion polymerization. *Chem. Commun.* **2006**, 3010-3012.

[22] Chuan-Ling, Z.; Kong-Peng, L.; Huai-Ping, C.; Shu-Hong, Y. Controlled Assemblies of Gold Nanorods in PVA Nanofiber Matrix as Flexible Free-Standing SERS Substrates by Electrospinning. *Small.* **2012**, 8, 648–653.

[23] Kim, K. O.; Akada, Y.; Wei, K.; Kim, B. S.; Kim, I. S. Cells Attachment Property of PVA Hydrogel Nanofibers Incorporating Hyaluronic Acid for Tissue Engineering. *J. Biomater. Nanobiotechn.* **2011**, 2, 353–360.

[24] Chakrit, T.; Pakorn, O.; Pramuan, T.; Paiboon, S. Prussian blue-coated magnetic nanoparticles for removal of cesium from contaminated environment. *J. Nanopart. Res.* **2013**, 15, 1689(1-10).

[25] Park, J. H.; Karim, M. R.; Kim, I. K.; Cheong, I. W.; Kim, J. W.; Bae, D. G.; Cho, J. W.; Yeum, J. H. Electrospinning fabrication and characterization of poly(vinyl alcohol)/montmorillonite/silver hybrid nanofibers for antibacterial applications. *Colloid Polym. Sci.* **2010**, 288, 115–121.

[26] Ki, C. S.; Baek D. H.; Gang K. D.; Lee, K. H.; Um, I. C.; Park, Y. H. Characterization of gelatin nanofiber prepared from gelatin–formic acid solution. *Polymer.* **2005**, 46, 5094–5102.

[27] Mansur, H. S.; Sadahira, C. M.; Souza, A. N.; Mansur, A. A. FTIR spectroscopy characterization of poly (vinyl alcohol) hydrogel with different hydrolysis degree and chemically crosslinked with glutaraldehyde. *Mater. Sci. Eng. C.* **2008**, 28, 539–548.

[28]   Pawel, J. K.; Marcin, A. M.; Andrzej, D.; Jerzy, S. In Situ FT-IR/ATR Spectroelectrochemistry of Prussian Blue in the Solid State. *Anal. Chem*. **1996**, 68, 2442–2446.

[29]   Herman, S. M.; Rodrigo, L. O.; Alexandra, A. P. M. Characterization of poly(vinyl alcohol)/poly(ethylene glycol) hydrogels and PVA-derived hybrids by small-angle X-ray scattering and FTIR spectroscopy. *Polymer*. **2004**, 45, 7193–7202.

[30]   Tang, C.; Saquing, C. D.; Harding, J. R.; Khan, S. A. In Situ Cross-Linking of Electrospun Poly(vinyl alcohol) Nanofibers. *Macromolecules*. **2010**, 43, 630-637.

[31]   Gopiraman, M.; Bang, H. S.; Ganesh Babu, S.; Wei, K.; Karvembu, R.; Kim, I. S. Catalytic N-oxidation of tertiary amines on RuO_2NPs anchored graphene nanoplatelets. *Catal. Sci. Technol*. **2014**, 4, 2099−2106.

[32]   Fujimori, K.; Gopiraman, M.; Kim, H. K.; Kim, B. S.; Kim, I. S. Mechanical and Electromagnetic Interference Shielding Properties of Poly(vinyl alcohol)/Graphene and Poly(vinyl alcohol)/Multi-Walled Carbon Nanotube Composite Nanofiber Mats and the Effect of Cu Top-Layer Coating. *J. Nanosci. Nanotechno*. **2013**, 13, 1759−1764.

[33]   Zhang, Z. Q.; Gong, S. W.; Yu, Z.; Ting, Y.; Wang, C. Y.; Gu, N. Prussian blue modified iron oxide magnetic nanoparticles and their high peroxidase-like activity. *J. Mater. Chem*. **2010**, 20, 5110–5116.

[34]   Liu, X.; Chen, G. R.; Lee, D. J.; Kawamoto, T.; Tanaka, H.; Chen, M. L.; Luo, Y. K. Adsorption removal of cesium from drinking waters: A mini review on use of biosorbents and other adsorbents. *Bioresour. Technol*. **2014**, 160, 142-149.

[35] Durga, P.; Hisashi, T.; Yukiya, H.; Kimitaka, M.; Shigeharu, F.; Kuniyoshi, U.; Ryuichi, K.; Yukie, H.; Masatoshi, O.; Tohru, K. Dealing with the Aftermath of Fukushima Daiichi Nuclear Accident: Decontamination of Radioactive Cesium Enriched Ash. *Environ. Sci. Technol.* **2013**, 47, 3800-3806.

[36] Ishizaki, M.; Akiba, S.; Ohtani, A.; Hoshi, Y.; Ono, K.; Matsuba, M.; Togashi, T.; Kananizuka, K.; Sakamoto, M.; Takahashi, A.; Kawamoto, T.; Tanaka, H.; Watanabe, M.; Arisaka, M.; Nankawa, T.; Kurihara, M. Proton-exchange mechanism of specific Cs^+ adsorption via lattice defect sites of Prussian blue filled with coordination and crystallization water molecules. *Dalton Trans.* **2013**, 42, 16049-16055.

[37] Baiyang, H.; Bunshi, F.; Hongwen, Y.; Yoshiteru, A. Prussian blue caged in spongiform adsorbents using diatomite and carbon nanotubes for elimination of cesium. *J. Hazard. Mater.* **2012**, 217-218, 85-91.

[38] Kouji, H. H.; Yukiko, F.; Ayumu, A.; Ayako, T.; Fumikazu, A.; Akio, K. Dietary Intake of Radiocesium in Adult Residents in Fukushima Prefecture and Neighboring Regions after the Fukushima Nuclear Power Plant Accident: 24‑h Food-Duplicate Survey in December 2011. *Environ. Sci. Technol.* **2013**, 47, 2520-2526.

[39] Damir, I.; Andreja, G.; Miran, C.; Boris, P. Prussian Blue-Modified Titanate Nanotubes: A Novel : Nanostructured Catalyst for Electrochemical Reduction of Hydrogen Peroxide. *Electroanalysis.* **2010**, 22, 2202–2210.

[40] Sheha, R. R.; El-Khouly, S. H. Adsorption and diffusion of cesium ions in zirconium(IV) iodomolybdate exchanger. *Chem. Eng. J.* **2013**, 91, 942–954.

[41] Nilchi, A.; Saberi, R.; Moradi, M.; Azizpour, H.; Zarghami, R. Adsorption of cesium on copper hexacyanoferrate–PAN composite ion exchanger from aqueous solution. *Chem. Eng. J.* **2011**, 172, 572–580.

[42] Borai, E.H.; Harjula, R.; Malinen, L.; Paajanen, A. Efficient removal of cesium from low-level radioactive liquid waste using natural and impregnated zeolite minerals. *J. Hazard. Mater.* **2009**, 172, 416–422.

[43] Abusafa, A.; Yucel, H. Removal of ^{137}Cs from aqueous solutions using different cationic forms of a natural zeolite : clinoptilolite. *Sep. Purif. Technol.* **2002**, 28, 103–116.

[44] Yıldız, B.; Erten, H.N.; Kis, M. The sorption behavior of Cs^+ ion on clay minerals and zeolite in radioactive waste management:sorption kinetics and thermodynamics. *J. Radioanal. Nucl. Chem.* **2011**, 288, 475–483.

[45] Sheha, R. R.; El-Khouly, S. H. Exchange Character of Caesium Ions onto Zirconium Tungstate. *Adsorpt. Sci. Technol.* **2011**, 29, 139–155.

CHAPTER 4

Noble Metal / Functionalized Cellulose Nanofiber Composites

for Catalytic Applications

CHAPTER 4

Noble Metal / Functionalized Cellulose Nanofiber Composites

for Catalytic Applications

4.1 Introduction

Metal nanoparticles (MNPs) have played a tremendous role as heterogeneous catalysts in various organic reactions[1,2]. Particularly, supported MNPs catalysts are preferred over the unsupported MNPs due to their simple separation and reusability[3,4]. Till date, several supported MNPs catalysts are reported for various organic reactions. Ho and co-workers[5] prepared RuNPs supported on hydroxyapatite (RuNPs/HAP) by a simple reduction method. They found that the RuNPs/HAP is an efficient catalyst for the *cis*-dihydroxylation and oxidative cleavage of alkenes. Recently, Carrillo *et al.*,[6] have reported a mild synthesis of mesoporous silica supported RuNPs as catalyst for oxidative Wittig coupling reaction. Similarly, various carbon nanomaterials such as carbon nanotubes (CNTs) and graphene have also been widely used as supports for the active MNPs[7,8]. Generally, the catalytic activity of the supported-MNPs depend on three main factors: (i) physicochemical nature of the support, (ii) metal-support interaction, and (iii) particle size distribution[9]. In order to obtain these properties, mainly surface modification is required to create active functional groups on the support materials. In fact, the functional groups can easily assist the formation of fine NPs with good dispersion and adhesion[10]. Since most of the common supports are inert nano-powders, the surface modification, recovery and handling are quite difficult and expensive.

Moreover, in the powder form, the catalysts are easily inhalable which can cause health problems[11]. Hence, developing efficient, green and easily handleable heterogeneous nanocatalysts is an important task.

Electrospun nanofibers (NFs) including cellulose nanofibers (CNFs) have attracted much attention due to their unique properties such as large surface area to volume ratio, biocompatibility, simple surface functionalization, easy handling and outstanding mechanical properties[12–15]. The CNFs and their composites have been used for various potential applications such as sensors, energy, catalysis, biomedical, separators and filters[16–19]. In fact, the surface modification of CNFs is simple and unique[20,21]. In addition, the chemically tunable carboxylate groups present in the cellulose can act as strong anchoring sites to immobilize metal species[22]. The isolation of cellulose fibrils in various aqueous and organic solvents is considerably difficult due to the existence of multiple hydrogen bonds in cellulose[23]. This is also one of the main reasons to prefer the CNFs as support to prepare MNPs-based heterogeneous catalysts[24,25]. Son and co-workers[26] prepared AgNPs/CNFs composite and used as an antimicrobial agent. Zhang et al.,[27] reported a facile fabrication of AuNPs immobilized bacteria CNFs (AuNPs/BCNFs) via a one-step method. They found that the AuNPs/BCNFs is highly efficient for the detection of H_2O_2. Very recently, Zhou et al.,[28] prepared PdNPs supported on bacteria CNFs (PdNPs/BCNFs) by a wet synthesis method and used for the Heck coupling reaction. We presumed that the decoration of noble metals such as Ru and Ag on functional CNFs could show interesting catalytic property. Hence, we have prepared noble MNPs supported on CNFs (RuNPs/CNFs and AgNPs/CNFs) by a simple reduction method. After complete characterization, the

RuNPs/CNFs and AgNPs/CNFs were used as nanocatalysts for the oxidation of benzyl alcohol and *aza*-Michael reaction respectively.

4.2 Experimental section

4.2.1 Materials and characterization

Cellulose acetate (CA, 39.8% acetyl content, Mw = 30 kDa), *N,N*-dimethylformamide (DMF) and acetone were purchased from Sigma Aldrich. $AgNO_3$, $RuCl_3$, NaOH, $NaBH_4$, and $ClCH_2COONa$ were obtained from Wako Pure Chemicals, Japan. All other chemicals were purchased from Sigma-Aldrich or Wako Pure Chemicals and used as received.

A high-voltage power supply (Har-100*12, Matsusada Co., Tokyo), capable of generating voltages up to 100 kV, was used as the source of the electric field to produce the nanofibers. The surface morphology of NFs was investigated by transmission electron microscope (TEM, JEM-2100 JEOL Japan) with accelerating voltage of 120 kV. The weight percentage of the MNPs in nanocomposites was confirmed by scanning electron microscope-energy dispersive spectrum (SEM-EDS, Hitachi, model-3000H). The same field of view was then scanned using an EDS spectrometer to acquire a set of X-ray maps for Ru, Ag, C, and O using 1 ms point acquisition for approximately one million counts. X-ray diffraction (XRD) experiment was performed at room temperature using a Rotaflex RTP300 (Rigaku.Co., Japan) instrument at 50 kV and 200 mA. Nickel-filtered Cu Kα radiation was used for the measurements, along with an angular range of $10 < 2\theta < 50°$. The chemical functionalization of CANFs was analyzed by Fourier transform infrared

spectroscopy (FT-IR, IR Prestige-21, Shimadzu, Japan). To confirm the chemical state of MNPs, X-ray photoemission spectra (XPS) were recorded in Kratos Axis-Ultra DLD model instrument. Prior to the analysis, the samples were irradiated under Mg Kα ray source. Progress of the catalytic reactions was monitored by gas chromatograph (GC, Shimadzu-2010 gas chromatograph). The GC was equipped with 5 % diphenyl and 95% dimethyl siloxane, Restek capillary column (0.32 mm dia, 60 m length) and a flame ionization detector (FID). Helium gas was used as a carrier gas. The initial column temperature was increased from 60 to 150°C at the rate of 10°C/min and then to 220°C at the rate of 40°C/min. To further confirm the catalytic products, nuclear magnetic resonance (NMR) spectra were recorded on a 400 MHz Bruker spectrometer. Tetramethylsilane (TMS) and dimethyl sulphoxide (DMSO-d_6) were used as standard and solvent respectively.

4.2.2 Preparation of cellulose acetate nanofibers (CANFs)

The CANFs were prepared according to our previously reported procedure[29]. In a typical experiment, CA solution (18 wt%) was prepared by dissolving a 3.6 g of CA in 10 mL of acetone/DMF mixture (3:2 ratio). The resultant CA solution was electrospun under an electric field of 12 kV at a tip-to-collector distance of 15 cm. A metallic Cu wire was used as an anode and a cathode was attached to a rotating metallic collector (RMC). The RMC was wrapped with aluminum foil and used as a collector for the nanofibers. For more information, refer the schematic illustration of the electrospinning setup shown in Figure 4.1.
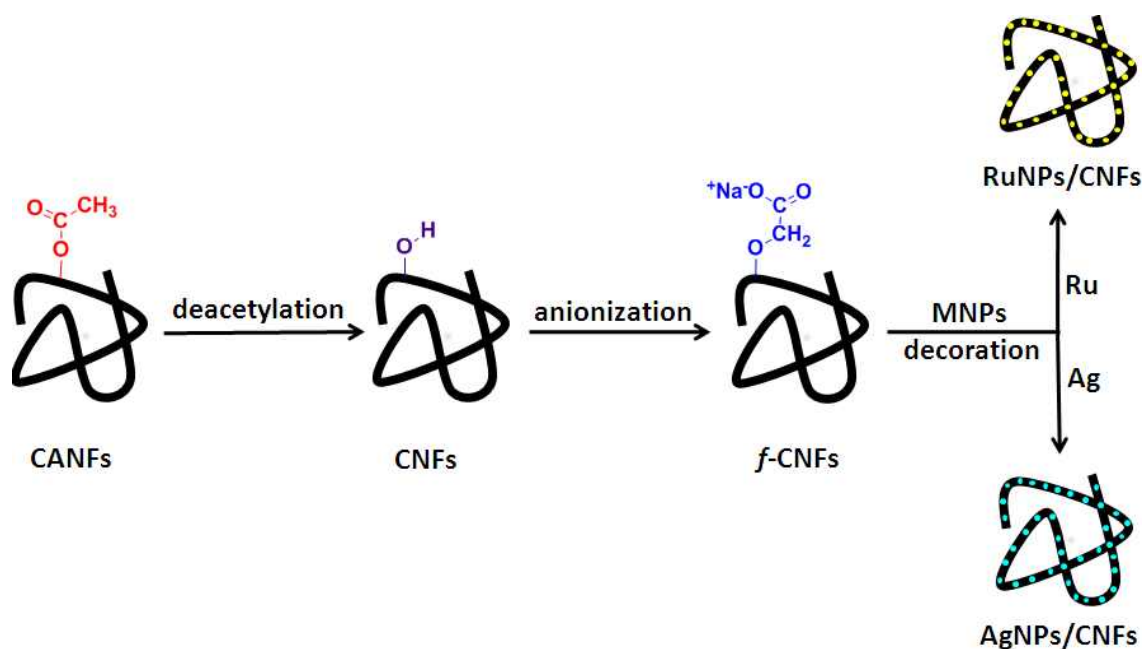
Figure 4.1 – Schematic illustration for the preparation of RuNPs/CNFs and AgNPs/CNFs.

4.2.3 Functionalization of cellulose acetate nanofibers (*f*-CNFs)

Prior to functionalization, the CANFs were deacetylated to regenerate the cellulose nanofibers (CNFs). Briefly, a 100 mg of the CANFs were dipped into 100 mL of NaOH solution (0.05 M) for 48 h at 25°C. Subsequently, the NFs were thoroughly washed with distilled water to remove excess NaOH and dried in oven at 60°C for 4 h. The resultant deacetylated sample (CNFs) was used for the further process.

In the first step of functionalization, the CNFs were dipped into a 1.5 M NaOH solution for 5 min to produce soda cellulose (Na-CNFs) and washed subsequently with 0.05 M NaOH solution. Then the resultant Na-CNFs was dipped into a 1.0 M

ClCH₂COONa solution for 6 h. Finally, the obtained anionic cellulose nanofiber (f-CNFs) was washed thoroughly with distilled water and dried in air. All the steps were carried out at 25°C.

4.2.4 Preparation of nanocomposites (RuNPs/CNFs and AgNPs/CNFs)

As shown in Figure 4.1, both the nanocomposites (RuNPs/CNFs and AgNPs/CNFs) were prepared by a simple wet reduction method using $NaBH_4$ as a reducing agent. For the preparation of RuNPs/CNFs, 100 mg of *f*-CNF was dipped into a 100 mL of aqueous $RuCl_3$ solution (0.5 mmol) at 60°C for 24 h to obtain $RuCl_3$/CNFs, followed by gentle washing with distilled water to remove the excess $RuCl_3$. Subsequently, the $RuCl_3$/CNFs mat was treated with $NaBH_4$ (1 mM, 20 mL) at 25°C for 15 min. Similarly, the AgNPs/CNFs was prepared by using $AgNO_3$ as precursor (100 mL, 0.5 mmol). Finally, the obtained RuNPs/CNFs and AgNPs/CNFs nanocomposites were rinsed twice with distilled water, followed by vacuum drying at room temperature for 24h.

4.2.5 Aerobic oxidation of benzyl alcohol

A 50 mg of RuNPs/CNFs (6.5 mol%) was stirred with 5 mL of toluene taken in a round-bottomed flask equipped with a condenser and a stirring bar. The benzyl alcohol (1 mmol) was added to the stirring solution and then the mixture was refluxed under atmospheric pressure of air at 110°C for 24 h. The progress of the reactions was monitored by TLC and GC analyses. After the reaction, the product was isolated and confirmed by NMR analysis. Benzaldehyde: ^{1}H NMR (400 MHz, DMSO-d₆): δ 7.65 (m,

5H), 9.99 (s, 1H) ppm; ^{13}C NMR (100 MHz, DMSO-d$_6$): δ 130.1, 134.9, 137.3, 192.3 ppm.

4.2.5 *aza*-Michael reaction

A mixture of 1-phenylpiperazine (1 mmol) and acrylonitrile (1 mmol) was stirred in methanol (5 mL) in the presence of AgNPs/CNFs (10 mg, 2.0 mol%) under atmospheric pressure of air at 25°C for 20 min. The completion of the reaction was checked by TLC and GC analyses. Once the reaction completed, the catalyst was separated out from the reaction mixture by simple filtration and the products and unconverted reactants were analyzed by GC without any purification. After the reaction, the product was isolated and confirmed by NMR analysis. 3-(4-phenylpiperazin-1-yl) propanenitrile: ^{1}H NMR (400 MHz, DMSO-d$_6$): δ 2.55 (t, 2H), 2.67 (t, 2H), 3.43 (s, 8H), 6.80 (t, 1H), 6.95 (d, 2H), 7.24 (t, 2H) ppm; ^{13}C NMR (100 MHz, DMSO-d$_6$): δ 16.5, 48.5, 52.4, 53.7, 114.8, 119.8, 120.3, 129.6, 152.8 ppm.

4.3 Results and discussion

4.3.1 Characterization of functionalized cellulose nanofibers (*f*-CNFs)

Figure 4.2 (a-f) shows the SEM images and the histogram of nanofiber diameter distribution for CANFs, CNFs and *f*-CNFs. It can be seen that the surface morphology of CANFs [Figure 4.2(a)] was smooth and continuous with fiber diameters ranging from 50 to 600 nm and lengths up to several millimeters. The mean diameter of the CANFs [Figure 4.2(d)] was calculated to be 325±2.0 nm. Alike, the surface morphology of the CNFs [Figure 4.2(b)] was fine and continuous but the mean fiber diameter of the CNFs was dramatically decreased from 325 to 275±2.0 nm. This phenomenon might be caused by the elimination of acetyl group from the CANFs[30]. Interestingly, after the functionalization process, the surface morphology of the nanofibers (*f*-CNFs) was rough without any significant changes in the diameter and length of the NFs. This may be due to two main factors; (1) replacement of the acetyl group (CH_3COO^-) with carboxyl methyl group ($-CH_2-COOH$) and (2) the presence of Na^+ ions. This rough morphology and the presence of functional groups provide efficient cavities and anchoring sites respectively for the MNPs[31]. Moreover, the anionic functional groups can form a coordination type of bonding with metal ions, which facilitate much better adhesion and homogeneous dispersion of the MNPs on the surface of the CNFs.
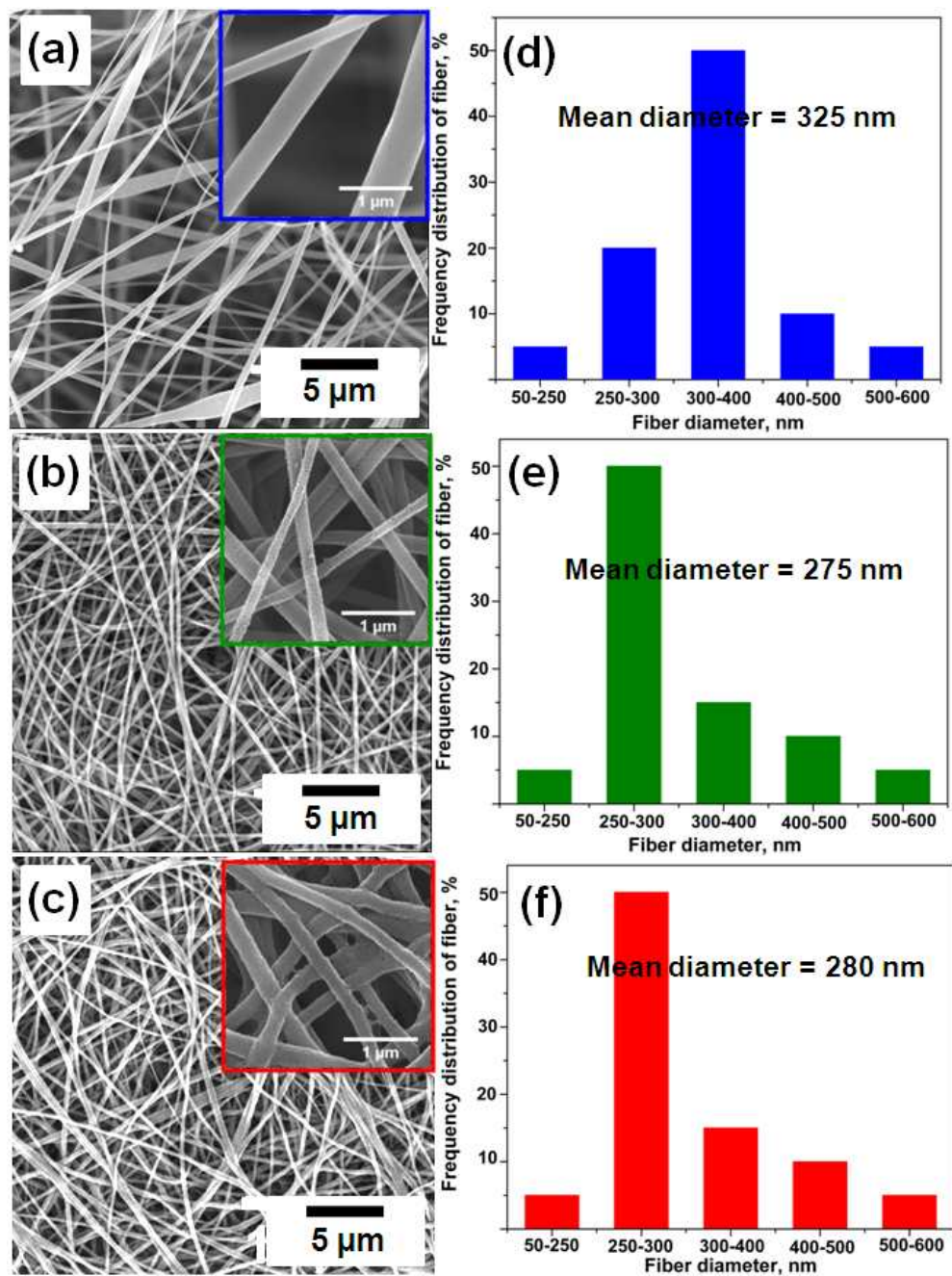
Figure 4.2 – SEM images of (a) CANFs, (b) CNFs and (c) *f*-CNFs, and the histogram of nanofiber diameter distribution for (d) CANFs, (e) CNFs and (f) *f*-CNFs.
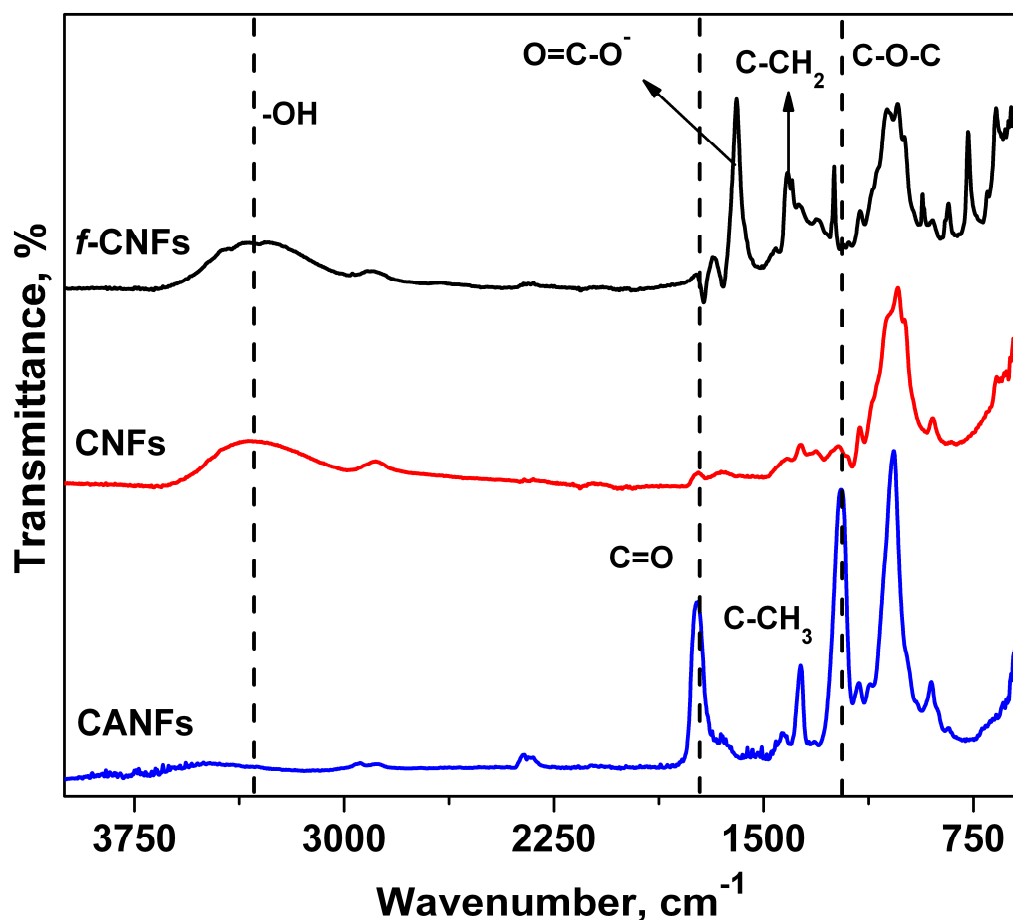
Figure 4.3 – FT-IR spectra of CANFs, CNFs and *f*-CNFs.

FT-IR spectra were recorded for CANFs, CNFs and *f*-CNFs to confirm the chemical modification of the CANFs; the results are shown in Figure 4.3. As expected, for pure CANFs, three intense peaks at 1730, 1373 and 1223 cm^{-1} were observed corresponding to the stretching vibration of C=O, C−CH$_3$ and C–O–C groups, respectively. However, after the deacetylation process, the strong carbonyl absorption at

1730 cm^{-1} was completely disappeared. On the other hand, a much broader and stronger hydroxyl (–OH) peak at 3400 cm^{-1} was observed; the results confirmed the successful regeneration of CNFs from CANFs[32]. In the case of functionalized nanofibers (f-CNFs), FT-IR spectrum showed two new peaks at 1572 cm^{-1} (–COO$^-$) and 1611 cm^{-1} (C–CH2) which indicate the presence of Na-carboxymethyl group (–CH$_2$–COONa)[33]. To further investigate the chemical modification of the CANFs in detail, XPS spectra were also taken for CANFs, CNFs and f-CNFs (Figure 4.4). All the three samples demonstrate a C 1s and O 1s peaks at 283.1 and 530.5 eV respectively. Referring Figure 4.4(a), the binding energy (BE) of the C–C and C–H was assigned at 283.5–284 eV and the peaks at 284.7, 285.6 and 287.5 eV are attributed to C–OH and C=O and C–O–C groups respectively[34]. Similarly, in the case of O 1s spectra, the peaks at 530.5 and 531.2 eV are assigned to C=O and C–OH respectively. When compared to the C 1s XPS spectrum of CANFs [Figure 4.4(a)], a dramatic increase in the peak intensity at 284.7 eV and 531.2 eV (C–OH) was observed for the CNFs. However, for the f-CNFs, these peak intensities (C–OH) decreased along with the appearance of border peaks at 285.6 and 287.5 eV. In addition, a new peak at 1069.1 eV was observed which corresponds to the photoemission from Na$^+$ (Figure 4.5)[35]. The results clearly confirmed the successful functionalization of CNFs.
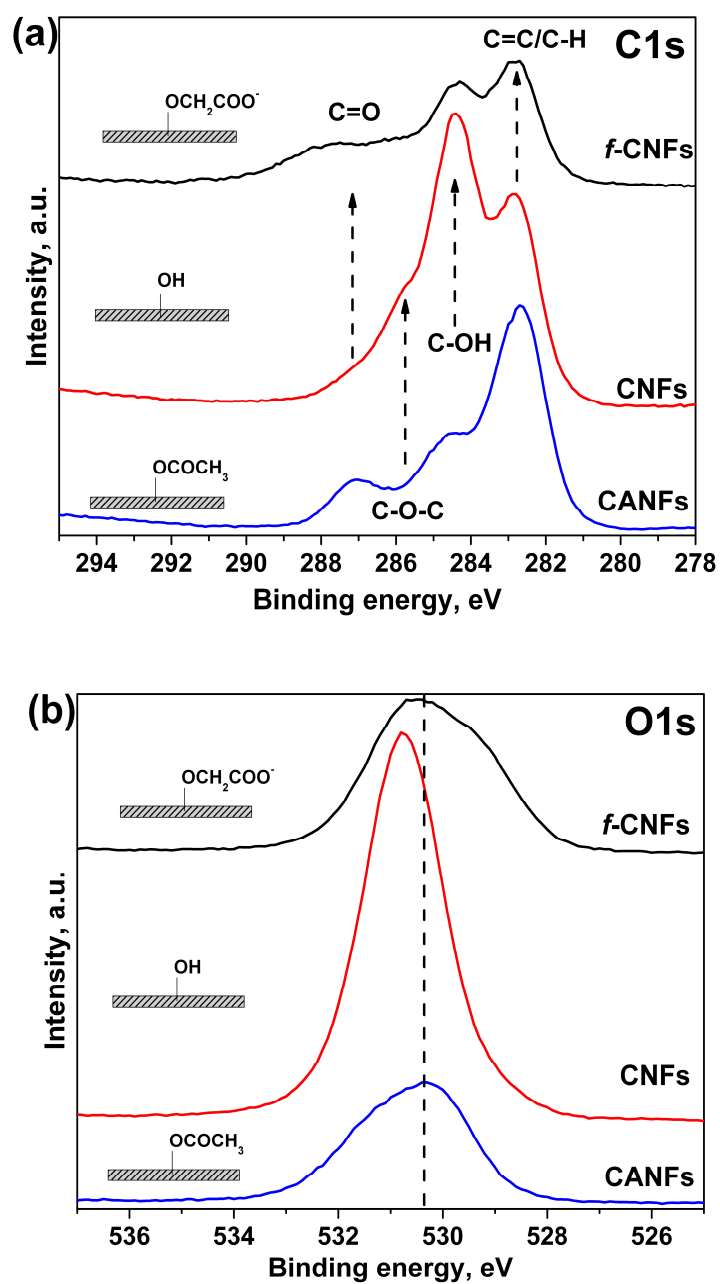
Figure 4.4 – (a) C 1s and (b) O 1s XPS spectra of CANFs, CNFs and *f*-CNFs.
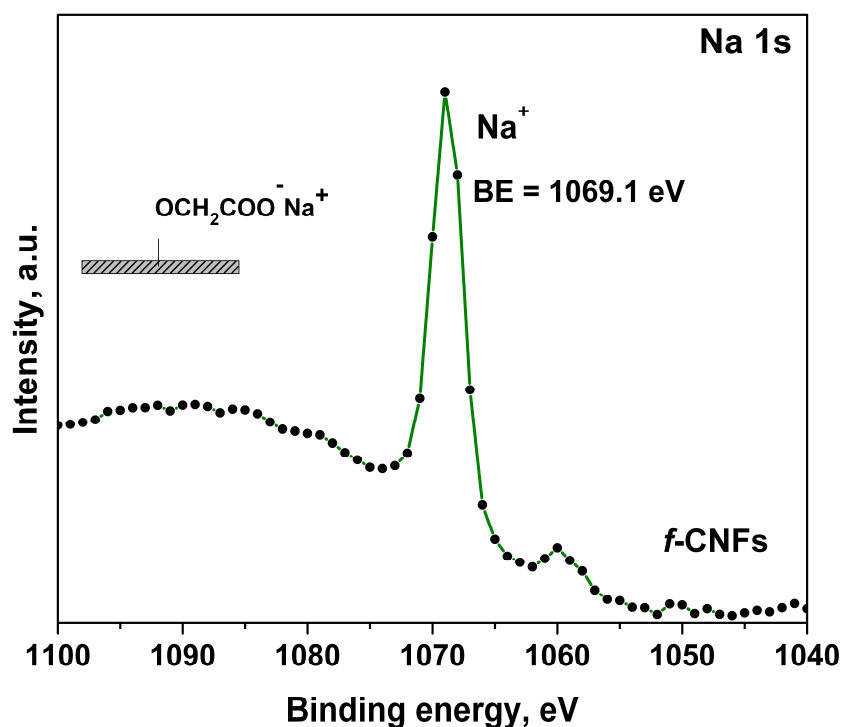
Figure 4.5 – XPS spectrum of *f*-CNFs, Na 1s peak.

4.3.2 Characterization of nanocomposites (RuNPs/CNFs and AgNPs/CNFs)

TEM images were taken for RuNPs/CNFs and AgNPs/CNFs nanocomposites (Figure 4.6) to investigate their surface morphology in terms of size, distribution and adhesion of MNPs. Figure 4.6(a-c) showed a very fine and uniformly dispersed RuNPs externally attached on the surface of CNFs. Similarly, Figure 4.6(d-f) showed good adhesion of AgNPs on the CNFs with a very narrow particle size distribution. The mean diameter of these RuNPs and AgNPs was 8±2.0 nm and 4±2.0 nm respectively; as calculated from TEM images. Furthermore, there was no free MNPs in the background of

the TEM images. The better morphology (mainly, excellent adhesion and uniform dispersion of the MNPs on the CNFs surface) of the RuNPs/CNFs and AgNPs/CNFs is due to the anionic functional groups present in the CNFs. In order to confirm the role of the anionic functional groups, non-functionalized CNFs were also employed to decorate the MNPs. However, the decoration of MNPs on non-functionalized CNFs was not uniform and the size of metal NPs was larger with broader size. Figure 4.7 shows the SEM-EDS and corresponding elemental mapping images of RuNPs/CNFs and AgNPs/CNFs nanocomposites. The weight percentage of Ru in RuNPs/CNFs and Ag in AgNPs/CNFs was found to be 13.29 and 22.60 respectively. The insets in Figures 4.7(b) and 4.7(d) show that the distribution of Ru in RuNPs/CNFs and Ag in AgNPs/CNFs is homogeneous.
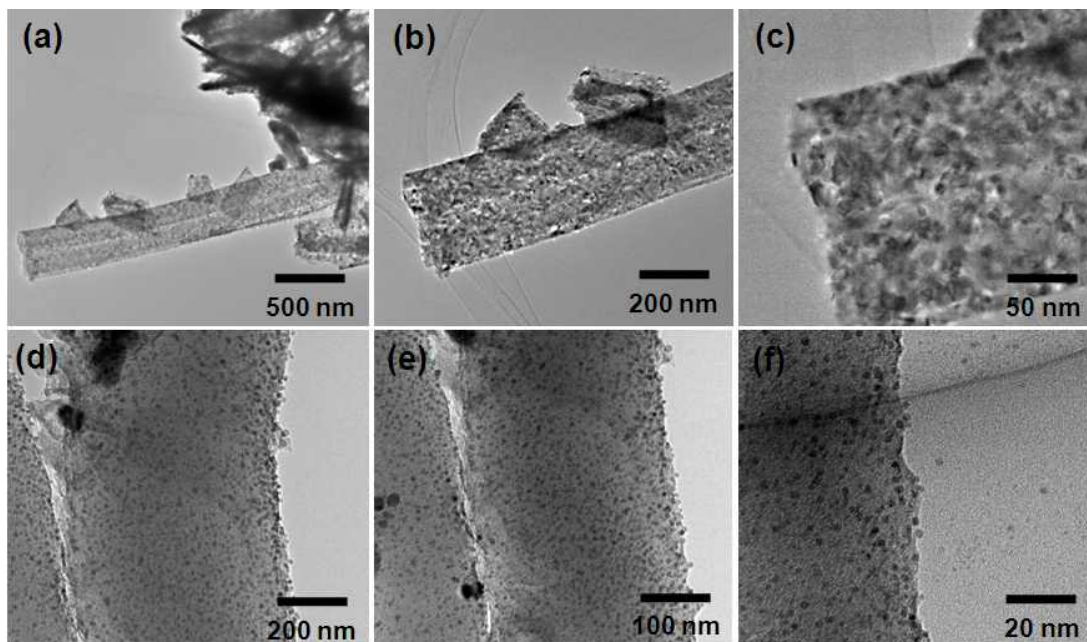

Figure 4.6 – TEM images of (a, b and c) RuNPs/CNFs and (d, e and f) AgNPs/CNFs.
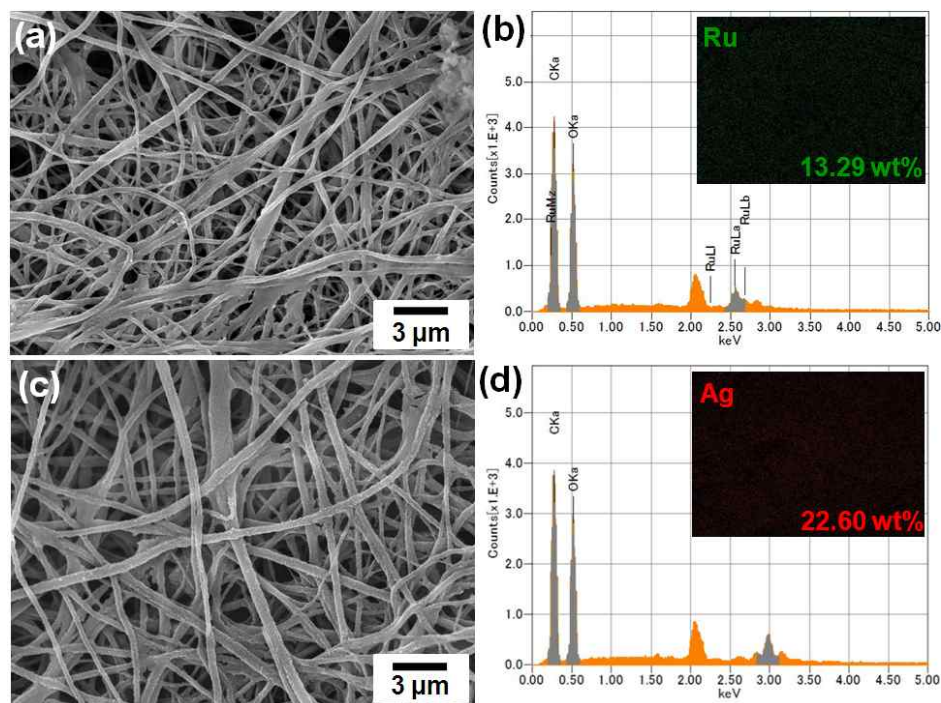
Figure 4.7 – SEM images of (a) RuNPs/CNFs and (c) AgNPs/CNFs. EDS spectra of (b) RuNPs/CNFs and (d) AgNPs/CNFs, and the insets show the corresponding EDS mapping of (inset in b) Ru and (inset in d) Ag.
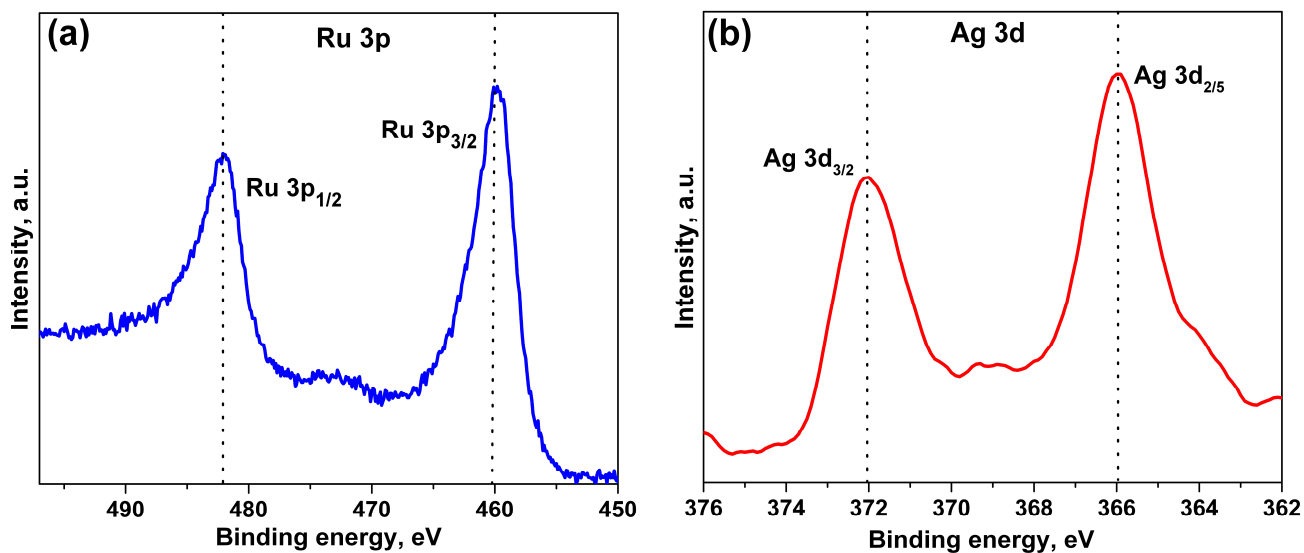

Figure 4.8 – (a) Ru 3d XPS spectrum of RuNPs/CNFs, and (b) Ag 3d XPS spectrum of AgNPs/CNFs.

XPS spectra were recorded for RuNPs/CNFs and AgNPs/CNFs nanocomposites; the results are shown in Figure 4.8. As expected, both RuNPs/CNFs and AgNPs/CNFs exhibited C 1s and O 1s peaks at 283.1 and 530.5 eV respectively. The XPS spectrum of RuNPs/CNFs in Ru 3p region [Figure 4.8(a)] showed BE of Ru $3p_{3/2}$ at 460.1 eV and Ru $3p_{1/2}$ at 482.5 eV. In Figure 4.8(b), AgNPs/CNFs showed Ag $3d_{2/5}$ peak at 366.2 eV and Ag $3d_{3/2}$ at 372.3 eV. Although the Ru and Ag are in a metallic state, the XPS spectra showed major shifts in the Ru 3d and Ag 3d peaks toward lower binding energies. It was calculated to be ~1.1 eV for Ru 3d and ~2.1 eV for Ag 3d[33,37]. According to Li *et al*.,[38] such kind of phenomenon is mainly due to the size effect of the NPs and the interaction between NPs and the support matrix. Moreover, the weight percentage of the Ru (12.68 wt%) in RuNPs/CNFs and Ag (20.59 wt%) in AgNPs/CNFs was measured by XPS analysis. The results are in well agreement with the TEM and SEM-EDS results.

Since the MNPs (Ru and Ag) were strongly attached on the surface of CNFs, the crystalline nature of the CNFs before (CANFs and CNFs) and after chemical modification (*f*-CNFs, RuNPs/CNFs and AgNPs/CNFs) was investigated by XRD analysis. Figure 4.9 shows XRD patterns of CANFs, CNFs, *f*- CNFs, RuNPs/CNFs and AgNPs/CNFs. Very weak diffraction peak was observed at 12.7° and the peak at 20.4° was virtually absent in the XRD pattern of all the five samples, which ascribed to the amorphous nature of the nanofibers[39]. A new peak at 33.4° was observed for *f*-CNFs which may be due to the presence of Na (CH_2-COO^-Na^+ group)[40]. There is no significant change in the diffraction patterns of RuNPs/CNFs and AgNPs/CNFs when compared to *f*-CNFs. However, disappearance of a peak at 33.4° might have caused by the replacement of Na^+ by the metal. The results showed that the attachment of MNPs

(Ru and Ag) is obviously on the surface of the CNFs but not into the CNFs matrix. In addition, the XRD pattern of RuNPs/CNFs (Figure 4.9) shows no diffraction peaks for Ru, indicating the nano-crystalline nature of RuNPs. The XRD pattern of AgNPs/CNFs shows sharp diffraction patterns at $2\theta = 38.1°$ and $44.3°$, which correspond to the (111) and (200) reflections of metallic Ag[41].
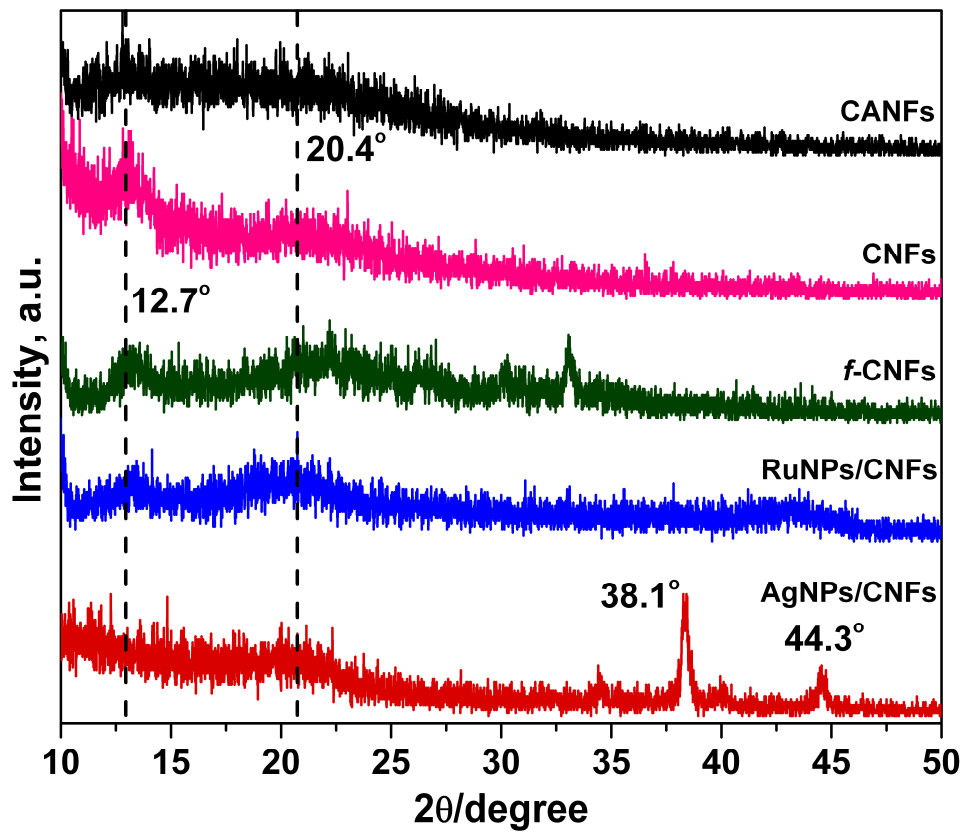
Figure 4.8 – XRD patterns of CANFs, CNFs, *f*-CNFs, RuNPs/CNFs and AgNPs/CNFs.

4.3.3 Catalytic applications

After the complete characterization, the RuNPs/CNFs and AgNPs/CNFs nanocomposites were used as catalysts for oxidation of benzyl alcohol and *aza*-Michael reaction of 1-phenylpiperazine with acrylonitrile respectively. Certainly, these reactions are important in synthetic organic chemistry and the products found applications in various fields such as pharmaceuticals and fine chemicals[42,43]. Benzaldehyde is an important intermediate for the perfumery, pharmaceutical, dyestuff and agrochemicals[44]. Similarly, the piperazine motifs often play a key role in the preparation of biologically active molecules and drugs[45]. Although there are several RuNPs-based heterogeneous catalysts available to date, we are reporting NFs immobilized RuNPs for oxidation of benzyl alcohol for the first time (Figure 4.10 and Scheme 4.1). Similarly, to the best of our knowledge, this is the first AgNPs-catalyzed *aza*-Michael reaction (Figure 4.11 and Scheme 4.2).
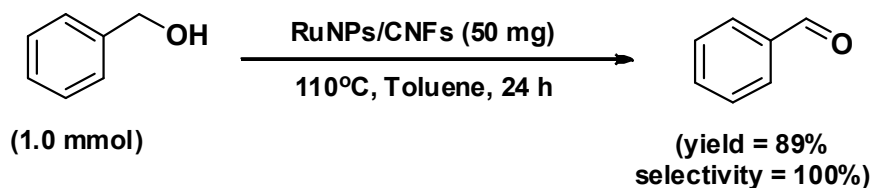
Scheme 4.1 – RuNPs/CNFs-catalyzed oxidation of benzyl alcohol to benzaldehyde.
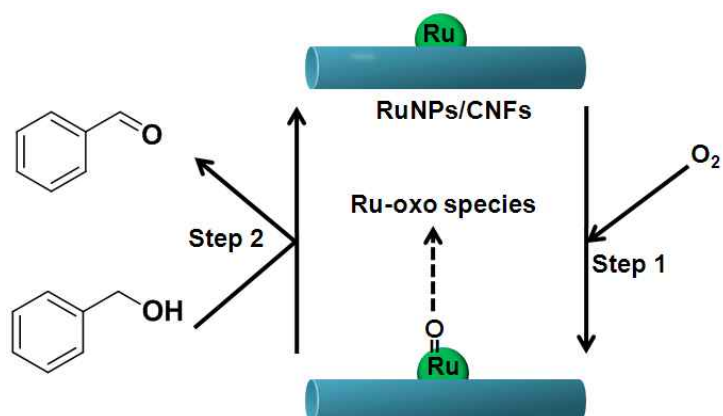
Figure 4.10 – Proposed mechanism for the oxidation of benzyl alcohol catalyzed by RuNPs/CNFs.
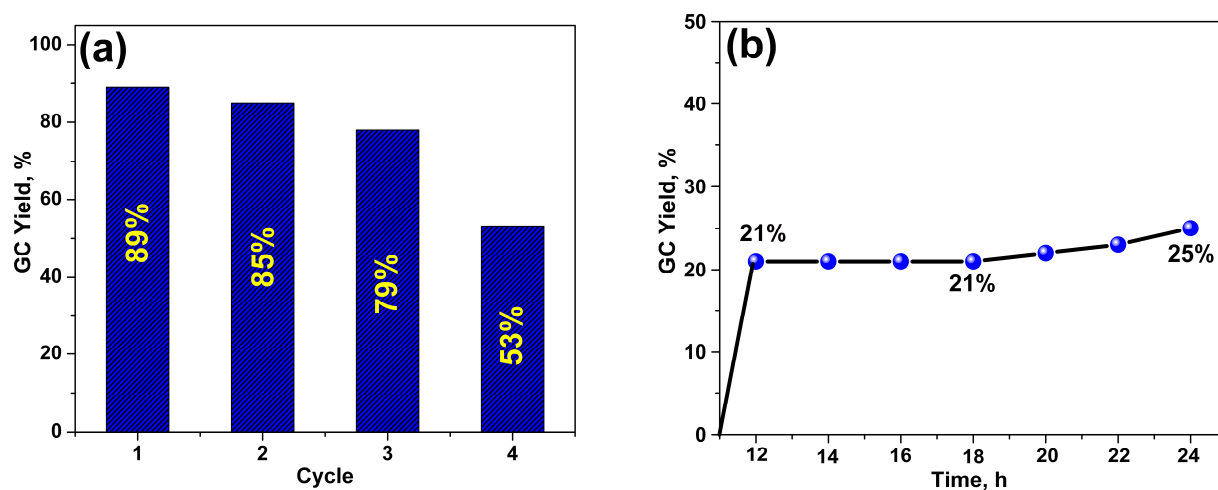
Figure 4.11 – Reusability and heterogeneity tests of RuNPs/CNFs.
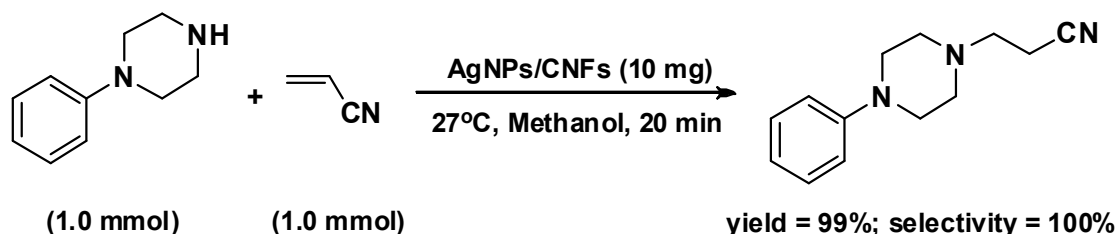
Scheme 4.2 – Ag/CNFs-catalyzed *aza*-Michael reaction of 1-phenylpiperazine with acrylonitrile.

4.3.4 Oxidation of benzyl alcohol by RuNPs/CNFs

Initially, the reaction conditions were optimized. As we expected, very low conversion of 9% was obtained in the absence of RuNPs/CNFs. Likewise, when the amount of catalyst was low (25 mg), the system showed poor yield of 56% but with excellent selectivity (100%). A 50 mg of RuNPs/CNFs (6.5 mol%) was found to be the optimum amount of catalyst which produced 89% yield and 100% selectivity. However, further increase in the amount of RuNPs/CNFs (75 mg) showed no significant change in the yield. The catalyst with low metal loadings also did not work well for the oxidation reaction (data not shown). Subsequently, reaction time was optimized and found to be 24h. An excellent yield of 89% was obtained at the temperature of 110°C. Unfortunately at the lower reaction temperatures (27, 50 and 70°C) the reactions were very slow and gave poor yields. In order to know the influence of CNFs support on the oxidation reaction, pure CNFs (50 mg) were used as catalyst under optimized reaction conditions. It

was concluded that the CNFs have no significant influence on the reaction since a very low conversion (5%) was observed. The present result is better than those previously reported. For instance, Ru/TiO_2 catalytic system gave 85% of the desired product under O_2/Ar (5%/95%) atmosphere after 2 h[46]. By using Ru-substituted silicotungstate as a catalyst[47], only 36% of benzaldehyde was obtained from the oxidation of benzyl alcohol under O_2 atmosphere after 120 h. The present catalytic system show 89% of the desired product, however the activity is slightly lower than the commercial catalysts such as Ru/Al_2O_3[48].

Mechanism has been proposed for the RuNPs/CNFs-catalyzed oxidation of benzyl alcohol (Figure 4.10). In the first step, RuNPs form $Ru^{II}=O$ species with the help of atmospheric oxygen. In step 2, the formed Ru-oxo species assist the formation of benzaldehyde from benzyl alcohol. Finally, RuNPs/CNFs was regenerated for the further oxidation process. FT-IR spectra were recorded for the RuNPs/CNFs before and after the reaction (50 mg of RuNPs/CNFs were stirred in 5 mL of toluene under air atmosphere at 110°C for 12 h). The RuNPs/CNFs after reaction showed a new peak at 775 cm^{-1}, indicating the formation of Ru-oxo species. In addition, the oxidation reaction was performed under N_2 atmosphere using the optimized reaction conditions and a very low conversion of 9% was observed. The result confirmed that the catalyst oxidize the benzyl alcohol using the atmospheric O_2.

The reusability and heterogeneity of RuNPs/CNFs were tested; the results are presented in Figure 4.11. The catalyst can be reused for three times (79% at 3rd cycle) without significant loss of the activity in terms of yield. However, the yield of benzaldehyde decreased significantly to 53% at 4th cycle (Figure 4.11a). A hot filtration

test was carried out with benzyl alcohol under optimized reaction conditions to demonstrate the heterogeneity of RuNPs/CNFs. In a typical test, the RuNPs/CNFs were removed by simple filtration and the filtrate was stirred for another 12 h. The progress of the reaction was monitored by GC and the results are shown in Figure 4.11b. It can be seen that no significant increase in the yield even after 24 h (25%) is observed, indicating no leaching of RuNPs from the catalyst.

4.3.4 AgNPs/CNFs-catalyzed *aza*-Michael reaction

To select suitable reaction medium, different solvents such as THF, acetonitrile, methanol and water were tested. It was found that methanol is the best solvent which gave an excellent yield of 99% with 100% selectivity. In the time optimization, the system showed an excellent yield of 99% after 20 min. Then, catalyst amount was optimized and found that the 10 mg of the AgNPs/CNFs is enough for the reaction. A poor yield was obtained when the reaction was preformed with 10 mg of pure CNFs as catalyst under optimized reaction conditions. After the catalytic reactions, the nanocomposites could be easily separated by simple filtration. The CuNPs catalytic system showed 82% of the desired product after the reaction time of 8 h[49]. The PEG catalytic system gave an excellent yield of 99% after 30 min[50]. Interestingly, the present AgNPs/CNFs system is better when compared to the above results. The excellent catalytic activity of these nanocomposites is obviously due to the good physicochemical properties such as smaller size, homogenous dispersion of the MNPs, and strong interaction between the MNPs and CNFs matrix.
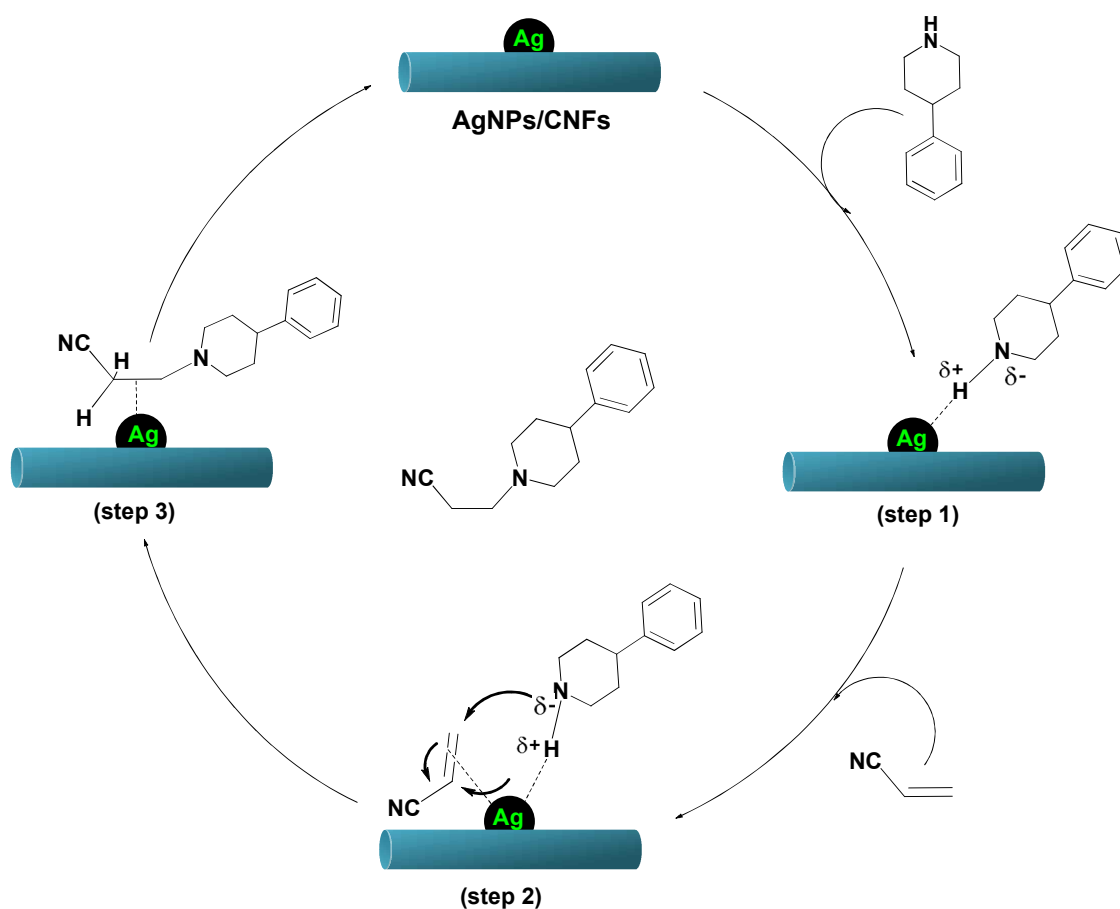
Figure 4.12 – Proposed mechanism for *aza*-Michael reaction of 1-phenylpiperazine with acrylonitrile catalyzed by AgNPs/CNFs.

The proposed mechanism for AgNPs/CNFs-catalyzed *aza*-Michael reaction has been provided in Figure 4.12. The 1-phenylpiperazine and acrylonitrile act as a Michael donor and acceptor respectively. Firstly, stirring the mixture of AgNPs/CNFs and 1-phenylpiperazine may lead to the attraction between AgNPs and hydrogen attached to the amine (step 1), which makes the N-H bond weaker (step 1) and simultaneously enhancing the nucleophilicity of the nitrogen for the addition to electron-deficient alkenes. Secondly, the attracted 1-phenylpiperazine undergoes reaction with acrylonitrile to form *aza*-

Michael adduct (step 2). Finally, the catalytic cycle is completed by desorption of the product (step 3). FT-IR spectra were taken for AgNPs/CNFs before (pure catalyst) and after the reaction [the catalyst (10 mg) after stirring with 1-phenylpiperazine (1.0 mmol) in methanol at 25°C for 20 min]. Several new peaks (600-1650 cm^{-1}) correspond to 1-phenylpiperazine were observed in the spectrum of AgNPs/CNFs after the reaction. In addition, a broad peak at 2770 cm^{-1} attributed to the N-H group. The result supports the proposed mechanism.

Figure 4.13 – (a) Reusability test of AgNPs/CNFs. (b) EDS spectrum, (c) SEM image of used AgNPs/CNFs and (d) elemental mapping observation of Ag.

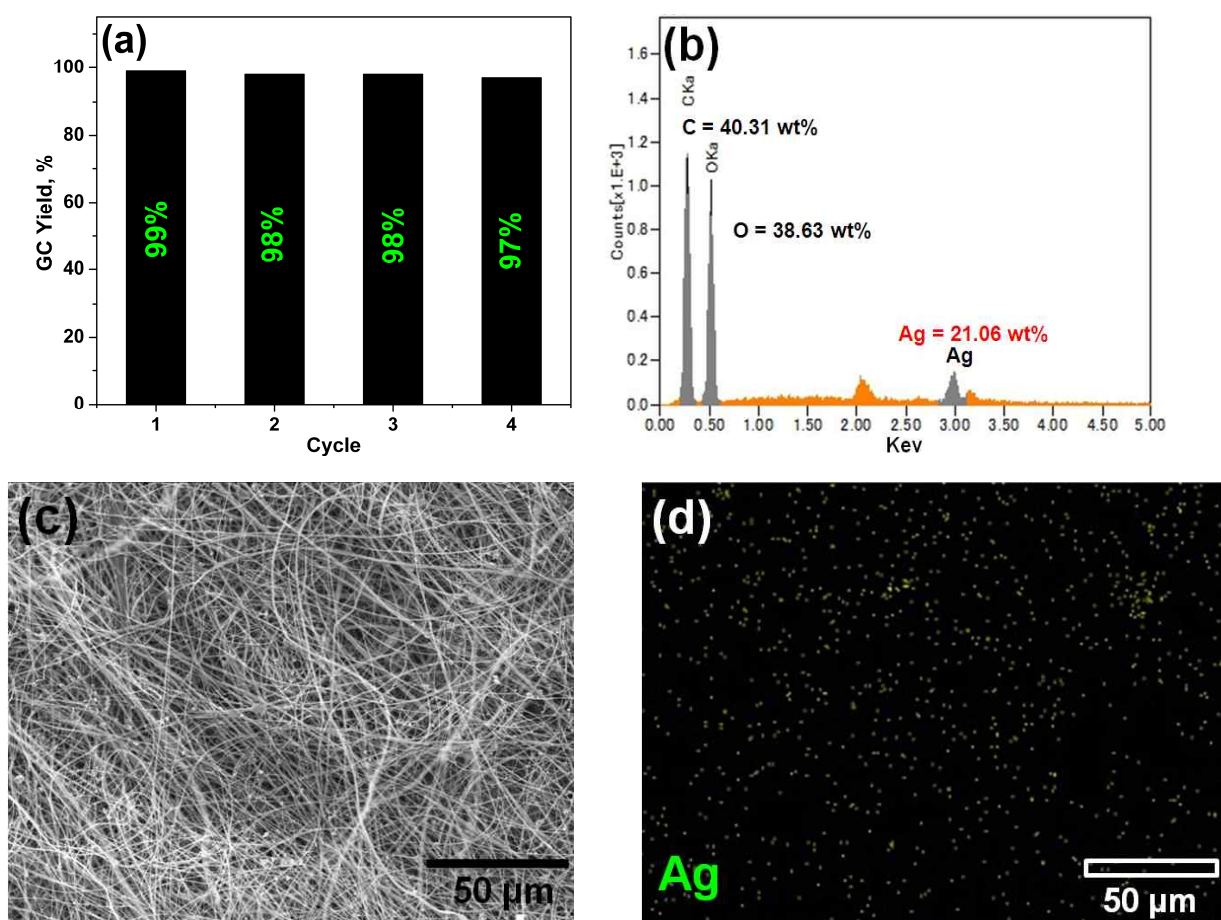Alike the RuNPs/CNFs system, the reusability and stability of the AgNPs/CNFs were investigated in detail; the results are shown in Figure 4.13. Interestingly, the catalyst showed an excellent yield even after 4th cycle (97%). Since the reusability of AgNPs/CNFs was good, the stability was tested for the AgNPs/CNFs after being used for four times. The EDS spectrum showed that the weight percentage of Ag in AgNPs/CNFs after use was 21.06 wt%, which reveals there is no significant loss of Ag. It can be seen from Figure 4.13, the fiber morphology of the AgNPs/CNFs (Figure 4.13c) was maintained without any aggregation of AgNPs (Figure 4.13d). The results confirmed that the AgNPs/CNFs is heterogeneous catalyst and stable.

4. 4 Conclusion

We demonstrated an efficient method for the fabrication of RuNPs/CNFs and AgNPs/CNFs nanocomposites. TEM and SEM images confirmed a very fine and homogeneous decoration of the MNPs (RuNPs and AgNPs) on the surface of CNFs. The weight percentage of the Ru and Ag in the nanocomposites was found to be 13.29 and 22.60 respectively. The metallic state and strong attachment of the Ru and Ag in the nanocomposites were confirmed by XPS and XRD analyses. The advantage of these nanocomposites was proven by their superior catalytic activity towards the organic transformation reactions. The RuNPs/CNFs catalyst showed a good yield of 89% (100% selectivity) in the oxidation of benzyl alcohol. Alike, the AgNPs/CNFs system gave an excellent yield (99%) with 100% selectivity towards the *aza*-Michael reaction. Overall, the RuNPs/CNFs and AgNPs/CNFs are efficient nanocatalysts for organic transformations.

Reference

[1] Arakawa, H. Catalysis Research of Relevance to Carbon Management: Progress, Challenges, and Opportunities. *Chem. Rev.* **2011**, 101, 953−996.

[2] Ganesh Babu, S.; Karvembu, R. Copper Based Nanoparticles-Catalyzed Organic Transformations. *Catal. Surv. Asia*. **2013**, 17, 156–176.

[3] Mizuno, N.; Misono, M. Heterogeneous Catalysis. *Chem. Rev*. **1998**, 98, 199–217.

[4] Hudson, R. ; Feng, Y.; Varma, R. S.; Moores, A. Bare Magnetic Nanoparticles: Sustainable Synthesis and Applications in Catalytic Organic Transformations. *Green Chem*. **2014**, 16, 4493–4505.

[5] Ho, C. M. ; Yu, W. Y.; Che, C. M. Ruthenium Nanoparticles Supported on Hydroxyapatite as an Efficient and Recyclable Catalyst for *cis*-Dihydroxylation and Oxidative Cleavage of Alkenes. *Angew. Chem.* **2004**, 116, 3365–3369.

[6] Carrillo, A. I.; Schmidt, L. C.; Marína, M. L.; Scaiano, J. C. Mild synthesis of mesoporous silica supported ruthenium nanoparticles as heterogeneous catalysts in oxidative Wittig coupling reactions. *Catal. Sci. Technol*. **2014**, 4, 435–440.

[7] Gopiraman, M.; Karvembu, R.; Kim, I. S. Highly Active, Selective, and Reusable RuO2/SWCNT Catalyst for Heck Olefination of Aryl Halides. *ACS Catal*. **2014**, 4, 2118−2129.

[8] Gopiraman, M.; Bang, H.; Ganesh Babu, S.; Wei, K.; Karvembu, R.; Kim, I. S. Catalytic N-oxidation of tertiary amines on RuO2NPs anchored graphene nanoplatelets. *Catal. Sci. Technol*. **2014**, 4, 2099−2106.

[9]   Joo, S. H.; Park, J. Y.; Renzas, J. R.; Butcher, D. R.; Huang, W. Y.; Somorjai, G. A. Size Effect of Ruthenium Nanoparticles in Catalytic Carbon Monoxide Oxidation. *Nano Lett*. **2010**, 10, 2709–2713.

[10] Gopiraman, M.; Ganesh Babu, S.; Khatri, Z.; Kai, W.; Kim, Y. A.; Endo, M.; Karvembu, R.; Kim, I. S. An efficient, reusable copper-oxide/carbon-nanotube catalyst for N-arylation of imidazole. *Carbon*, **2013**, 62, 135–148.

[11] Wendel, W.; Sandra, B.; Matthias, W. M.; Michael, M.; Gerhard, C.; Sabine, H.; Bernhard, V.; Volker, S.; Silke, T.; Karin, W.; Lan, M. H.; Robert, L. On the Lifecycle of Nanocomposites: Comparing Released Fragments and their In-Vivo Hazards from Three Release Mechanisms and Four Nanocomposites. *Small.* **2011**, 7, 2384-2395.

[12] Yoon, K.; Hsiao, B. S.; Chu, B. Functional nanofibers for environmental applications. *J. Mater. Chem*. **2008**, 18, 5326–5334.

[13] Bang, H.; Watanabe, K,; Nakashima, R.; Kai, W.; Song, K. H.; Lee, J. S.; Gopiraman, M.; Kim, I. S. A highly hydrophilic water-insoluble nanofiber composite as an efficient and easily-handleable adsorbent for the rapid adsorption of cesium from radioactive wastewater. *RSC Adv*. **2014**, 4, 59571-59578.

[14] Siro, I.; Plackett, D. Microfibrillated cellulose and new nanocomposite materials: a review. *Cellulose*. **2010**, 17, 459–494.

[15] Takagi, H.; Asano, A. Effects of processing conditions on flexural properties of cellulose nanofiber reinforced "green" composites. *Composites: Part A*. **2008**, 39, 685–689.

[16]   Isogai, A.; Saito, T.; Fukuzumi, H. TEMPO-oxidized cellulose nanofibers. *Nanoscale*. **2011**, 3, 71–85.

[17]   Iwamoto, S.; Isogai, A.; Iwata, T. Structure and Mechanical Properties of Wet-Spun Fibers Made from Natural Cellulose Nanofibers. *Biomacromolecules*. **2011**, 12, 831–836.

[18]   Ma, Z.; Kotaki, M.; Ramakrishna, S. Electrospun cellulose nanofiber as affinity membrane. *J. Membrane Sci*. **2005**, 265, 115–123.

[19]   Chen, W.; Yu, H.; Liu, Y.; Hai, Y.; Zhang, M.; Chen, P. Isolation and characterization of cellulose nanofibers from four plant cellulose fibers using a chemical-ultrasonic process. *Cellulose*. **2011**, 18, 433–442.

[20]   Ifuku, S.; Nogi, M.; Abe, K.; Handa, K.; Nakatsubo, F.; Yano, H. Surface Modification of Bacterial Cellulose Nanofibers for Property Enhancement of Optically Transparent Composites: Dependence on Acetyl-Group DS. *Biomacromolecules*. **2007**, 8, 1973–1978.

[21]   Khatri, Z.; Gopiraman, M.; Hirata, Y.; Wei, K.; Kim, I. S. Cationic-cellulose nanofibers: Preparation and dyeability with anionic reactive dyes for apparel application. *Carbohydr. Polym*. **2013**, 91, 434–443.

[22]   Jarvis, M. Chemistry: Cellulose stacks up. *Nature*. **2003**, 426, 611–612.

[23]   Koga, H.; Tokunaga, E.; Hidaka, M.; Umemura, Y.; Saito, T.; Isogai, A.; Kitaoka, T. Topochemical synthesis and catalysis of metal nanoparticles exposed on crystalline cellulose nanofibers. *Chem. Commun*. **2010**, 46, 8567–8569.

[24] Azetsu, A.; Koga, H.; Isogai, A.; Kitaoka, T. Synthesis and Catalytic Features of Hybrid Metal Nanoparticles Supported on Cellulose Nanofibers. *Catalysts*. **2011**, 1, 83–96.

[25] Edmond, L.; Sabahudin, H.; Ehsan, M.; Jonathan, H. C.; John, H. T. L. Catalysis using gold nanoparticles decorated on nanocrystalline cellulose. *Nanoscale*. **2012**, 4, 997–1002.

[26] Son, W. K.; Youk, J. H.; Park, W. H. Antimicrobial cellulose acetate nanofibers containing silver nanoparticles. *Carbohydr. Polym*. **2006**, 65, 430–434.

[27] Zhang, T.; Wang, W.; Zhang, D.; Zhang, X.; Ma, Y.; Zhou, Y.; Qi, L. Biotemplated Synthesis of Gold Nanoparticle–Bacteria Cellulose Nanofiber Nanocomposites and Their Application in Biosensing. *Adv. Funct. Mater*. **2010**, 20, 1152–1160.

[28] Zhou, P.; Wang, H.; Yang, J.; Tang, J.; Sun, D.; Tang, W. Bacteria Cellulose Nanofibers Supported Palladium(0) Nanocomposite and Its Catalysis Evaluation in Heck Reaction. *Ind. Eng. Chem. Res*. **2012**, 51, 5743−5748.

[29] Gopiraman, M.; Fujimori, K.; Zeeshan, K.; Kim, B. S.; Kim, I. S. Structural and mechanical properties of cellulose acetate/graphene hybrid nanofibers: Spectroscopic investigations. *Express Polym. Lett*. **2013**, 7, 554−563.

[30] Deng, L.; Young, R. J.; Kinloch, I. A.; Zhu, Y.; Eichhorn, S. J. Carbon nanofibres produced from electrospun cellulose nanofibres. *Carbon*. **2013**, 58, 66–75.

[31] Formo, E.; Yavuz, M.; Lee, E. P.; Lane, L.; Xia, Y. Functionalization of electrospun ceramic nanofibre membranes with noble-metal nanostructures for catalytic applications. *J. Mater. Chem*. **2009**, 19, 3878–3882.

[32] Zhang, L.; Menkhaus, T. J.; Fong, H. Fabrication and bioseparation studies of adsorptive membranes/felts made from electrospun cellulose acetate nanofibers. *J. Membr. Sci.* **2008**, 319, 176–184.

[33] Lawal, O. S.; Yoshimura, M.; Fukae, R.; Nishinari, K. Microporous hydrogels of cellulose ether cross-linked with di- or polyfunctional glycidyl ether made for the delivery of bioactive substances. *Colloid Polym. Sci.* **2011**, 289, 1261–1272.

[34] Qaiser, A. A.; Hyland, M. M.; Patterson, D. A. Surface and Charge Transport Characterization of Polyaniline−Cellulose Acetate Composite Membranes. *J. Phys. Chem. B.* **2011**, 115, 1652–1661.

[35] Liu, H.; Wang, Y.; Li, L.; Wang, K.; Hosono, E.; Zhou, H. Facile synthesis of NaV_6O_{15} nanorods and its electrochemical behavior as cathode material in rechargeable lithium batteries. *J. Mater. Chem.* **2009**, 19, 7885–7891.

[36] Gopiraman, M.; Ganesh Babu, S.; Khatri, Z.; Wei, K.; Kim, Y. A.; Endo, M.; Karvembu, R.; Kim, I. S. Dry Synthesis of Easily Tunable Nano Ruthenium Supported on Graphene: Novel Nanocatalysts for Aerial Oxidation of Alcohols and Transfer Hydrogenation of Ketones. *J. Phys. Chem. C.* **2013**, 117, 23582–23596.

[37] Song, J.; Kang, H.; Lee, C.; Hwang, S. H.; Jang, J. Aqueous Synthesis of Silver Nanoparticle Embedded Cationic Polymer Nanofibers and Their Antibacterial Activity. *ACS Appl. Mater. Interfaces.* **2012**, 4, 460−465.

[38] Li, J.; Guo, L.; Zhang, L.; Yu, C.; Yu, L.; Jiang, P.; Wei, C.; Qin, F.; Shi, J. Donor−π−acceptor structure between Ag nanoparticles and azobenzenechromophore and its enhanced third-order optical non-linearity. *Dalton Trans.* **2009**, 823–831.

[39] Khatri, Z.; Arain, R. M.; Jatoi, A. W.; Mayakrishnan, G.; Wei, K.; Kim, I. S. Dyeing and characterization of cellulose nanofibers to improve color yields by dual padding method. *Cellulose.* **2013**, 20, 1469–1476.

[40] Parmeggiani, C.; Cardona, C. Transition metal based catalysts in the aerobic oxidation of alcohols. *Green Chem.* **2012**, 14, 547−564.

[41] Liu, C.; Kim, W. S.; Baek, J.; Cho, Y.; Han, S.; Kim, S. W.; Min, N. K.; Choie, Y.; Kim, J. U.; Lee, C. J. Improved field emission properties of double-walled carbon nanotubes decorated with Ru nanoparticles. *Carbon.* **2009**, 47, 1158−1164.

[42] Jude, A. O.; Paul, T. W. Hydrothermal reactions of sodium formate and sodium acetate as model intermediate products of the sodium hydroxide-promoted hydrothermal gasification of biomass. *Green Chem.* **2010**, 12, 2214−2224.

[43] Xiao, S.; Xu, W.; Ma, H.; Fang, X. Size-tunable Ag nanoparticles immobilized in electrospun nanofibers: synthesis, characterization, and application for catalytic reduction of 4-nitrophenol. *RSC Adv.* **2012**, 2, 319–327.

[44] Amakawa, K.; Kolenko, Y. V.; Villa, A.; Schuster, M. V.; Csepei, L.; Weinberg, G.; Wrabetz, S.; Alnoncourt, R. N.; Girgsdies, E.; Prati, L.; Schlogl, R.; Trunschke, A. Multifunctionality of Crystalline MoV(TeNb) M1 Oxide Catalysts in Selective Oxidation of Propane and Benzyl Alcohol. *ACS Catal.* **2013**, 3, 1103−1113.

[45] Bartoli, G.; Bartolacci, M.; Giuliani, A.; Marcantoni, E.; Massaccesi, M.; Torregiani, E. Improved Heteroatom Nucleophilic Addition to Electron-Poor Alkenes Promoted by CeCl$_3$·7H$_2$O/NaI System Supported on Alumina in Solvent-Free Conditions. *J. Org. Chem.* **2005**, 70, 169−174.

[46] Kockritz, A.; Sebek, M.; Dittmar, A.; Radnik, J.; Bruckner, A.; Bentrup, U.; Magerlein, W. Ru-catalyzed oxidation of primary alcohols. *J. Mol. Catal. A: Chem*. **2006**, 246, 85−99.

[47] Yamaguchi, K.; Mizuno, N. Heterogeneously catalyzed liquid-phase oxidation of alkanes and alcohols with molecular oxygen. *New J. Chem*. **2002**, 26, 972−974.

[48] Zsigmond, A.; Notheisz, F.; Csjernyik, G.; Backvall, J. E. Ruthenium-Catalyzed Aerobic Oxidation of Alcohols on Zeolite-Encapsulated Cobalt Salophen Catalyst. *Top. Catal*. **2002**, 19, 119−124.

[49] Yamaguchi K.; Mizuno, N. Supported Ruthenium Catalyst for the Heterogeneous Oxidation of Alcohols with Molecular Oxygen. *Angew. Chem. Int. Ed*. **2002**, 41, 4538−4542.

[50] Kumar, R.; Chaudhary, P.; Nimesh, S.; Chandra, R. Polyethylene glycol as a non-ionic liquid solvent for Michael addition reaction ofamines to conjugated alkenes. *Green Chem*. **2006**, 8, 356–358.

[51] Verma, A. K.; Kumar, R.; Chaudhary, P.; Saxena, A.; Shankar, A.; Mozumdar, S.; Chandra, R. Cu-nanoparticles: a chemoselective catalyst for the aza-Michael reactions of *N*-alkyl- and *N*-arylpiperazines with acrylonitrile. *Tetrahedron Lett*. **2005**, 46, 5229–5232.

CHAPTER 5

Conclusions

CHAPTER 5

Conclusions

We have successfully prepared the PVA/MWNT composite nanofibers by electrospinning method, and studied the effects of MWNT concentration and pH on the morphologies, microstructures and mechanical properties of the resultant PVA/MWNT composite nanofibers. SEM analysis demonstrated that the PVA/MWNT nanofibers with acid-treated MWNTs of 1.0 wt% gave rather smaller diameter and narrower distribution, suggesting well-distribution of the MWNTs onto the PVA nanofiber matrix, which was also confirmed by TEM analysis. In addition, it was found that the PVA/acid-treated MWNT (MWNTs concentration ~ 1.0 wt%) nanofibers at higher pH gave lower diameter than those at lower pH, due to a decreased molecular interaction between PVA and acid-treated CNTs, and thereby results in a decreased viscosity and their diameters. Moreover, the resultant nanofibers at lower pH have better mechanical properties than those at higher pH. Also, the crystalline structures of the PVA/MWNT nanofibers were altered when the pH of the PVA/MWNT dispersion solutions was changed.

We have successfully prepared a new PBNPs-based PVA composite nanofibers (*c*-PBNPs/PVA) via electrospinning. SEM images revealed smooth and continuous nanofiber morphology of the *c*-PBNPs/PVA composite with diameters of 200-300 nm and lengths up to several millimeters. TEM images confirmed homogeneous dispersion and well incorporation of PBNPs into the PVA matrix. The amorphous nature of the *c*-PBNPs/PVA composite nanofibers was confirmed by the XRD analysis. FT-IR spectra showed successful cross-linking of PVA with GA. It was found that the prepared

nanocomposite fiber is highly hydrophilic and water-insoluble. The excellent activity of the *c*-PBNPs/PVA composite nanofibers can be realized from the higher Cs adsorption rate of 96 % after only 100 min. Moreover, the mass production of the *c*-PBNPs/PVA is simple and cost-effective. After Cs adsorption test, the *c*-PBNPs/PVA can be easily separated from the wastewater. Overall, the simple preparation, easy separation and faster Cs adsorption activity make *c*-PBNPs/PVA as an alternate choice to the existing PBNPs-composite materials.

We demonstrated an efficient method for the fabrication of RuNPs/CNFs and AgNPs/CNFs nanocomposites. TEM and SEM images confirmed a very fine and homogeneous decoration of the MNPs (RuNPs and AgNPs) on the surface of CNFs. The weight percentage of the Ru and Ag in the nanocomposites was found to be 13.29 and 22.60 respectively. The metallic state and strong attachment of the Ru and Ag in the nanocomposites were confirmed by XPS and XRD analyses. The advantage of these nanocomposites was proven by their superior catalytic activity towards the organic transformation reactions. The RuNPs/CNFs catalyst showed a good yield of 89% (100% selectivity) in the oxidation of benzyl alcohol. Alike, the AgNPs/CNFs system gave an excellent yield (99%) with 100% selectivity towards the *aza*-Michael reaction. Overall, the RuNPs/CNFs and AgNPs/CNFs are efficient nanocatalysts for organic transformations.